Title
Enhanced Loss of Magnetic Mirror Trapped Fast Electrons by a Shear Alfven Wave

Author
Wang, Yuhou

Publication Date
2013

Peer reviewed|Thesis/dissertation

UNIVERSITY OF CALIFORNIA

Los Angeles

Enhanced Loss of Magnetic Mirror Trapped Fast Electrons by a Shear Alfvén Wave

A dissertation submitted in partial satisfaction
of the requirements for the degree
Doctor of Philosophy in Physics

by

Yuhou Wang

2013

ABSTRACT OF THE DISSERTATION

Enhanced Loss of Magnetic Mirror Trapped Fast Electrons by a Shear Alfvén Wave

by

Yuhou Wang

Doctor of Philosophy in Physics

University of California, Los Angeles, 2013

Professor Walter Gekelman, Chair

Highly energetic electrons produced naturally or artificially can be trapped in the Earth's radiation belts for months, posing a severe danger to valuable space satellites. Concepts that can lead to radiation belts mitigation have drawn a great deal of interest. This dissertation investigates the loss of fast electrons from a magnetic mirror trap when irradiated by a shear Alfvén wave. The experiment is performed in the quiescent after-glow plasma in the Large Plasma Device (LaPD). The background magnetic field is programmed to include a magnetic mirror section (mirror ratio ≈ 2, length = 3.5 m). A trapped fast electron population is generated in the mirror section by X-mode high power microwave pulses. Different power levels, pulse durations and heating schemes lead to different electron energies. Two distinct electron energy ranges are studied separately in this work, which are around 100 eV and 100 keV respectively. Shear Alfvén waves of arbitrary polarization are launched externally by a Rotating Magnetic Field (RMF) source ($\delta B/B_0 \approx 0.1\%$, $\lambda_{\parallel} \approx 9m$).

It is demonstrated that the shear Alfvén wave can effectively de-trap energetic electrons from the magnetic mirror field in both electron energy ranges.

Due to grad-B and curvature drift, the highly energetic electrons (above 100 keV) form a hot electron ring in the magnetic mirror. Experimental evidence indicates that the ring is deformed in the right-handed (RH) circularly polarized shear Alfvén wave field. Electron losses are observed in both the radial and the axial direction of the mirror field, with modulation at the Alfvén wave frequency. The periodical loss continues even after the termination of the wave.

A test particle simulation is performed, which confirms that the single particle motion of the energetic electrons in the Alfvén wave field is not adequate to explain experimental observations, and the hot electron collective behavior must play a role in the de-trapping effect.

It is proposed that the hot electron ring is deformed due to $\vec{E}_{Alfven} \times \vec{B}_0$ drift in the Alfvén wave field. The ring deformation grows when the electron azimuthal drift matches the rotation of the RH shear Alfvén wave pattern, which generates a collective mode of the ring that degrades its confinement and leads to electron loss from the magnetic mirror.

The dissertation of Yuhou Wang is approved.

Raymond Walker

George Morales

Troy Carter

Walter Gekelman, Committee Chair

University of California, Los Angeles

2013

To my parents

TABLE OF CONTENTS

1 Introduction 1

1.1 Motivations 1

1.2 Fundamental concepts 3

1.3 Summary of results and dissertation outlines 7

2 Experimental Methods 10

2.1 Large Plasma Device. 10

2.2 Rotating Magnetic Field (RMF) antenna 13

2.2.1 Description of the antenna 13

2.2.2 Arbitrarily polarized shear Alfvén wave 17

2.3 Microwave heating source 19

2.4 Diagnostics 23

2.4.1 B-dot probes 23

2.4.2 Langmuir probes 23

2.4.3 Soda-straw probes 24

2.4.4 X-ray scintillation detector 26

2.4.5 X-ray computed tomography 28

2.5 Summary of experiment setup 31

3 Experiment I: De-trapping electrons at the 100 eV energy level 35

3.1 Fast electron generation 35

3.2 Fast electron de-trapping 40

4 Experiment II: De-trapping 100 keV electrons 44
4.1 Generation of a magnetic mirror-trapped hot electron ring 44
4.2 Hot electron de-trapping 49
4.2.1 Independence of ECRH and the de-trapping process 50
4.2.2 Modulated electron loss 51
4.2.3 Alfvén ghost 52
4.2.4 Spatial distribution of the lost electrons 53
4.2.5 Deforming the hot electron ring 56
4.2.6 Dependence of de-trapping on the Alfvén wave polarization . . . 58
4.2.7 X-ray spectrum 60
4.2.8 Whistler waves and electron de-trapping 62

5 Test particle simulation of single particle evolution 64
5.1 Simulation method and setup 64
5.2 Results 68
5.3 Discussion 77

6 Discussion and conclusions 79
6.1 Future work 85

Appendix A: Dot by Dot Reconstruction (DDR)-A novel tomography algorithm 87
Appendix B: Green function calculation of RMF antenna radiation pattern . . 100
Appendix C: Evolution of the hot electron ring in absence of Alfvén waves . . 105
Appendix D: Boris Mover Scheme 111

Bibliography 113

LIST OF FIGURES

Fig 1.1 Diagram of vectors related to a typical shear Alfvén wave. . . . 6

Fig 2.1 A photograph of LaPD. 10

Fig 2.2 (a) Photograph of the RMF antenna. (b) Electrical schematics for each coil of the RMF antenna. (c) Schematic of the variable capacitor bank. (d) Typical current in one coil of the RMF antenna. In this case, the RMF driver is turned on at t = 0 for 20 cycles at f = 115 kHz. After the driver is turned off at t = 0.174 ms the current continue to oscillate with a decaying envelop, showing an underdamped RLC oscillation. 14

Fig 2.3 (a) B field vectors of a shear Alfvén wave measured on a transverse (x-y) plane. Axial current density, calculated by taking the curl of wave magnetic field, is overplotted in color. Only the horizontal coil of the antenna is turned on. (b) A computer graphic portrayal of a shear Alfvén wave generated by the RMF antenna. The antenna is to the lower left of the picture. Both coils are driven at the same frequency with a $\pi/2$ phase delay. Isosurfaces of current density are plotted in red (flowing to the right) and blue (flowing to the left). The white arrows are magnetic field vectors of the wave. A mirrored image is shown on the bottom, which appears to have opposite helicity compare to the original. (Credit: W. Gekelman, UCLA) 16

Fig 2.4 Polarity of a shear Alfvén wave as a function of perpendicular wave number, calculated with a typical experimental condition in the cold plasma approximation. The polarity is characterized by the ratio of $i\tilde{E}_y / \tilde{E}_x$, where $\tilde{E}_x$ and $\tilde{E}_y$ are the complex amplitudes of the wave electric field. It is assumed $\vec{k}_\perp = \vec{k}_x$ in this case. 18

Fig 2.5 (left) Relative power in LH/RH oscillation of the wave B field over a transverse plane. The B field vectors are overplotted for reference. The B field is measured 2 m (0.2 $\lambda_{Alfvén}$) away from the RMF antenna, where it can be considered as the near field region of the antenna. (upper-right) Hodograms of wave magnetic field vectors, at (0,0) and (9,0) cm respectively, running for 5 wave cycles. (lower-right) Horizontal line cut at y = 0, showing percentage power in RH oscillation and amplitude of the wave B field. 19

Fig 2.6 A labeled photograph of the microwave source. Part of the rf sealing is removed temporarily for display. 21

Fig 2.7 A schematic plot of the microwave source. 22

Fig 2.8 Schematics of a "soda-straw probe". 24

Fig 2.9 Cross-sectional drawing of a "soda-straw probe". 26

Fig 2.10 Probability of interactions between x-ray and NaI(Tl) crystal in terms of attenuation coefficient μ that characterize the exponential decay of the intensity of x-rays when travel through matter by $I = I_0 e^{-\mu l}$, where I and I_0 are the intensity

of a monoenergetic beam of x-rays after and before it travels in the matter for a distance of l. Data for the graph is retrieved from National Institute of Standards and Technology (NIST) and calculated with a density of 3.67 g/cm^3 of the NaI(Tl) crystal. 27

Fig 2.11 Transmission rate I/I_0 of a monoenergetic x-ray beam traveling through 3/8 inch stainless steel, where I_0 is the incident beam intensity and I is the exit intensity. 28

Fig 2.12 A drawing of the rotation drive with the detector shielding mounted on it. 30

Fig 2.13 A drawing of the experiment geometry on the transverse x-y plane. The sign of t is defined as the sign of the y-intercept. (b) A map of (t,θ) coverage by the tomography system. The hatched area can be covered with the detector moving only on the positive x side of the vacuum chamber. The uniformly shaded area is added if the detector is moved to the negative x side of the vacuum chamber. 31

Fig 2.14 Schematic of the experiment. The two series of experiments have very similar setup. 33

Fig 2.15 Axial magnetic field profile in the two series of experiments. Z coordinates of the cathode-anode pair, the microwave waveguide and the RMF antenna are marked. The second experiment is conducted at a lower field because the generation of the highly energetic electrons is found to be more efficient at the second harmonic electron cyclotron

resonance (ECR) frequency ($f_{microwaves} = 2 f_{ce}$) compared to at the fundamental ECR frequency ($f_{microwaves} = f_{ce}$) or the upper-hybrid resonance frequency ($f_{microwaves} = f_{UH}$). 33

Fig 3.1 Photographs taken by a camera with 1 us exposure time, aiming along B_0, (a) without microwaves and (b) with microwaves. Plasma near the waveguide is illuminated by the microwaves. The light is generated by fast electrons. The background plasma is Helium. 36

Fig 3.2 Electron impact excitation cross-section for Helium atom, from ground state ($1s^2$) to the lowest excited state (1s1p). Data retrieved from National Institute of Standards and Technology (NIST). 37

Fig 3.3 (left) Ion saturation current measured by a Langmuir probe moving on a small data plane in front of the waveguide. (upper right) geometry showing where the measurement is located. The probe is biased at -70 Volts relative to the vacuum chamber. Fast electrons with energy higher than the bias can be collected by the probe and show up as negative signals. Two contours where the plasma density and local magnetic field result in the upper hybrid frequency matching the microwave frequency are superimposed. 38

Fig 3.4 Comparison of I_{sat} measured with/without the presence of a shear Alfvén wave. Both cases have same microwave heating power shown in panel (a). In one case the shear Alfvén wave

is launched during t = [0.5, 0.7] ms, as shown in panel (b), while in the other case no wave is launched. The hot electron current measured by a Langmuir probe in both cases are shown in panel (c). 41

Fig 3.5 Soda-straw probe current measured before/after injection of a shear Alfvén wave. The negative signal (shown in red), indicates fast electrons of energy more than 80 eV, is reduced significantly by the Alfvén wave. 43

Fig 3.6 Photographs of the light from the fast electrons, taken with/without the presence of a shear Alfvén wave. The bright spot of fast electrons is reduced by the Alfvén wave. . . . 43

Fig 4.1 Experiment timing scheme. 44

Fig 4.2 Ion saturation current measured 96 cm downstream from the magnetic mirror center. The microwave waveguide comes in from – x axis, and its edge is at x = -35 cm at the center plane of the mirror (z = 0). The measurement is made at t = 3 ms after ECRH is turned on. It is worth noting that what is shown here is not the hot electron ring itself, but the by-product that comes with the generation of the ring. 46

Fig 4.3 (a) A schematic plot of the transverse plane at z = 0, showing the relative position of the vacuum chamber, microwave waveguide, the "luminator probe" and the hot electron ring. (b) X-ray flux as a function of luminator probe tungsten tip position at different times during the ECRH. 48

Fig 4.4 Time series of x-ray flux measured with/without the presence of a 100-cycle shear Alfvén wave launched from t = 23 ms to 23.9 ms. 50

Fig 4.5 Overlay of 19 traces of x-ray flux measured with an un-collimated detector (designated A-S), each with a 100-cycle SAW launched at different time delays (marked by an arrow on the top). 51

Fig 4.6 1200 shot averaged signal of the x-ray burst during SAW propagation. Bx of the SAW measured at the center of the magnetic mirror in absence of the ECRH is shown on the bottom trace. 52

Fig 4.7 X-ray flux (un-collimated) and B_y of the Alfvén wave on the machine axis outside the mirror, measured just after the Alfvén wave driver power off. 53

Fig 4.8 X-ray axial tomograms at z = 0. The semi-transparent red rectangles indicating the size and position of the waveguide are superimposed in the plots. The waveguide position is shown as a red rectangle. 54

Fig 4.9 (left, colored) X-ray axial tomograms on the plane where the anode was situated (z = 10.75 m). (right) horizontal line cuts at y = 0 of the two tomograms. 55

Fig 4.10 Temporal history of x-ray flux. The detector is collimated in such way that only x-rays from near either z = 0 plane (black trace) or z = 351.5 cm plane (blue trace) are recorded. A close

up examination of the two traces shows that the oscillations have the same frequency and phase. 56

Fig 4.11 (a) Cartoon of experiment setup, for three cases with different positions of a tantalum paddle inserted from the opposite side of the waveguide. (b) X-rays as function of time measured in the three cases. Antenna current is shown on top for comparison. (c) frequency spectrum of the x-ray signal. The dominant oscillation at f = $f_{Alfvén}$ is suppressed by compensating geometrical asymmetry of the experiment. . . . 57

Fig 4.12 (upper-left) The x-ray flux measured when Alfvén waves of different polarizations are launched. (upper-right) Hodograms of Alfvén wave magnetic field with three different polarities. The hodograms begin at the center when the wave is first turned on at t = 31 ms, and end at t = 31.1 ms ($\Delta t = 11\tau_{Alfven}$). The wave magnetic field is measured by a 3-axis B-dot probe on the machine axis at z = 191.7 cm, by which the polarity of the wave is determined. (bottom) horizontal line-cuts of the upper panel at 3 different LH amplitudes. 59

Fig 4.13 (left) Phase of x-ray modulation at f_{Alfven} as a function of phases of LH and RH component of the Alfvén wave. For ease of comparison, the relative phases are shown with the smallest phases set to 0 deg. (right) Hodograms of Alfvén wave magnetic field with three different phases, measured by a B-dot probe on machine axis at z = 191.7 cm. 60

Fig 4.14 X-ray spectrum measured near the center of the magnetic mirror. 61
Fig 4.15 X-ray spectrum measured at one end of the magnetic mirror. . . 62
Fig 4.16 (Top) current in the RMF antenna. The launched Alfvén wave has 20 cycles at 115 kHz. (Bottom) High frequency electro-static fluctuations that accompany the electron de-trapping process. 63
Fig 4.17 X-ray signal measured when Alfvén wave (115 kHz) or whistler waves (20 ~ 200 MHz) are launched. In both cases a hot electron ring is generated by ECRH on from t = [0,30] ms. The Alfvén wave is on from t = [31.2, 31.37] ms. The whistler waves are turned on from t = [31.2, 31.3] ms. 63
Fig 5.1 Calculated radiation pattern of the RMF antenna on a transverse (x-y) plane Δz = 10.7 m from the antenna. The Alfvén wave E and B field are mostly perpendicular to the background magnetic field direction. 65
Fig 5.2 Comparison of simulated antenna radiation pattern with experimental measurement. 66
Fig 5.3 Axial profile of the magnetic mirror and the simulated Alfvén wave field (only B_x component is shown) in the calculation domain. The RMF antenna is at z = - 435 cm and the wave propagates to the right. The decreasing amplitude of the wave is due to collisional damping in the modeled plasma. . . 67
Fig 5.4 (left col.) Kinetic energy and adiabatic invariants evolution of 10 (color coded) randomly chosen test particles trapped in the

magnetic mirror, in absence of the Alfvén wave. (right col.) Distribution function of 41,521 trapped electrons, compared at the beginning and end of the simulation time. 71

Fig 5.5 Evolution of 10 randomly chosen particles lost by the application of a 0.5 Gauss RH wave. 72

Fig 5.6 Number of lost electrons at 4 different levels of wave amplitude (0.5, 1, 5, 50 Gauss respectively). The apparent threshold value of the wave amplitude for the axial loss (no axial loss is found with waves less than 50 Gauss) is very likely caused by the discretization of the initial electron distribution function. 72

Fig 5.7 Time history of electron loss with application of a 50 Gauss RH wave. 72

Fig 5.8 Evolution of 10 randomly chosen test particles de-trapped in the axial direction by a 50 Gauss wave, with LH or RH polarity respectively. Test particles kinetic energies are well conserved. The 1st adiabatic invariant (magnetic moment μ) is broken by the wave, which causes the violation of higher order adiabatic invariance (J and Φ). The two cases with different wave polarities behave very similarly. 73

Fig 5.9 Kinetic energy and adiabatic invariants evolution of 20 randomly chosen test particles (color coded) that are de-trapped in the radial direction by a 50 Gauss shear Alfven wave. 74

Fig 5.10 Pitch angle distribution function before/after the application of a 50 Gauss Alfvén wave. The loss cone angle of this mirror configuration is also shown. The pitch angle is calculated as the angle between velocity and B_0 when the particle is at the center plane of the mirror trap. Note that in the experiment presented in Chapter 4 there is neither a 50 Gauss Alfvén wave (the real wave amplitude is about 0.5 Gauss), nor electrons with pitch angle close to the loss cone (minimum electron pitch angle is measured to be 56 degree). 75

Fig 5.11 Distribution functions of radial position of electrons guiding center before / after the application of a 50 Gauss Alfvén wave. 75

Fig 5.12 Time history of the electron loss when a 50 Gauss Alfvén wave is applied for 5 cycles. B_x component of the wave at the center of the mirror is also shown for comparison. Current in the RMF antenna is ramped up from zero during t = $[0,1]\times T_{Alfvén}$, and ramped down to zero during t = $[4,5]\times T_{Alfvén}$. 76

Fig 6.1 Frequency of the electron grad-B and curvature drift, as function of electron energy and pitch-angle. The Alfvén wave frequency, shown in light blue, can be matched by the azimuthal drift frequency of electrons with proper combination of energy and pitch angle. The measured minimum hot electron pitch angle in the experiment is 56

degree, which implies that the drift resonance energy range is 100 ~ 300 keV. 82

Fig 6.2 Cartoon of ring displacement due to $\vec{E}\times\vec{B}$ drift, at three phases of the wave. The electric field of the Alfvén wave field is simplified as a uniform rotating field. The original positions of the trapped electron guiding centers in absence of the wave is denoted by doted circles, and the displaced positions due to the wave field are the solid circles. 83

Fig A1 A drawing of the tomography geometry in the transverse x-y plane. The sign of t is defined as the sign of the y-intercept. . . 88

Fig A2 A point source, shown in (a), is measured from different angles θ and different impact parameter to the coordinate origin t. Presented in a $t-\theta$ coordinate, the measurement of a point source forms a curve, as shown in (b). 90

Fig A3 (a) An arbitrary test 2D emissivity. Using DDR method, 2.8×10^4 points are found one by one, to reconstruct the emissivity. The course of the reconstruction is shown in (b) – (e), which contains the first $0.2\times10^4, 1\times10^4, 2\times10^4$ and 2.8×10^4 points. The images on the top row are emissivity profiles, and their corresponding line of sight integrated measurements are shown on the bottom. 96

Fig A4 (a) An artificial test function f(x,y), which is a 2D Gaussian centered at (-20,0). (b) The distribution of 549 points in the

projection space, where the simulated measurement is made for the test. 98

Fig A5 The emissivity f_{rec} reconstructed by 6 different procedures are shown on top: (a) back-projection; (b) least-squares fit with pixel basis; (c) least-squares fit with Fourier-Bessel basis; (d) ART with pixel basis; (e) ART with Fourier-Bessel basis; (f) DDR. Line cuts of f_{rec} at y=0 are shown on the bottom plot with solid lines, and line cut of the test emissivity is plotted with dashed lines. 99

Fig B1 Coordinate system for one coil of the RMF antenna. The Cartesian coordinates that are used in the experiment and the test particle simulation are retained for clarity. 102

Fig C1 Time series of x-rays measured without the presence of Alfvén wave. The ECRH is on from t=0 to 30 ms. It talks about 0.5 ms for the microwaves to completely shut off, which caused the rapid drop of x-ray flux immediately after t=30 ms. After ECRH is completely turned off (t > 31 ms), the x-ray signal shows an exponential decay. This measurement is the same one in Fig 4.5 trace S, but is shown in log scale here. 105

Fig C2 After ECRH is turned off, the x-ray signal shows an exponential decay in the axial and radial loss, both with a decay time about 40 ms. The ECRH is on from t=[0,30] ms. Around t=31 ms, the spike in the x-ray signal is caused by a shear Alfvén wave launched during the time t=[31.2,31.4] ms. . . 110

LIST OF TABLES

Table 2.1 Typical LaPD parameters 12

Table 2.2 Typical parameters in the two series of experiments . . . 34

ACKNOWLEDGEMENT

I am deeply grateful to my advisor, Professor Walter Gekelman, for his valuable guidance and encouragement over the years, for his way of making people laugh and think at the same time, and for setting the example of an extraordinarily energetic physicist. The incredible opportunity to work in his amazing lab has shaped me to be the person I am today, and for that I will be forever thankful. I am also greatly indebted to Dr. Pat Pribyl for providing brilliant ideas and guidance to this project. I have greatly benefited from his tremendous support in electronics, physics, coding, English and so much more.

I owe my heartfelt gratitude to my PhD committee members, Professor George Morales, Professor Troy Carter, and Professor Ray Walker, for their careful review of this dissertation and for the inspiring questions and suggestions that, in a way, made the graduation experience worthwhile. George taught me the best plasma physics courses I ever had, and his lecture notes have been my best reference in the past five years. Troy has always been so generous in sharing his in-depth knowledge of plasma physics and in giving me encouragement.

Big thanks to the superb scientists and staffs at BaPSF for their valuable help: to Dr. Steve Vincena for the tremendous work of keeping LaPD running and being an excellent scientist at the same time; to Dr. James Maggs, Dr. Shreekrishna Tripathi, and Dr. Bart Van Compernolle for answering any question I had about plasmas and being ready to provide technical support at any time; to Meg Murphy for guiding me through bureaucracies with ease; to Dr. Zoltan Lucky and Marvin Drandell who know how to build everything and

tried to teach me about it; and to Mio Nakamoto for the tiny delicate probes and beautifully interfaced electronics that one day may go to an art museum after their retirement from the lab.

My sincere gratitude goes to the senior graduate students Dr. Eric Lawrence, Dr. Andrew Collette, Dr. Brett Jacobs, Dr. Dave Auerbach, and Dr. Chris Cooper for teaching me everything I need to know to work efficiently in this lab. Each of them has been a model graduate student to me. I miss them and wish I had more time with them.

I was very fortunate to have the companion of awesome peers. I thank Dr. Seth Dorfman for his contagious enthusiasm for science and for sharing his graduation experience; Nathaniel Moore for his unfailing jokes; Mike Martin for being the most considerate person I have ever met; Jeff Bonde for numerous interesting discussions of plasmas or anything else in the universe; Tim DeHaas, who shares the same cubical with me and is able to put up with that, for making my life musical; Giovanni Rossi, Danny Guice, and Alexandra Latshaw for making me feel so much younger.

I would like to thank the ONR MURI grant and Professor Papadopoulos (Univ. of Maryland) for providing funding to this project, which made this dissertation possible.

And, of course, I need to thank beautiful southern California. It is just hard to feel bad here. Sometime I wonder if I'd like to be a biologist or even an artist had I grown up in this exotic park rather than a forest of concrete. Moreover, the easygoing and friendly people here made my stay really enjoyable.

I thank my unorthodox parents who have always been providing a different point of view. I remember they complained about excessive homework so much more often than myself did when I was growing up (which is rare for Chinese parents); now I am very happy to dedicate this dissertation to them as my very last homework assignment. Finally, I would like to thank my sweetheart, Dr. Jie Zhang, for giving me a home whenever I needed one, for understanding my somewhat solitary life style, for having faith in me, and for being a fantastic chef. I feel very lucky to have such a family; their endless patience, support, and love make me floating on the clouds every day.

Yuhou Wang

Nov 24, 2013

VITA

2003–2007	B.S. Applied Physics University of Science and Technology of China Special Class for the Gifted Young
2007-2009	Teaching Assistant Department of Physics University of California, Los Angeles
2007-2009	M.S. Physics University of California, Los Angeles
2009-2013	Graduate Student Researcher Department of Physics University of California, Los Angeles

PUBLICATIONS

Y. Wang et al. "Scattering of magnetic mirror trapped fast electrons by a shear Alfvén wave." Physical Review Letters. 108, 105002 (2012).

Y. Wang et al. "Hard x-ray tomographic studies of the destruction of an energetic electron ring." Review of Scientific Instruments. v84, 053503 (2013).

A. Karavaev et al. "Generation of shear Alfvén waves by a rotating magnetic field source: Three-dimensional simulations." Physics of Plasmas. v18, 032113 (2011).

H. Wang et al. "Monopole antenna probe for density measurements in cold plasmas." Plasma Science and Technology. 13, 197 (2011).

CHAPTER 1

Introduction

1.1 Motivations

Highly energetic electrons in the Earth's radiation belts are frequently referred to as "killer electrons" for their ability to cause fatal radiation damage to satellites. This killer electron flux naturally exists as observed by extensive satellite measurements since the discovery of the radiation belts. These electrons can come from naturally occurring events such as geomagnetic storms driven by corotating interaction regions (CIRs) or coronal mass ejections (CMEs) directed toward the Earth. Accidental or deliberate human activity such as High Altitude Nuclear Explosions (HANE), can also cause enhancement by several orders of magnitude of the MeV electron flux trapped in the inner radiation belt, leading to catastrophic failure of the Low Earth Orbiting (LEO) satellites [Dupont 2004]. A 1962 exoatmospheric nuclear test ("Starfish Prime") produced an artificial radiation belt with an intense electron flux, and it took almost 10 years before the natural dynamic equilibrium of the radiation belts was restored [Beall 1967]. One-third of the entire satellite fleet in low earth orbit at the time was disabled.

The need for protection of the space satellite infrastructure is receiving increasing attention in recent years with the fast growing application of satellite technology, represented by $177.3 billion revenue of the global satellite industry in 2011, and an average annual growth rate of 10.7% for the past decade [SIA 2012]. Passive actions to cope with the everyday hostile environment of space

have already been taken, such as the expensive practice of radiation hardening and redundancies in the electronics to prolong their lifetime. There is a great deal of current interest in developing artificial techniques to mitigate extraordinary energetic charged particle flux [Inan 2003]. The topic has come to be known as "Radiation Belt Remediation" (RBR).

One promising strategy is enhancing electron precipitation by injecting whistler mode VLF (Very-Low-Frequency) waves, which are gyro-resonant with the electrons and pitch-angle scatter them to lower altitude into the atmosphere [Sauvaud 2008]. Another less discussed possibility is injecting Alfvén mode ULF (Ultra-Low-Frequency) waves to drain or re-direct the energetic particles. In this dissertation, we performed a laboratory experiment in which a population of energetic electrons is trapped in a magnetic mirror field and subsequently irradiated by a shear Alfvén wave. It is observed that the low frequency ($f<f_{ci}$, f_{ci} is the ion cyclotron frequency) Alfvén wave dramatically affects the confinement, and the trapped electrons are scattered out of the magnetic mirror.

Aside from remediation, this study is of general interest for space science. For example, one unanswered, fundamental question is, which mechanism is primarily accounted for the natural loss of electrons in the radiation belt [Horne 2003]? Of special interest is the dramatic drop of relativistic electron flux during geomagnetic storms when the electron flux is decreased by several orders of magnitude within hours [Bortnik 2006] [Turner 2012]. Possible explanations include pitch-angle scattering through wave-particle interactions [Thorne 1971] [Millan 2007], magnetopause shadowing [West 1972] [Ohtani 2009], rapid outward radial transport [Brautigam 2000] [Shprits 2006], to name a few. To

answer such a question, detailed understanding of each of these processes is required. These processes are usually tangled in the space environment because they can occur simultaneously. It is difficult to evaluate the effectiveness of any single process, or even identify causality in this uncontrolled environment. Controlled laboratory experiments can separate these processes, and provide opportunities to study them in great detail, one-by-one. This experiment was designed to study the response of mirror-trapped electrons to a low frequency electromagnetic (EM) wave. This fundamental process involves phenomena such as the depletion of radiation belt electron flux [Loto'aniu 2010] [Brito 2012] [Degeling 2013], acceleration of energetic electrons in the radiation belts [Elkington 1999] [O'Brien 2003], and the modulation of VLF emissions [Sato 1974] to name a few.

1.2 Fundamental concepts

Magnetic mirrors and adiabatic invariants

Magnetic mirrors are configurations that the magnetic field lines are compressed at two points, so that the field strength varies along the field lines. The ratio of the maximum to minimum field strength is defined as the mirror ratio $R_{mirror} = B_{\max} / B_{\min}$. Charged particles can be trapped in the mirror field if they have enough velocity perpendicular to the magnetic field, otherwise they cannot be confined. The pitch angle (the angle between particle's velocity and B_0) below which the particle is not confined is known as the "loss cone angle", and is related to the mirror ratio by $\theta_{losscone} = \tan^{-1}(1/\sqrt{R_{mirror}})$.

The motion of charged particles in a magnetic mirror can be most easily described by three periodic motions of different time scales (with an order from

the fastest to the slowest): the gyro-motions, the axial bounce between the mirror points, and the azimuthal drift due to the grad-B and curvature drift. Three adiabatic invariants are associated with these periodical motions: the magnetic moment, the longitudinal invariant and the flux invariant:

$$\mu = \frac{p_\perp^2}{2mB}, \tag{1.1}$$

$$J = \int_{bounce} p_\parallel ds, \tag{1.2}$$

$$\Phi = \int_{drift} B dS, \tag{1.3}$$

where m and p are the particle's mass and perpendicular momentum, B is the magnetic field strength, the integral in J is along the guiding center's motion on a field line between the two mirror points, and the integral in Φ is over the surface enclosed by the drift orbit of the guiding center.

Shear Alfvén waves

Shear Alfvén waves are electromagnetic waves propagating in magnetized plasmas at frequencies below the ion cyclotron frequency (f_{ci}) in single species plasma. They have been observed as ULF magnetic fluctuations of the Earth's magnetic field as early as 1861 [Kivelson 1995], however they were not understood until Hannes Alfvén first predicted their existence theoretically in 1942 [Alfvén 1942]. Since then shear Alfvén waves have been generated in laboratories and their frequent occurrences in a wide variety of natural environments are studied.

The phase speed of the Alfvén wave (to the first order approximation) is known as the Alfvén velocity, $v_A = B/(4\pi n_i m_i)^{1/2}$. The dispersion relation of

shear Alfvén wave can be concisely expressed in two limits $v_A \gg v_{th,e}$ and $v_A \ll v_{th,e}$ ($v_{th,e}$ is the electron thermal speed), in which the wave is known as inertial Alfvén wave [Gekelman 1994] [Morales 1994] and kinetic Alfvén wave [Gekelman 1997] [Morales 1997] respectively:

($v_A \gg v_{th,e}$, inertial Alfvén wave) $$\frac{\omega^2}{k_{\parallel}^2} = v_A^2(1-\omega^2/\Omega_{ci}^2)/(1+k_{\perp}^2\delta^2) \tag{1.4}$$

($v_A \ll v_{th,e}$, kinetic Alfvén wave) $$\frac{\omega^2}{k_{\parallel}^2} = v_A^2(1-\omega^2/\Omega_{ci}^2 + k_{\perp}^2\rho_s^2) \tag{1.5}$$

Here ω and k are the wave frequency and wave number, Ω_{ci} is the ion cyclotron frequency, the electron skin depth is defined as $\delta = c/\omega_{pe}$ (ω_{pe} is the electron plasma frequency), and ρ_s is the ion sound gyro-radius $\rho_s = c_s/\Omega_{ci}$ ($c_s = (T_e/M_i)^{1/2}$ is the ion sound speed).

Unlike electro-magnetic waves in vacuum, the non-isotropic response of a magnetized plasma to electro-magnetic field fluctuations gives shear Alfvén wave special directionality. The magnetic field of a shear Alfvén wave is predominantly perpendicular to the background field. For obliquely propagating waves ($k_{\perp} \neq 0$) the electric field vector is co-planar with the wave vector, and the parallel electric field is much smaller than the perpendicular component. In most cases the wave perpendicular wave number is much larger than the parallel wave number, which leads to the phase fronts moving primarily in the perpendicular direction. However the direction of the energy flow, i.e. the group velocity of the wave, is mostly along the background field. As an example, the geometric relationships of a typical shear Alfvén wave are illustrated in Fig 1.1.

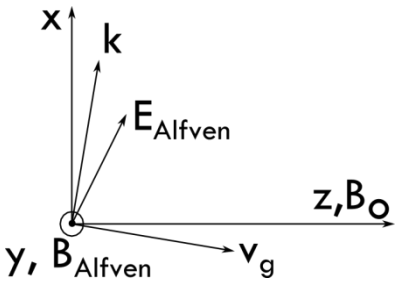

(Not shown to scale)

Fig 1.1 Diagram of vectors related to a typical shear Alfvén wave.

Rotating Magnetic Field source

The Rotating Magnetic Field (RMF) source is an innovative method for efficiently generating waves in plasmas [Karavaev 2010]. The simplest RMF source can be considered as a permanent or superconducting magnet rotating at certain rate ω in a magnetized plasma. Waves in the plasma can be excited when the background magnetic field is perturbed by the magnetic field of the magnet at a proper frequency ω.

An important application of the RMF source is as space-borne ULF/VLF antennas with the implication of radiation belt remediation. In the space environment, for example in the L=2 layer in the magnetosphere, the background magnetic field is on the order of micro-Teslas (μT) and the proton cyclotron frequency is on the order of tens of Hertz. It is possible to mechanically rotate a magnet at a rate near this range. For a higher frequency range, such as in the laboratory, the RMF can be created by a pair of concentric orthogonal coils [Gigliotti 2009] [Karavaev 2011]. When the two coils are driven by rf current at the same frequency with a π/2 phase delay, the induced

magnetic field at the center of the coils rotates at the frequency of the rf current, thus generating waves in the same way as that by a rotating magnet.

1.3 Summary of results and dissertation outlines

This dissertation investigates the loss of fast electrons from a magnetic mirror trap when irradiated by a shear Alfvén wave generated by a RMF source. Two series of experiments are performed, characterized by the different energy levels of the targeting electrons to be de-trapped (at ~100 eV and ~100 keV respectively). In the first series of experiment, electrons with large perpendicular energy (~100 eV) are produced by a short pulse of low power microwaves (f = 2.45 GHz, P = 5 kW, dt = 3 ms) at the upper-hybrid frequency $f_{uh} = (f_{ce}^2 + f_{pe}^2)^{1/2}$, and trapped in a magnetic mirror field (length = 3.5 m, mirror ratio $\approx$1.6). A shear Alfvén wave ($\delta B/B_0 \approx 0.1\%$, $\lambda_{||} \approx 9$ m) is launched by a RMF antenna axially 2 m away from the center of the mirror. It was observed that the Alfven wave effectively eliminated the trapped electrons. This effect is observed via different diagnostics (Langmuir probes, "soda-straw" probes, and visible light photography). Plasma density and temperature perturbations from the Alfvén wave are observed along with the scattering. In the second series of experiments, a hot electron ring along with hard x-rays of energies of 100 keV – 3 MeV, is generated by 2nd harmonic electron cyclotron resonance heating [Ikegami 1967] and is trapped in a magnetic mirror field (mirror ratio ≈ 1.8). Shear Alfvén waves are launched with a RMF antenna with arbitrary polarization. Irradiated by the Alfvén wave, the loss of electrons is modulated at $f_{Alfvén}$. The periodic loss of electrons is found to be related to the spatial distortion of the hot electron ring, and continues even after the

termination of the wave. The effect is found to be caused only by the right-hand (electron diamagnetic direction) circularly polarized component of the Alfvén wave. Hard x-ray tomography, constructed from more than 1000 chord projections at each axial location, shows electrons are lost in both the radial and axial direction. X-ray spectroscopy shows electrons over a broad range of energy are de-trapped by the Alfvén wave, which suggests the non-resonant nature of the de-trapping process. The de-trapping process is found to be accompanied by electro-magnetic fluctuations in the frequency range of 1~5 f_{LH}, which are also modulated at the frequency of the Alfvén wave. To exclude the possible role of whistler waves in this electron de-trapping process, whistler waves at these frequencies are launched with an antenna in absence of the Alfvén wave and no significant electron loss found.

A test particle simulation is performed to examine the single particle motion of magnetic mirror trapped electrons in the field of a shear Alfvén wave, by numerically integrating their relativistic equations of motion using a Boris Mover [Decyk 2007]. The background magnetic mirror field used in the simulation is the same configuration as in the second series of experiments. The volumetric electro-magnetic field of the Alfvén wave is obtained by numerical calculation of the antenna radiation pattern following a Green function method described in [Bamber 1995], and has been verified by comparison with experimental measurements with a difference of less than 10%. The motions of 94,622 test particles, initially uniformly distributed in phase space, are tracked in a calculation box of 85 cm × 85 cm × 8 m, for a period of 10 Alfvén wave cycles. From this numerical study, we conclude that the motion of single electrons in the Alfvén wave field is not adequate to explain experimental

observations; therefore the interactions between the fast electrons must play a role in the electron de-trapping effect.

A collective electron loss mechanism is proposed, which is based on the experimental observation of the deformation of the hot electron ring in the field of the shear Alfvén wave. It is conjectured that the non-uniform wave field pattern distorts the spatial shape of the ring via the $\vec{E}_{Alfven} \times \vec{B}_0$ drift. The ring deformation grows when the electron azimuthal drift matches the rotation of the shear Alfvén wave pattern. The 3D non-uniform charge density can build up a global electric field, which generates a collective mode of the ring that degrades its confinement and leads to electron loss from the magnetic mirror.

This dissertation is organized as follows. **Chapter 1** motivates the experiment, and introduces some key concepts involved in this dissertation. **Chapter 2** describes the experimental method to generate and trap an energetic electron population and to launch arbitrarily polarized shear Alfvén waves. The diagnostics and data acquisition method adapted in the experiment is also described in this chapter. The two series of experiments are described in **Chapter 3 and 4** respectively. **Chapter 5** presents a test particle simulation which examines the single particle motion of magnetic mirror trapped electrons in the field of a shear Alfvén wave. **Chapter 6** summarizes and concludes the dissertation with analysis of possible theoretical conjectures of the de-trapping process.

CHAPTER 2

Experimental methods

2.1 Large Plasma Device

The experiment is performed at the Large Plasma Device (LaPD) at the University of California, Los Angeles. The device creates highly uniform magnetized plasma of large physical size, which makes it an ideal platform to study Alfvén wave related phenomenon. One can find a detailed description of the device in [Gekelman 1991], as well as recent updates at the website of Basic Plasma Science Facility (BaPSF) [Bapsf website]. We will give a brief explanation of how this machine works, with typical parameters listed at the end of this section.

Fig 2.1: A photograph of LaPD.

Shown in Fig 2.1 is a photograph of LaPD. The most visible parts of the machine are a cylindrical stainless steel vacuum vessel surrounded by yellow and purple solenoidal electro-magnets. Vacuum is required for plasma production to reduce neutral density and to keep a low level of impurities. The vacuum is maintained by four turbo pumps located at the two ends of the machine. Gas is fed to the vessel near the middle of the machine, with flow rate regulated by a piezoelectric valve with feedback from readings of an ion gauge, to achieve an operating gas pressure set by the experimenter. The fill gas can be a mixture of different species (H_2, He, Ne, or Ar), and the concentration of each species is adjusted by mass flow controllers. The partial pressures of different gas species in the vacuum chamber are monitored by a residual gas analyzer (RGA). The yellow and purple coils shown in Fig 2.1 provide a strong steady-state background magnetic field. Because of the large current (~ kA) required to create such a strong field, the coils are made with heavy gauge extruded copper bar which has water cooling channel inside. The coils are divided into 10 sets along the axial direction and driven by independently programmable power supplies, thus provide capability of generating a flexible axial field profile. The cooling water connections and the brass bus bars running between the coils and their power supplies are also visible in Fig 2.1.

A cathode-anode pair is located at one end of the machine to deliver the plasma discharge power. The cathode material has a low work function (barium oxide coated on a nickel plate) and is heated to increase electron emission from its surface $I_{emission} \sim 3A/cm^2$). The anode is a semi-transparent wire mesh located about 50 cm away from the cathode. When a discharge voltage is applied between the cathode and the anode, the emitted electrons

gain energy from the electric field, and ionize the fill gas to create plasma. The discharge voltage, typically lasts for 10 ms, and is switched on and off rapidly by solid state transistors. After the removal of the discharge power the plasma becomes highly quiescent and the density slowly decays (at timescales of about 10 ms). This is referred to as the "afterglow plasma".

The discharge is created repeatedly once every second, and the plasma is highly reproducible. The repeatability of the experiment enables convenient ensemble average over multiple plasma shots, as well as the reconstruction of volumetric data from a single movable probe measurement. For such a dataset, the traversal of the probe through all grid points in the volume is conducted by an automated probe drive (also visible in Fig 2.1) under the control of a computerized data acquisition system. At each grid point, the probe signal is A/D converted by a digitizer triggered at a fixed time relative to the discharge pulse.

Vacuum chamber size	1 m diameter, 20.7 m long
Gas pressure	5×10^{-5} Torr (fill), 5×10^{-7} Torr (base)
Background magnetic field	400-3500 Gauss, variable profile
Discharge pulse	40-70 V, 2-5 kA, 5 – 15 ms
Plasma size	60 cm diameter, 17 m long
Plasma density	1×10^{12} cm^{-3} (discharge), 5×10^{11} cm^{-3} (afterglow)
Electron temperature	6 eV (discharge), 1 eV (afterglow)
Ion temperature	1 eV (discharge), 0.1 eV(afterglow)

Table 2.1: Typical LaPD parameters

2.2 Rotating Magnetic Field (RMF) antenna

2.2.1 Description of the antenna

The shear Alfven wave in this experiment is launched by a Rotating Magnetic Field (RMF) antenna. A detailed description of the antenna and the radiation pattern can be found in [Gigliotti 2009]. Here we give a brief summary to facilitate the readers.

The antenna is composed of 2 orthogonal coils with diameters of 8 cm and 9 cm. Each coil is constructed with three turns of 0.25 cm diameter solid copper wire, and coated with epoxy for insulation. A photograph of the antenna is shown in Fig 2.2(a). Each of the two coils has an independent RLC resonant circuit (necessary to generate high amplitude rf current) using the inductance of the coil (L_0) and the inherent line resistance (R_0), as shown in Fig 2.2(b). The mutual inductance of the two coils is negligible because the two coils are orthogonal to each other. The circuit is made symmetric so that the center of the coil is at the lowest potential. The resonance frequency is matched by tuning the capacitance (C) in the circuit with variable capacitor banks of 1.27 uF with 0.01 uF precision (Fig 2.2c). The circuit is capable driving sinusoidal current burst, in frequency range of 50 ~ 500 kHz with maximum 500 A peak-to-peak amplitude. A typical current driven in one coil, measured by a Rogowski coil, is shown in Fig 2.2(d).

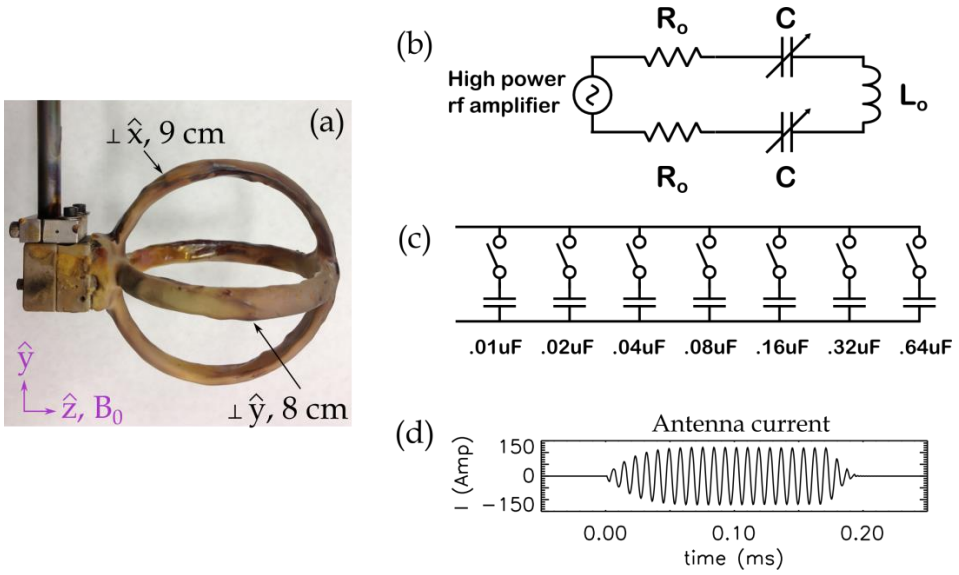

Fig 2.2: (a) Photograph of the RMF antenna. (b) Electrical schematics for each coil of the RMF antenna. (c) Schematic of the variable capacitor bank. (d) Typical current in one coil of the RMF antenna. In this case, the RMF driver is turned on at t = 0 for 20 cycles at f = 115 kHz. After the driver is turned off at t = 0.174 ms the current continue to oscillate with a decaying envelop, showing an underdamped RLC oscillation.

The RMF antenna is placed on the magnetic axis of the machine with two coils normal to x and y direction (Fig 2.2a). Each coil is capable of driving an Alfvén wave individually. Fig 2.3 (a) shows a typical magnetic field pattern of the Alfvén wave radiated by powering only the horizontal coil ($\perp \hat{y}$). By taking the curl, the B field pattern shows two induced current channels of opposite directions, mirroring the axial rf current driven in the coil which peak at (x,y) = (- 4, 0) cm and (4, 0) cm.

When both coils are powered, it is typical to drive an rf current of the same frequency with a $\pi/2$ phase delay between them. The amplitude of the

coil current is adjusted so that waves radiated by each coil individually have the same amplitude. In this case, the superimposed wave pattern rotates. Fig 2.3 (b) is a computer graphic portrayal of such rotating wave pattern, generated using 3D volumetric measurements of the wave magnetic field. The two helical current channels winding each other, and rotate together left-handedly with respect to $\hat{z}$ at the wave frequency as time advances. The overall wave pattern is well collimated along the background magnetic field lines. The dispersion relation of shear Alfvén wave has been verified by [Gigliotti 2009] for the wave radiated by the RMF antenna in a uniform plasma for frequencies below 0.93 f_{ci}.

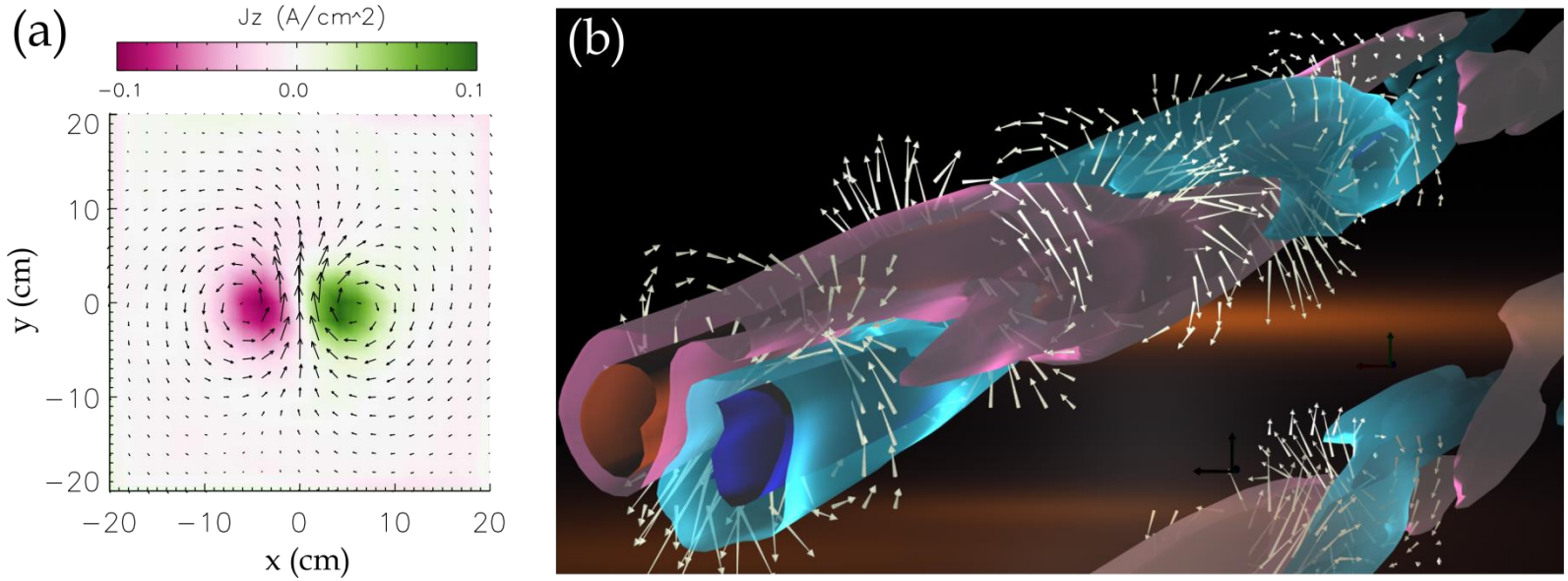

Fig 2.3: (a) B field vectors of a shear Alfvén wave measured on a transverse (x-y) plane. Axial current density, calculated by taking the curl of wave magnetic field, is overplotted in color. Only the horizontal coil of the antenna is turned on. (b) A computer graphic portrayal of a shear Alfvén wave generated by the RMF antenna. The antenna is to the lower left of the picture. Both coils are driven at the same frequency with a $\pi/2$ phase delay. Isosurfaces of current density are plotted in red (flowing to the right) and blue (flowing to the left). The white arrows are magnetic field vectors of the wave. A mirrored image is shown on the bottom, which appears to have opposite helicity compare to the original. (Credit: W. Gekelman, UCLA)

2.2.2 Arbitrarily polarized shear Alfvén wave

A parallel propagating (perpendicular wave number $k_\perp = 0$) shear Alfven wave is left-handed circularly polarized. As the wave propagation becomes more oblique (increasing $k_\perp$), the wave become linearly polarized in the direction of $\vec{k}_\perp$. Both polarities have been experimentally generated, such as in [Maggs 2003] [Gekelman 1994]. Calculated using a typical experimental condition, the polarity of the shear Alfvén wave as a function of $k_\perp$ is shown in Fig 2.4. Using a half perpendicular wavelength of the 9 cm antenna size, the characteristic $k_\perp$ of the wave generated by the RMF antenna is 0.35 cm^{-1}, thus the Alfvén wave is intrinsically linearly polarized. Waves in these calculations are considered as eigenmodes, which are plane waves with fixed wave numbers and frequencies. Arbitrarily polarized waves can be generated by combining these eigenmodes. Each coil of the RMF antenna generates an Alfvén wave, dominantly linearly polarized in x and y direction respectively, at the same frequency with a controllable phase delay, to achieve an arbitrary polarity of the superimposed wave field.

Because in this experiment the Alfvén wave is diagnosed mainly by magnetic probes, we quantify the polarization state by the complex amplitude $\tilde{B}$ of the wave magnetic field, which gives the physical field by $B = \mathrm{Re}(\tilde{B}e^{-i\omega t})$. It is most convenient to write $\tilde{B}$ as a combination of two waves linearly polarized in x and y direction: $\tilde{B} = \tilde{B}_x\hat{x} + \tilde{B}_y\hat{y}$, where $\hat{x}$ and $\hat{y}$ are waves of unit amplitude linearly polarized in x and y direction respectively. $\tilde{B}_x$ and $\tilde{B}_y$ are complex amplitudes in x and y direction, and can be calculated from direct probe measurement.

It is also useful to write $\tilde{B}$ as a combination of two circularly polarized waves: $\tilde{B} = \tilde{B}_{RH}\hat{r} + \tilde{B}_{LH}\hat{l}$, where $\hat{r}$ and $\hat{l}$ are waves of unit amplitude circularly polarized in the right-handed (RH) and left-handed (LH) directions respectively. The two bases follow a simple conversion relation: $\hat{r} = \frac{1}{\sqrt{2}}(\hat{x} + i\hat{y})$, $\hat{l} = \frac{1}{\sqrt{2}}(\hat{x} - i\hat{y})$.

The radiation pattern of the RMF antenna exhibits a dominant polarity state over the region where the wave field is strongest (main lobe). Fig 2.5 shows the polarization state of the field vectors for a case when the rf current driven in one loop 90 degree out of phase with the other. Over the area in the center where the amplitude of the wave peaks the rf field is all right-handed circularly polarized. It is interesting to note that outside the main lobe the polarization of the rf field changes albeit at much lower amplitude. To avoid confusion, for the following of this dissertation the polarity of the Alfvén wave is defined as the polarity of its magnetic field on the machine axis with respect to the background magnetic field direction.

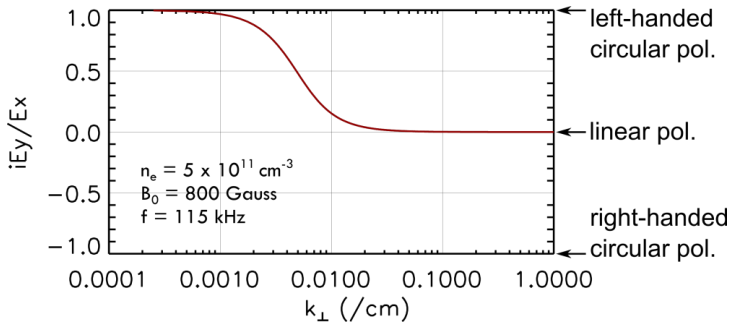

Fig 2.4: Polarity of a shear Alfvén wave as a function of perpendicular wave number, calculated with a typical experimental condition in the cold plasma approximation. The polarity is characterized by the ratio of $i\tilde{E}_y / \tilde{E}_x$, where $\tilde{E}_x$

and $\tilde{E}_y$ are the complex amplitudes of the wave electric field. It is assumed $\vec{k}_\perp = \vec{k}_x$ in this case.

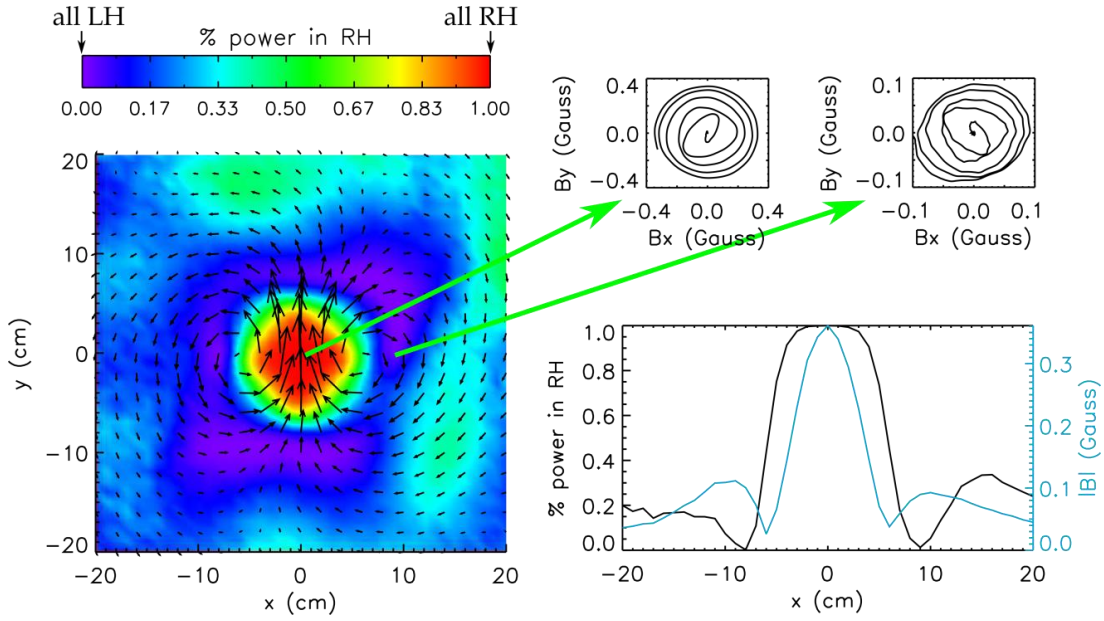

Fig 2.5: (left) Relative power in LH/RH oscillation of the wave B field over a transverse plane. The B field vectors are overplotted for reference. The B field is measured 2 m (0.2 $\lambda_{Alfvén}$) away from the RMF antenna, where it can be considered as the near field region of the antenna. (upper-right) Hodograms of wave magnetic field vectors, at (0,0) and (9,0) cm respectively, running for 5 wave cycles. (lower-right) Horizontal line cut at y = 0, showing percentage power in RH oscillation and amplitude of the wave B field.

2.3 Microwave heating source

A pulsed high power microwave source is used to energize mirror-trapped electrons in this experiment. Fig 2.6 and 2.7 are a photograph and a block diagram of this source. The source is based on a 25 kW CW S-band

Magnetron (Model CWM-30S by California Tube Laboratory), which was the highest power rating CW magnetron commercially available at the time the experiment was designed. The frequency of the output microwaves is determined by the size of the resonance cavities in the magnetron, which is 2450±10 MHz for this magnetron.

The magnetron's cathode is biased by a dc high voltage switching power supply. A pulsed low amplitude 25 kHz switching burst is generated by a FPGA (Field Programmable Gate Array) gate logic board, then power amplified by four Isolated-gate bipolar transistors (IGBT, rated 1200V, 200A) connected in an H-bridge configuration. Their output is stepped-up by four 1:20 transformers with primaries in parallel and secondaries each separately connected to its own full wave diode bridge rectifier (made from 40 fast switching diodes each rated for 1200V, 15A) followed by a high-voltage capacitor (6.3 kV, 0.5uF). The four separate pulsed DC output stages are then connected in series. The power supply has been reliably operated at 20 kV / 3 A, for a pulse duration of 1~100 ms.

The cathode of the magnetron is heated by ~50 Amp ac current, powered by an electrically isolated variable ac power supply. This magnetron uses an electro-magnet to generate the magnetic field, which is driven by an adjustable DC power supply. Water and air cooling are applied to the anode, the electro-magnet and the cathode HV connection, as shown in Fig 2.6. The water flow is interlocked to the cathode heater to prevent rapid destruction of the magnetron in the event of a cooling water supply failure. The majority of the assembly is mounted inside a convenient platform which is rf sealed to prevent leakage of harmful radiation and to block access to dangerous high voltage.

The microwaves generated from the magnetron are launched from a rectangular waveguide (WR430 waveguide). A microwave circulator (2.4~2.5 GHz, 1 kW CW) with a high power water dummy load (50 kW CW) is installed directly at the output of the launching waveguide. The circulator (rated VSWR 1.2) directs any reflected microwaves to the water load, thus prevents power reflection back to the magnetron. A rectangular to circular waveguide converter is used to provide gradual transition of the waveguide geometry. The converter is machined out of a solid aluminum cylinder (8 inch diameter 12 inch long) using electric discharge machining (EDM). The forward power is introduced to the LaPD chamber by a 10 cm diameter cylindrical waveguide through a water cooled ceramic vacuum sealing window, which is designed with the aid of a freely available FDTD (finite-difference time-domain) simulation software package [Oskooi 2010]. The microwave source is typically operated at a pulsing mode with peak output power of 10 kW.

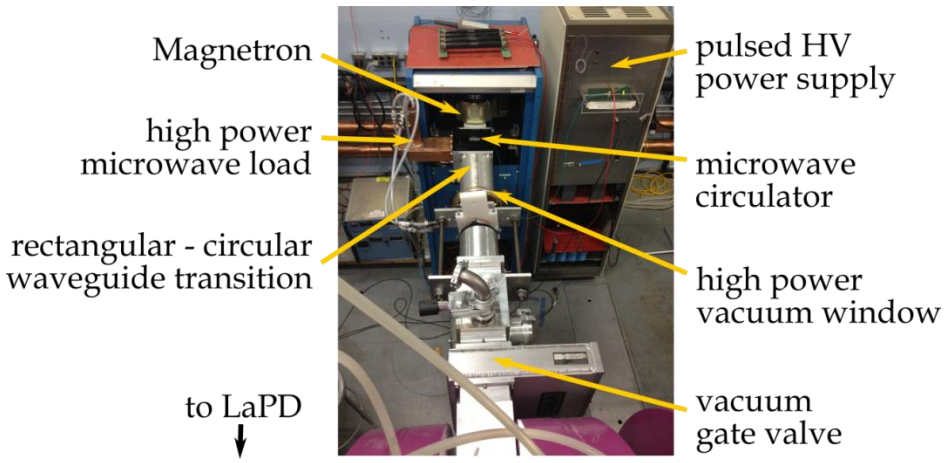

Fig 2.6: A labeled photograph of the microwave source. Part of the rf sealing is removed temporarily for display.

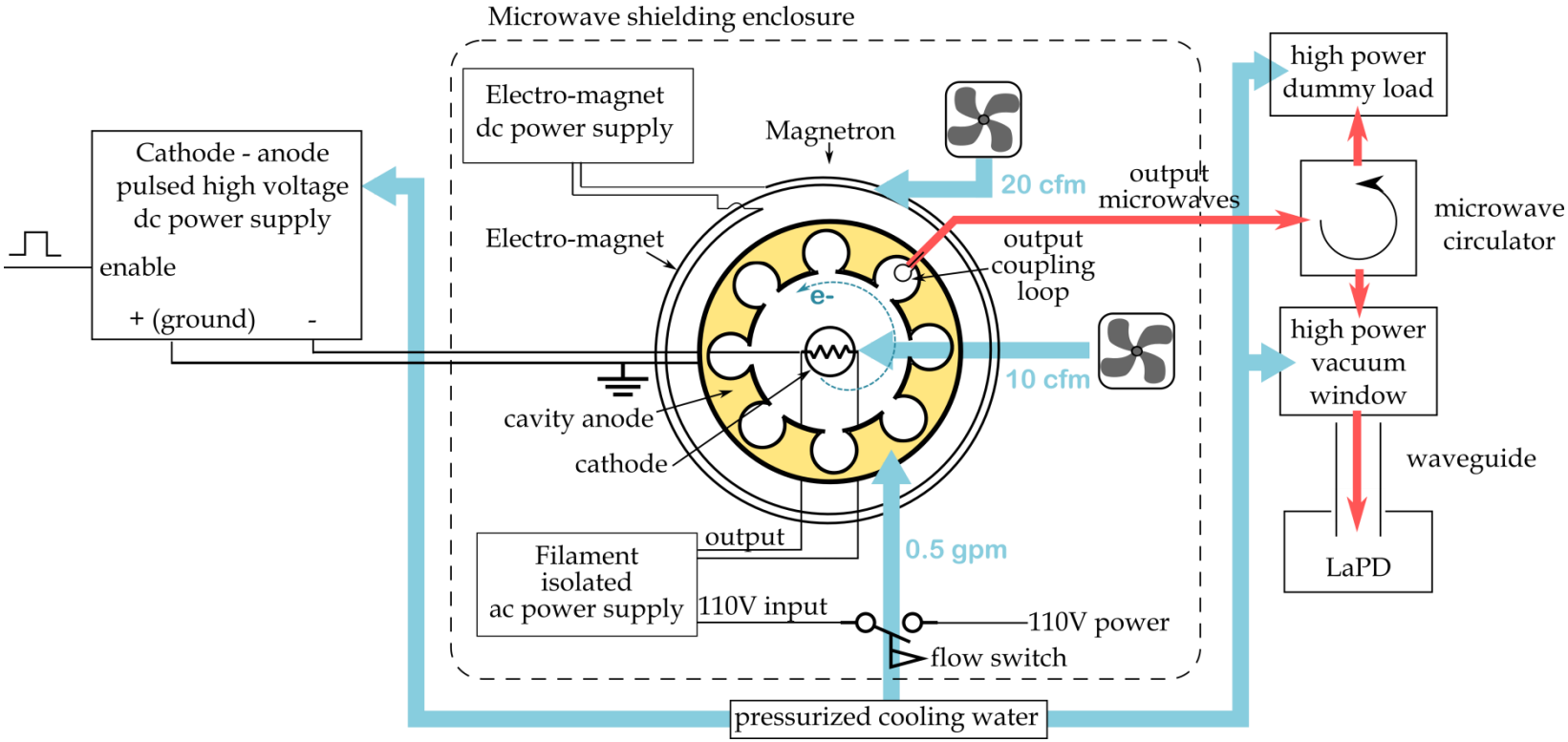

Fig 2.7: A schematic plot of the microwave source.

2.4 Diagnostics

2.4.1 B-dot probes

B-dot probes make localized measurement of time-varying magnetic field, by measure the EMF generated by changing magnetic flux through the coils in the probes, i.e. $V = -A\dot{B}$ (here V is the EMF, A is the effective area of the coil, and B is the magnetic field component that parallel to the normal of the coil). They are standard diagnostics to many plasma physics experiments [Hutchinson 2005]. In this experiment B-dot probes are used to measure the magnetic field of the Alfvén waves.

The B-dot probe used in this experiment consists of three orthogonal coils wound around the six sides of a 3 mm cube. Each coil has 10 turns, and is differentially wounded to eliminate common mode noise. The probe head is covered with a glass dome to insulate it from the plasma. The spatial resolution of the probe, limited by the probe size, is about 5mm. The frequency response of the probe is investigated with a network analyzer and is found to be linear up to approximately 10 MHz, which is well above the frequencies of interest in this experiment. Details about the construction and calibration procedures for the B-dot probe used in this experiment have been well described in [Everson 2009] [Lawrance 2010] and [Cooper 2012].

2.4.2 Langmuir probes

A Langmuir probe is a small conductor immersed in plasma to collect electron and ion current at various probe bias voltages. In a Maxwellian plasma, information about plasma density, electron temperature and plasma potential can be obtained from the probe current – voltage response (also known as I-V

curve). As one of the most widely used plasma diagnostics, detailed description of the probe measurement theory (for various types of Langmuir probes used in different types of plasmas) can be found in numerous publications such as [Lieberman 1994] and [Chen 2003].

The Langmuir probe used in this experiment consists of a small 1 mm x 3 mm tantalum plate situated on the tip of a 3 mm diameter ceramic rod. The probe is usually biased at a negative potential (~ -70 V) relative to the anode, which repels nearly all thermal electrons to collect ion saturation current. In a Maxwellian plasma, the ion saturation current I_{sat} is proportional to $n_e\sqrt{T_e}$.

2.4.3 Soda-straw probes

A novel "soda-straw probe'' was developed for this experiment to measure the trapped electron population with large perpendicular energy. The probe has a copper wire recessed into a ceramic tube as schematically pictured in Fig 2.8. The copper wire is retractable with a micrometer. The probe is situated perpendicular to B_0. Electrons can be collected on the copper wire and show up as negative current only if their gyro-radii are larger than the threshold value

$$r = [d^2 + (L/2)^2]/2d\,, \tag{2.1}$$

Where d is the ceramic tube inner diameter (0.2 mm) and L is the copper wire recessing distance (Fig 2.8).

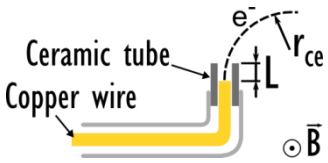

Fig 2.8: Schematics of a "soda-straw probe".

In principle, the electron perpendicular velocity distribution function $f(v_{e\perp})$ can be extracted by probe current measurement at various wire recess distance $I(L)$. The two functions are related by an integral transform

$$\int_0^\infty f(v_{e\perp})\, p(v_{e\perp}, L)\, dv_{e\perp} = I(L) \tag{2.2}$$

, where the kernel $p(v_{e\perp}, L)$ is the probe response of a mono-energetic electron population at certain wire recess distance. Given the measurement $I(L)$, Eq (2.2) can be solved numerically for $f(v_{e\perp})$. However, due to infinitesimal values of $p(v_{e\perp}, L)$ near the threshold velocity, the solution is very sensitive to noise in the measurement. Therefore, the electron distribution function was not extracted from the probe measurement.

Fig 2.9 is a schematic of the probe construction. A 120 μm diameter copper wire is threaded into a 200 μm i.d. (inner diameter) 5 mm long ceramic tube, then run through another 690 μm o.d. (outer diameter) 10 cm long single bore ceramic rod. A 2 mm o.d. glass tube is bended to a smoothly curved 90 degree angle. The thinner ceramic tube blocks the low energy electrons, and is attached to one end of the glass tube by epoxy. The probe is designed such that the thin copper wire is retractable relative to the thin ceramic tube with great precision while the probe is in vacuum. This is achieved by mechanically attaching the copper wire to the ceramic rod, which is attached on the other end to a 5 mm diameter copper rod running the whole length of the probe shaft, through a vacuum feed through, to a micrometer that moves them together with 1 μm precision. Electrically, the copper wire is attached to the center conductor of a coaxial cable which runs the full length of the probe shaft. The probe signal is finally brought out by a vacuum save LEMO connector.

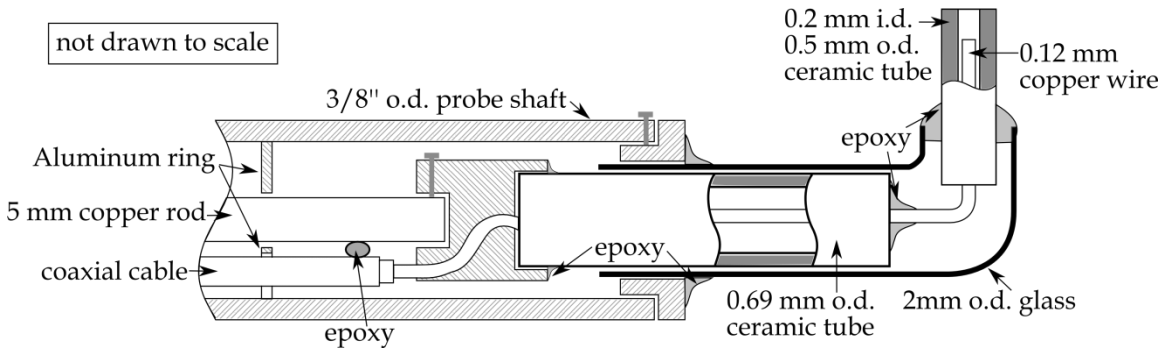

Fig 2.9: Cross-sectional drawing of a "soda-straw probe".

2.4.4 X-ray scintillation detector

Scintillation detector is a common method for x-ray detection and spectroscopy. The scintillator crystal in the detector absorbs energy in an incident x-ray by photoelectric effect, Compton scattering or electron-positron pair production (cross-sections of these processes as function of incident x-ray energy are shown in Fig 2.10), and subsequently excite the crystal atoms and molecules. Scintillation photons are emitted with the de-excitation process, and are converted to an electric signal by a photomultiplier tube. It is generally assumed that the total charge in the output electric pulse is proportional to the energy of the incident x-ray.

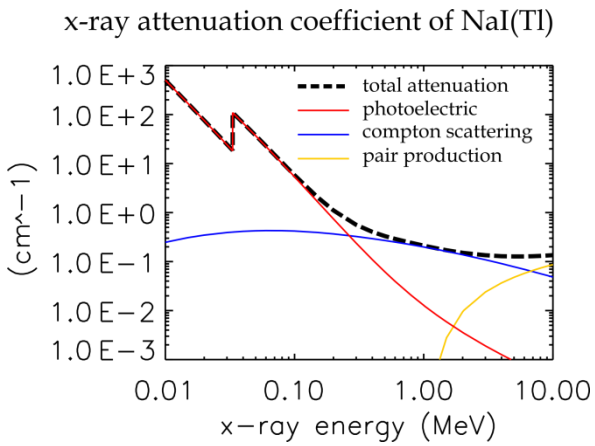

Fig 2.10: Probability of interactions between x-ray and NaI(Tl) crystal in terms of attenuation coefficient μ that characterize the exponential decay of the intensity of x-rays when travel through matter by $I = I_0 e^{-\mu l}$, where I and I_0 are the intensity of a monoenergetic beam of x-rays after and before it travels in the matter for a distance of l. Data for the graph is retrieved from National Institute of Standards and Technology (NIST) and calculated with a density of 3.67 g/cm^3 of the NaI(Tl) crystal.

This experiment used an integrated scintillation detector, which contained a 7.62 cm diameter × 7.62 cm long cylindrical thallium-doped sodium iodide (or NaI(Tl)) crystal, a photomultiplier tube (PMT) directly optically coupled to the crystal, and a layer of mu-metal to magnetically shield the PMT. As a test the detector was placed in a 1000 Gauss ambient field at arbitrary directions, and no effect was found in the detector output; this field is substantially larger than that the detector is located in the experiment. The detector was calibrated with the 661.7 keV x-rays from Cs-137 using pulse height analysis. The hard x-rays produced in this experiment were energetic enough (>100keV) to penetrate the 3/8 inch thick stainless steel wall of the

vacuum chamber. Therefore the detector is conveniently located outside the vacuum chamber. The x-ray transmission rate of vacuum chamber wall is shown in Fig 2.11.

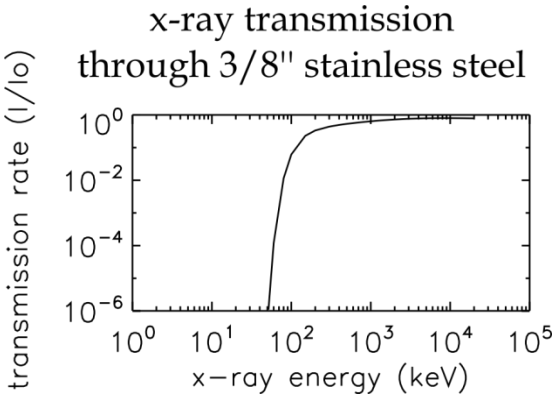

Fig 2.11: Transmission rate I/I_0 of a monoenergetic x-ray beam traveling through 3/8 inch stainless steel, where I_0 is the incident beam intensity and I is the exit intensity.

2.4.5 X-ray computed tomography

Computed tomography (CT) is a technique to produce cross-sectional image of an object by measuring propagation of collimated beams through the object (or other forms of line integrals through the object). At present the most common application of CT is in medical imaging [Hsieh 2009], while it has been successfully applied to high temperature plasma diagnostics [Camacho 1986] [Edwards 1986] [Nagayama 1987] [Janicki 1989] [Anton 1996]. In this experiment, we assume x-rays are emitted isotropically, and measure line integrated x-ray emissivity using a collimated x-ray detector to calculate the 2D emissivity profile.

To get a line of sight integrated measurement of the x-rays, the scintillation detector is encased in lead shielding with an opening for a collimator. The thinnest part of the lead is 5.8 cm, which passes less than 6% of x-rays with energy in the range 100 keV to 3 MeV. The lead was cast into an iron tube, which also provided additional magnetic shielding for the PMT. The collimator was made of lead with a 10.2 cm long cylindrical tunnel in the center. The inner part of the collimator was replaceable to change the acceptance angle in different experimental conditions. Three replacement collimators were made, with hole-diameters of 12.7 mm, 6.4 mm and 3.2 mm.

A large set of sightline integrated measurements is required in order to calculate a tomogram. Since the experiment is highly reproducible and is repeated once every second, all line projections are measured by only one movable detector with a computer controlled rotation drive (Fig 2.12). The rotation drive is mounted on a horizontal platform which can move vertically with 1 mm precision and was able to hold the 300 lb weight of the drive and the detector shielding mounted on it.

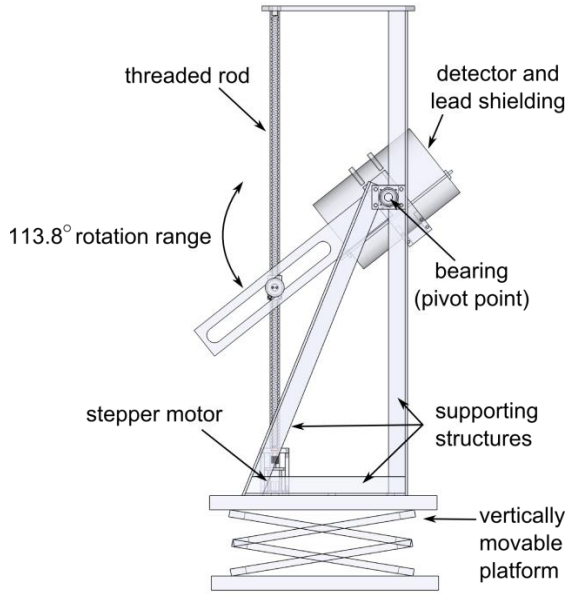

Fig 2.12: A drawing of the rotation drive with the detector shielding mounted on it.

We parameterize each line projection on a transverse plane by (t,θ), where t is the impact parameter of the chord offset from the vacuum chamber center, and θ is the angle from the x-axis (Fig 2.13a). According to Fourier slice theorem[1], the 2D x-ray emissivity can be fully reconstructed from the line projection data if the full (t,θ) space is sampled. In this experiment, the tomography system is designed to maximize the (t,θ) space coverage. These two parameters are limited by several factors: (i) all parts of the rotation drive needs to be clear from the LaPD magnets and its supporting structures; (ii) the platform have a limited range of vertical motion; and (iii) the rotation drive have a limited range of angular motion. The achievable (t,θ) is plotted in Fig 2.13 (b). The x-ray emissivity is confined inside the vacuum chamber, which has

[1] The theorem states that, *the Fourier transform of a parallel projection of a 2D function f(x, y) obtained at angle θ equals a line in a 2D Fourier transform of f(x, y) taken at the same angle [Hsieh 2009]*.

a radius of 50 cm, therefore only the region with $|t| \le 50cm$ is considered. A novel Dot-by-Dot Reconstruction (DDR) algorithm was developed to calculate tomograms with limited measurements, which was found to be more effective than previously published methods for the specific geometry of this experiment. A detailed description of the DDR algrithem is included in appendix A for reference.

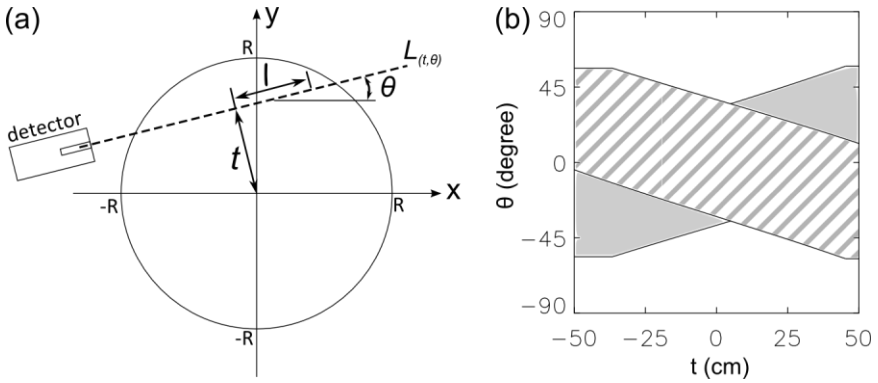

Fig 2.13: A drawing of the experiment geometry on the transverse x-y plane. The sign of t is defined as the sign of the y-intercept. (b) A map of (t,θ) coverage by the tomography system. The hatched area can be covered with the detector moving only on the positive x side of the vacuum chamber. The uniformly shaded area is added if the detector is moved to the negative x side of the vacuum chamber.

2.5 Summary of experiment setup

This dissertation consists of two series of experiments, characterized by the different energy level of the targeting electrons to be de-trapped (at ~100 eV and ~100 keV respectively). Because of their vastly different energy levels, the experimental method for generation and detection of these trapped electrons

are different. We have found it is technically difficult to study both energy ranges in one experiment. For example, a probe that detects 100 eV electrons will interfere with the generation of 100 keV electrons, and the probe itself will be destroyed with the high power microwave heating required to generate the higher energy electrons. Therefore, the two energy ranges are studied separately.

The two series of experiments have similar settings, shown schematically in Fig 2.14. A magnetic mirror field is established near the center of LaPD. High power microwaves are introduced into the LaPD chamber radially to generate a fast electron population, which is trapped by the magnetic mirror. A shear Alfvén wave is launched separately using the RMF antenna which is placed outside the mirror. Probes are inserted radially at different axial positions to diagnose the experiment. In the Cartesian coordinate system used this dissertation, the microwave waveguide is located at z = 0, and on the machine axis (x,y)=(0,0). $\hat{z}$ direction points towards the cathode, and $\hat{y}$ points vertically up. The axial magnetic field profiles for the two series of experiments, as well as the positions for the microwave waveguide and the RMF antenna, are shown in Fig 2.15.

The timing system used in this dissertation defines t = 0 as the start of microwave heating. The experiments are conducted in the LaPD afterglow plasma. Typical parameters used for the two series of experiments are listed in Table 2.2.

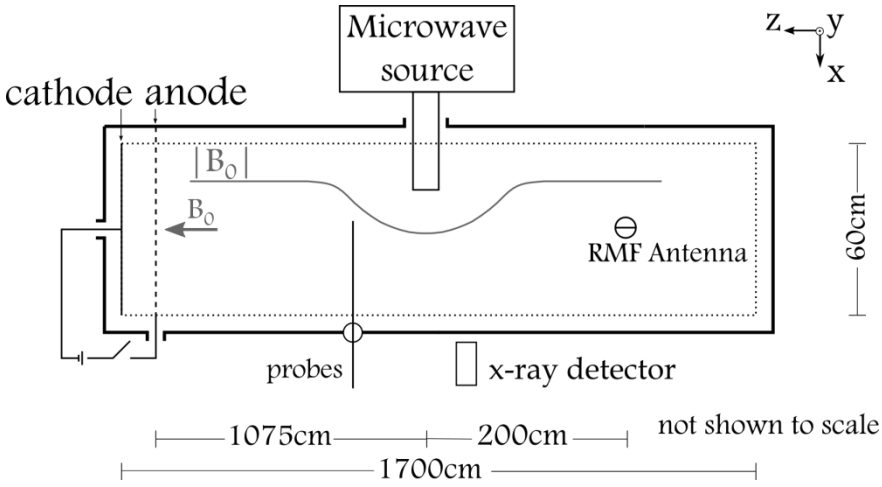

Fig 2.14: Schematic of the experiment. The two series of experiments have very similar setup.

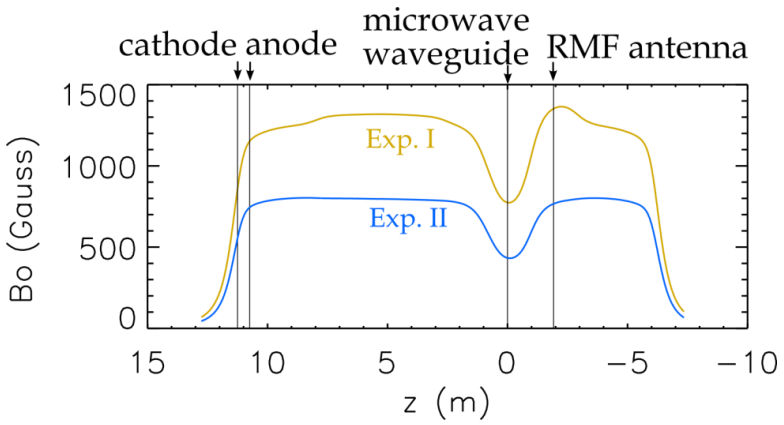

Fig 2.15: Axial magnetic field profile in the two series of experiments. Z coordinates of the cathode-anode pair, the microwave waveguide and the RMF antenna are marked. The second experiment is conducted at a lower field because the generation of the highly energetic electrons is found to be more efficient at the second harmonic electron cyclotron resonance (ECR) frequency ($f_{microwaves} = 2 f_{ce}$) compared to at the fundamental ECR frequency ($f_{microwaves} = f_{ce}$) or the upper-hybrid resonance frequency ($f_{microwaves} = f_{UH}$).

	Experiment I	Experiment II
Fast electron energy	~10^2 eV	~10^5 eV
Microwave heating peak power	5 kW	10 kW
Microwave heating duration	0.1 ~ 3 ms	10 ~ 100 ms
B_{min}	800 Gauss	438 Gauss
Mirror ratio (B_{max}/B_{min})	1.6	1.8
Mirror length (between B=0.95 B_{max})	3.52 m	3.56 m
Alfvén wave frequency	220 kHz	115 kHz
f_{Alfven} / f_{ci}	0.45 ~ 0.72	0.38 ~ 0.69
$\lambda_{\parallel, Alfven}$	7.9 m	9.6 m
B_{Alfven} / B_0	0.11%	0.06%

Table 2.2: Typical parameters in the two series of experiments.

CHAPTER 3

Experiment I: De-trapping electrons at the 100 eV energy level

This experiment was conducted in the earlier stage of this study prior to a microwave source upgrade. The fast electrons with energies of ~100 eV are generated by microwave heating at a low power (peak power 3 kW typical) and with a short heating time (3 ms typical). The diagnostics for these electrons include Langmuir probes, the "soda-straw" probe and visible light emission. Decreases in the fast electron signal on all of these diagnostics are observed when a shear Alfvén wave passes through the electrons, indicating the shear Alfvén wave causes electron loss from the mirror region.

3.1 Fast electron generation

We begin with two photographs taken with a camera from the end of the LaPD chamber (Fig 3.1). The dark cross in the center is the RMF antenna. The microwave waveguide (with ring magnets attached at the end) is at the right hand side in the pictures. The two pictures are taken without microwaves (a) and with microwaves (b). The camera is triggered at the same delay time in the plasma afterglow, when the cathode-anode discharge voltage has been switched off and the plasma density and temperature start to decay.

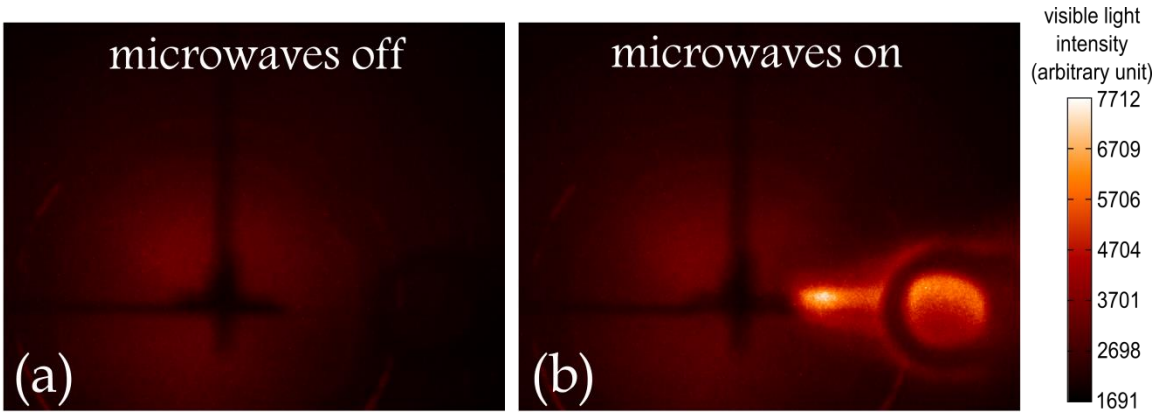

Fig 3.1: Photographs taken by a camera with 1 us exposure time, aiming along B_0, (a) without microwaves and (b) with microwaves. Plasma near the waveguide is illuminated by the microwaves. The light is generated by fast electrons. The background plasma is Helium.

The photographs can be approximated by[1]

$$I = \int_L d\vec{r} \int dE \sum_i \sigma_i(E)\, p_i\, f_e(E, \vec{r})\, n_n \tag{3.1}$$

Where I is the light intensity of a pixel and L is the line of sight corresponding to that pixel; the integrating variables $\vec{r}$ and E are spatial location and incident electron energy; p_i is the probability of an optical transition from the ith energy level to a lower energy level and can be treated as a constant here; n_n is the density of ground state atoms and can also be considered as a constant. We focus on the energy related parts in (3.1): f_e is the electron distribution function, and σ_i is the excitation cross section of the ith energy level of an atom. For Helium, $\sigma_i(E)$ typically peaks at around 100 eV. A curve of the excitation

[1] Further details such as helium ion lines, quantum efficiency of emission, plasma optical depth and the detector response are omitted here.

cross section from the ground state to the lowest excited state is shown in Fig 3.2.

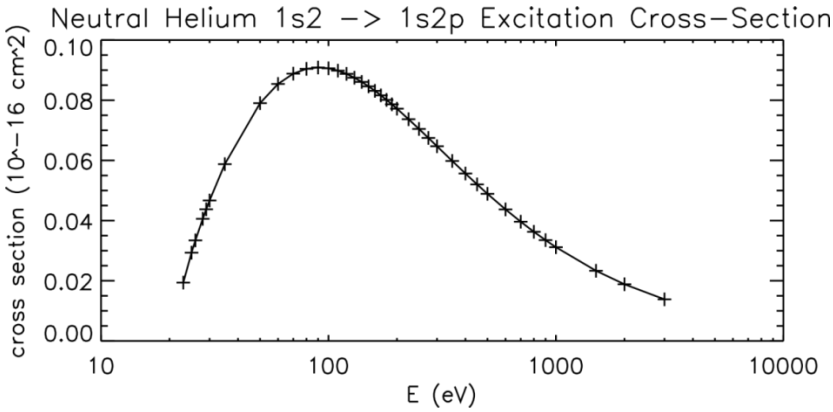

Fig 3.2 Electron impact excitation cross-section for Helium atom, from ground state ($1s^2$) to the lowest excited state (1s1p). Data retrieved from National Institute of Standards and Technology (NIST).

The difference in Fig 3.1 (a) and (b) can be explained as a change in plasma energy distribution function. For the afterglow plasma, f_e peaks around 0.5 eV and decays rapidly beyond the peak, therefore little light is emitted (Fig 3.1a). With the microwave heating (Fig 3.1b), a population of electrons is heated to a significantly higher energy (> 20 eV) so that the helium neutrals start to emit light. The generation of the fast electrons is further confirmed by measurement of the plasma UV spectrum, which shows strong enhancement of the lines in the Extreme Ultraviolet (EUV) range when the microwaves are turned on, such as the He II 303.8 Å line which requires an excitation energy of 40.8 eV.

In Fig 3.1 the photograph shows the integrated light along the camera's line of sight. The bright spot in Fig 3.1 (b) may correspond to the light emission from the end of the magnetic mirror. A localized probe measurement was used to clarify the ambiguity of the fast electron spatial distribution.

The fast electrons are detected by a Langmuir probe. The probe is biased at -70 V relative to the vacuum chamber. In absence of the fast electrons, the bias voltage repels the cold electrons in the background plasma and collects positive ion saturation current. Fast electrons with energies higher than the bias can overcome the potential barrier and get collected by the probe. Therefore in presence of the fast electrons, the positive probe current decreases or even becomes negative. Fig 3.3 shows the probe current measured on a small data plane in front of the microwave waveguide between the two rings attached at the end (geometry is shown in upper right in the figure).

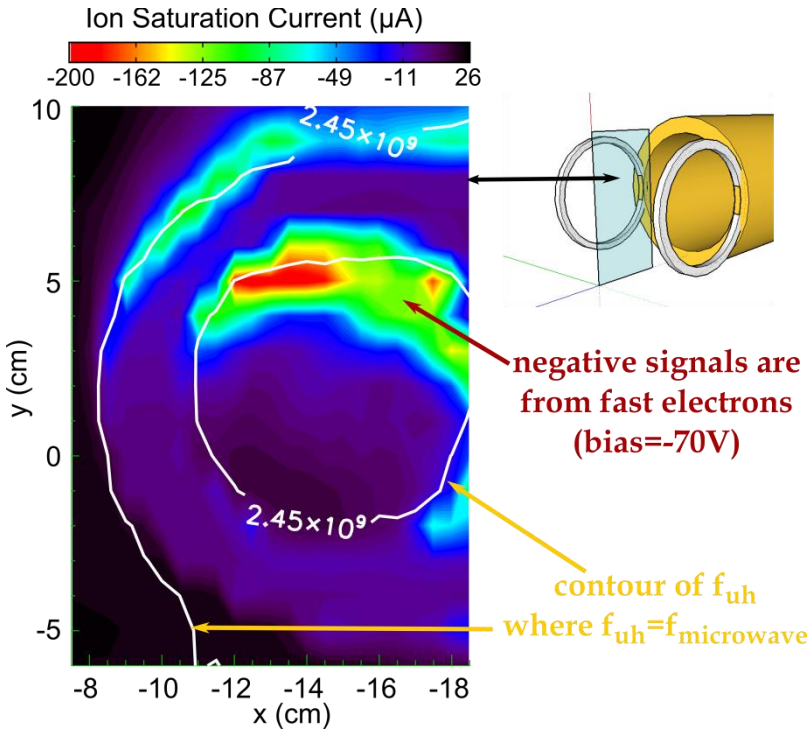

Fig 3.3 (left) Ion saturation current measured by a Langmuir probe moving on a small data plane in front of the waveguide. (upper right) geometry showing where the measurement is located. The probe is biased at -70 Volts relative to the vacuum chamber. Fast electrons with energy higher than the bias can be collected by the probe and show up as negative signals. Two contours where the plasma density and local magnetic field result in the upper hybrid frequency matching the microwave frequency are superimposed.

The spatial distribution of the fast electrons shown in Fig 3.3 suggests the heating is most efficient at the upper-hybrid frequency. The upper-hybrid frequency is given by

$$f_{uh} = (f_{ce}^2 + f_{pe}^2)^{1/2} \tag{3.2}$$

, and is related to both local plasma density and magnetic field intensity via fpe (electron plasma frequency) and fce (electron cyclotron frequency). We estimate the plasma density with Langmuir probe measurement just before the microwaves are turned on (0.25 ms prior to the time step when measurement in Fig 3.3 is made. The plasma density is approximately constant during this short period). The magnetic field is calculated from the currents in the LaPD magnets. The upper hybrid frequency is then evaluated for every point on the data plane, and the contours where f_{uh} matches $f_{microwave}$ are over-plotted on the probe current plot. It is apparent that the fast electrons are generated along these contours.

This heating frequency preference can be understood by examining the microwave propagation. In the waveguide the microwave wavelength is 14.8

cm. The heating microwaves leave the waveguide and immediately enter plasma as an electro-magnetic wave propagating perpendicular to the B_0 ($k \perp B_0$) with its electric field also perpendicular to B_0. It is an extraordinary wave (or X wave). The dispersion relation of an X wave (in cold plasma approximation) is given by

$$\frac{c^2k^2}{\omega^2} = 1 - \frac{\omega_{pe}^2}{\omega^2}\frac{\omega^2 - \omega_{pe}^2}{\omega^2 - \omega_{uh}^2}, \tag{3.3}$$

where ω, ω_{pe} and ω_{uh} are the X wave frequency (which is the microwave frequency here), electron plasma frequency and the upper hybrid frequency, and k is the wave number. At $\omega = \omega_{uh}$, the wavelength becomes zero (the wave reaches resonance), thus the microwaves power is strongly absorbed by the plasma and turns into mostly kinetic energy of the electrons.

3. 2 Fast electron de-trapping

Fig 3.4(c) shows the hot electron current collected by a Langmuir probe biased at -70 V relative to vacuum chamber (normally at this bias potential the probe draws a positive ion saturation current in the background plasma) when no shear Alfvén wave is launched (blue curve) compared with the case when the wave is launched at t = 0.5 ms for a duration of 0.2 ms (black curve). Microwave heating is turned on for both cases at t=0, and lasts for about 2 ms as shown in Fig 3.4(a).

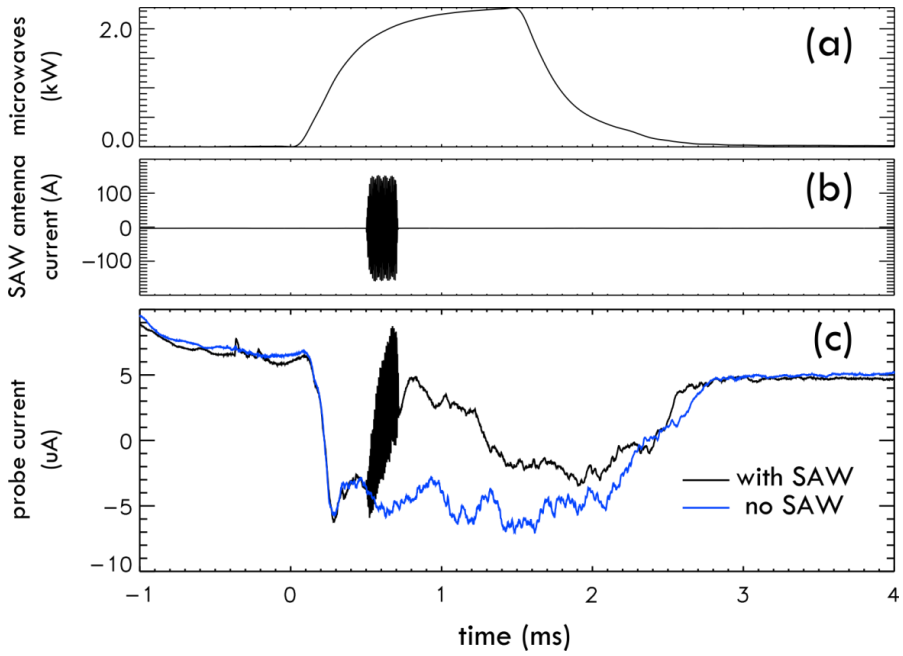

Fig 3.4: Comparison of I_{sat} measured with/without the presence of a shear Alfvén wave. Both cases have same microwave heating power shown in panel (a). In one case the shear Alfvén wave is launched during t = [0.5, 0.7] ms, as shown in panel (b), while in the other case no wave is launched. The hot electron current measured by a Langmuir probe in both cases are shown in panel (c).

Before the microwaves are turned on, in both cases the probe collects a positive ion current (the slow decay is caused by plasma production shutting off at t = -1.5 ms). Later when the microwaves are switched on, the probe current drops to negative level indicating the presence of the fast electrons, and the two cases agree before t = 0.5 ms. In the presence of a shear Alfvén wave (black curve) the negative fast electron current disappears. The fast electron signal comes back slowly after the wave shuts off due to the continuing microwave heating, while in the no Alfvén wave case the signal remains

negative. This comparison shows that the trapped electrons are significantly mitigated by the shear Alfvén wave.

The fast electrons are measured over a small transverse plane using a novel "soda-straw" probe (introduced in Chapter 2, the probe is an improvement over Langmuir probe as it mechanically rejects the background electrons thus increasing sensitivity to the fast electron population). Similar to the setting in Fig 3.4 (a) and (b), an Alfvén wave is launched after the generation of the hot electrons. Fig 3.5 shows the measurement just before and right after the Alfvén wave. The soda-straw probe is recessed to reject electrons of energy less than 80 eV, thus negative probe current indicates presence of the hot electrons. It is worth noting that the shear Alfvén wave is strongest at $(x, y) = (0,0)$ to the left side of the measurement plane, which explains the less effective de-trapping at the right-hand side of the plane.

Visible light from the fast electrons is also reduced by the shear Alfvén wave. The difference in light intensities caused by fast electron de-trapping is brought out by a fast speed camera, shown in Fig 3.6.

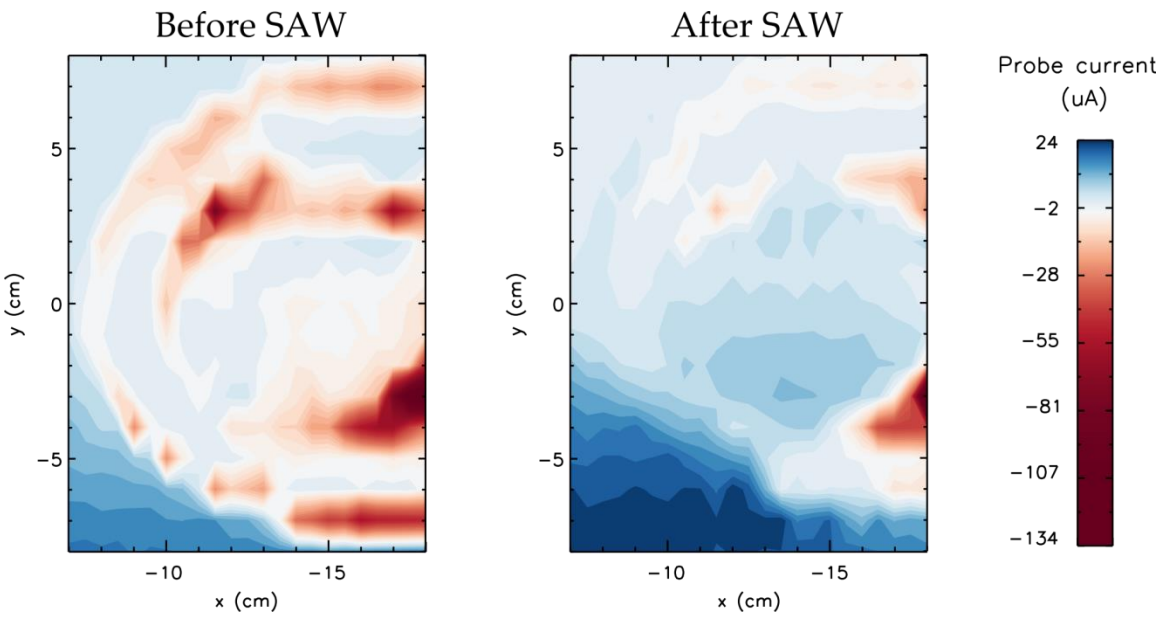

Fig 3.5: Soda-straw probe current measured before/after injection of a shear Alfvén wave. The negative signal (shown in red), indicates fast electrons of energy more than 80 eV, is reduced significantly by the Alfvén wave.

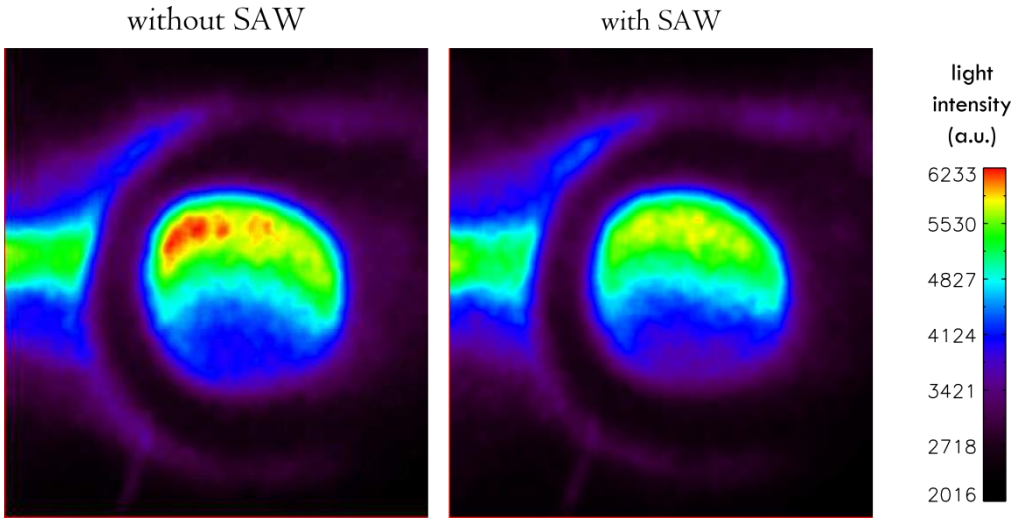

Fig 3.6: Photographs of the light from the fast electrons, taken with/without the presence of a shear Alfvén wave. The bright spot of fast electrons is reduced by the Alfvén wave.

CHAPTER 4

Experiment II: De-trapping 100 keV electrons

4.1 Generation of a magnetic mirror-trapped hot electron ring

In this series of experiments, the background afterglow plasma is heated and a population of trapped fast electrons is generated by microwaves via Electron Cyclotron Resonance Heating (ECRH). At the center of the mirror, high power microwave pulses are introduced radially through a 10 cm diameter cylindrical waveguide. Different magnetic mirror field profiles were tested, and the hot electron generation was found to be most efficient at $f_{microwaves} = 2 f_{ce}$ at the field minimum. The microwaves are pulsed once per second at a peak power of 15 kW, with each pulse starting 2 ms after the LaPD discharge is turned off and lasting 30-50 ms. The starting time of the microwave pulse is defined as t=0. Fig 4.1 summarizes the timing scheme.

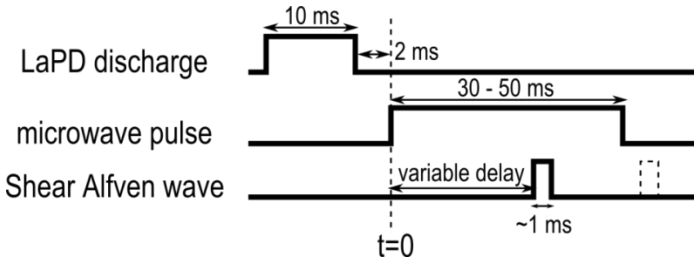

Fig 4.1: Experiment timing scheme.

The microwaves propagate in the $TE_{1,1}$ mode (fundamental Transverse Electric) with $\vec{E}_{microwaves} \parallel \hat{y}$ in the waveguide where the plasma density is

negligible. The microwaves become extraordinary waves (X-mode) as they enter the plasma radially. The cold plasma dispersion approximation predicts that the X-mode wave is evanescent when the plasma density is above a critical density of 1.1×10^{11} cm^{-3} at the fixed background magnetic field of 438 Gauss. In this case the wave field exponentially decays as it propagates into the plasma. The decay length decreases with increasing plasma density. At peak power, the electric field of the microwaves in the waveguide is 3×10^2 V/cm. In the afterglow plasma with a typical density of $n_e = 5 \times 10^{11}$ cm^{-3} the decay length is calculated to be 5.3 cm. It has been observed that the heating is less effective during the LaPD discharge when plasma density is higher.

The presence of the hot electron population is evidenced by detection of hard X-rays. The X-rays are generated when the hot electrons strike metallic surfaces (such as the microwave waveguide or the chamber walls). Due to the imperfect confinement of the magnetic mirror, hot electrons are slowly lost and X-rays continuously generated. The X-rays are detected by a NaI(Tl) scintillator detector located outside the vacuum chamber, with a solid angle span of 0.004±0.002sr measured from the center of the magnetic mirror. The chamber wall is made of 3/8 inch thick stainless steel, which cuts off X-ray transmission below ~100 keV. The X-ray energies are determined to be in the range from 100 keV to 3 MeV using pulse height analysis of the scintillator detector response.

Due to the grad-B and curvature drift, the trapped fast electrons move in the azimuthal direction, which form a hot electron ring within the magnetic mirror. The electrons trapping time (before a loss due to cumulative collisions with Helium atoms or ions) is estimated to be much longer than the period of their grad-B and curvature drift motion ($\tau_{trapping}/\tau_{drift} > 5 \times 10^3$).

The electron azimuthal drift is intuitively visualized in Fig 4.2, which is the ion saturation current measured 96 cm downstream from the magnetic mirror center. It is important to note that what is shown in the figure is not the hot electron ring itself, but a by-product that comes with the generation of the ring. At this axial location, the plasma density and temperature is enhanced by ionization and heating from the anisotropic fast electrons confined near the center of the mirror. As the trapped electrons drift azimuthally, the fast electron density drops along the drift orbit due to collisions with ions and neutrals. It is estimated that for 500 eV electrons that gyrate and drift in the mirror middle plane, the decay length along the drift orbit is about 50 cm. Electrons with higher energies have longer mean free path, but there is not enough density of these electrons at this early time when the measurement is taken (t = 3 ms after ECRH turned on).

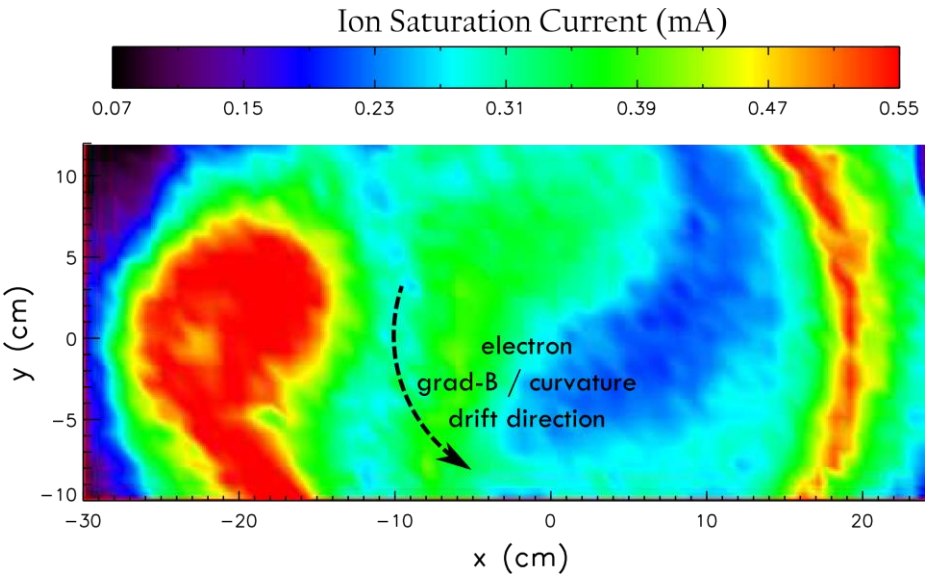

Fig 4.2: Ion saturation current measured 96 cm downstream from the magnetic mirror center. The microwave waveguide comes in from – x axis, and its edge is

at x = -35 cm at the center plane of the mirror (z = 0). The measurement is made at t = 3 ms after ECRH is turned on. It is worth noting that what is shown here is not the hot electron ring itself, but the by-product that comes with the generation of the ring.

The radial thickness of the ring is measured using a "luminator probe" (Fig 4.3a). The probe consists of a 5 mm × 5 mm × 1 mm tungsten tip at the end of a 10 mm diameter ceramic shaft. Fig 4.3(b) is the measured X-ray flux as a function of the probe tip position when the probe is inserted from the positive x-axis. Far away from the ring (probe tip x > 15 cm), the probe has no effect on the X-ray production. A background X-ray flux is measured which is generated by hot electrons slowly lost from the mirror. As the probe is moved further in, copious X-rays are generated when the hot electrons strike the tungsten tip, due to the high atomic number of tungsten. The thin ceramic shaft does not have the same effect. The hot electron ring cannot form when the probe completely cuts through the ring region (probe tip x < 5 cm), therefore no X-ray is measured. The thickness of the ring is measured to be 10 cm.

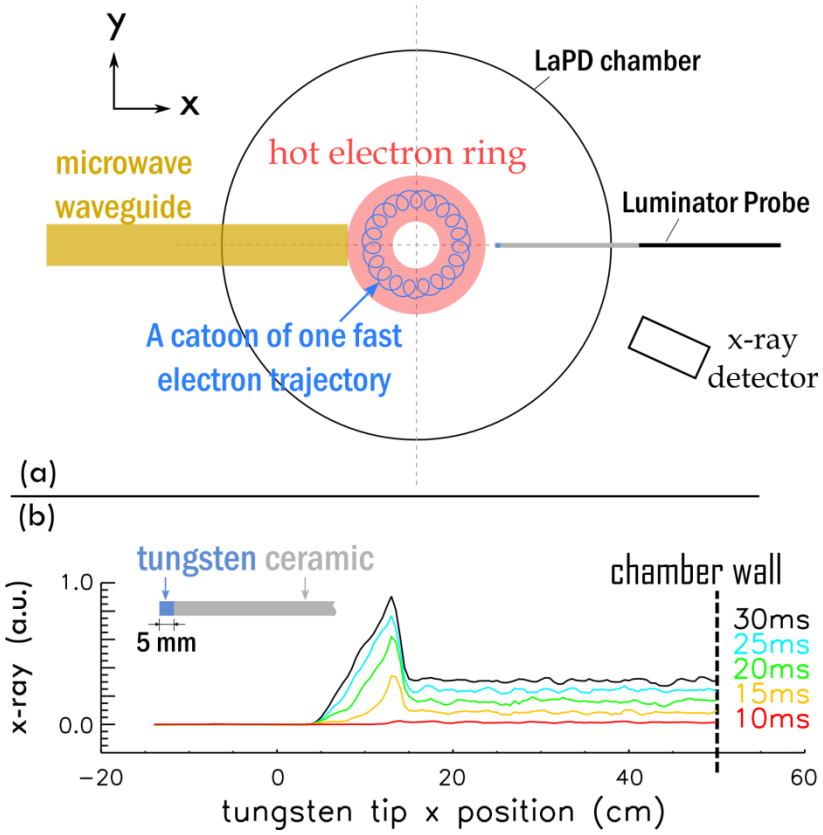

Fig 4.3: (a) A schematic plot of the transverse plane at z = 0, showing the relative position of the vacuum chamber, microwave waveguide, the "luminator probe" and the hot electron ring. (b) X-ray flux as a function of luminator probe tungsten tip position at different times during the ECRH.

With a similar technique, the axial extension of the ring is measured to be Δz = 211 cm by inserting the probe at different axial locations. The axial extension of the ring is a value of interest because it is directly related to the electron anisotropy. For a trapped electron, its pitch angle reaches minimum at the center of the mirror where the field is weakest. This angle θ is related to the furthest distance the electron travels in the axial direction z_{max} by

$$\tan\theta = 1\Big/\sqrt{\frac{B(z_{\max})}{B_{\min}} - 1},$$

where $B_{\min}$ is the minimum magnetic field in the mirror. The calculated lower limit of the pitch-angle distribution of all hot electrons is 56 degrees. The loss cone angle for this magnetic mirror is 47 degrees. The wide margin of the pitch-angle distribution to the loss cone indicates that the anisotropy of the electron velocity is less likely to be shaped by the magnetic confinement, but is dominated by the ECRH which primarily increases the electron's perpendicular energy.

4.2 Hot electron de-trapping

We now examine the de-trapping effect that the shear Alfvén wave has on the ring using hard x-rays as the primary diagnostic. Take Fig 4.4 for example. Fig 4.4 shows the time series of x-ray flux measured after the ECRH is turned on at t=0. The black trace is measured without launching an Alfvén wave. The more or less steady x-ray production is referred to as "the background x-ray production". It is thought that the background x-rays are related to the presence of the microwaves, as evidenced by the fact that their signal drops rapidly with the termination of the ECRH at t = 30 ms.

In this series of experiments, it takes about 20 ms for a measurable background X-ray flux to be generated. We attribute this to the time it takes to accelerate a substantial electron population to energies that produce X-rays measurable outside the vacuum vessel (E >0.1 MeV). Loss of the low-energy electrons is not visible on the existing X-ray diagnostic.

The blue trace in Fig 4.4 is measured with a shear Alfvén wave burst 100 cycles long, f = 115 kHz, launched at t = 23 ms. A burst of x-rays generated by hot electrons escaping the mirror trap and striking metallic surfaces appears during the Alfvén wave propagation time. A large flux of x-ray appears while the Alfvén wave is first turned on. After this initial increase, during the rest of Alfvén wave propagation, the x-ray flux decreases as the hot electron population is depleted. After the Alfvén wave is turned off, the x-ray flux drops precipitously. Later in time (t > 24 ms), the x-ray flux slowly builds up due to the presence of ECRH which is on for an additional 6ms.

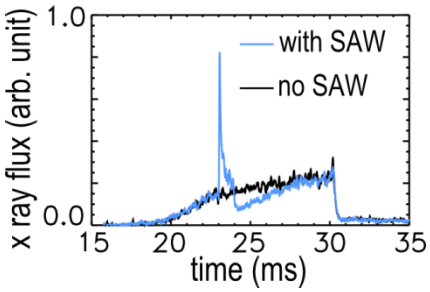

Fig 4.4: Time series of x-ray flux measured with/without the presence of a 100-cycle shear Alfvén wave launched from t = 23 ms to 23.9 ms.

4.2.1 Independence of ECRH and the de-trapping process

Shown in Fig 4.5 is an overlay of 19 traces. For each trace, a 100-cycle Alfvén wave is launched starting at a time between t = 17 ms and t = 40 ms. The starting time of the Alfvén wave for each trace is marked by an arrow with the same color as the trace (designated A-S) on the top. A population of fast electrons persists in the magnetic mirror after the ECRH terminates at t = 30 ms. When the Alfvén wave is switched on at these late times these fast electrons are

lost as evidenced by x-ray bursts in Fig 4.5 traces J-S. The estimated average trapping time for a 200 keV electron is about 40 ms before its loss from the mirror trap as a result of cumulative collisions with helium atoms or ions (see Appendix C). We observe hot electrons by Alfvén wave scattering during the same time scale (up to 10 ms). The decay of the X-ray burst intensity after t = 31 ms reflects the decay of the number of X-ray producing hot electrons still in the mirror. There is also a possible factor of decreasing Alfvén wave amplitude due to the plasma density decay after the ECRH is switched off, which increases the Alfvén wavelength from 8 m to lengths that no longer fit into the 18 m long plasma column. This measurement proves that the electron loss due to the shear Alfvén wave is not related to the presence of the microwaves.

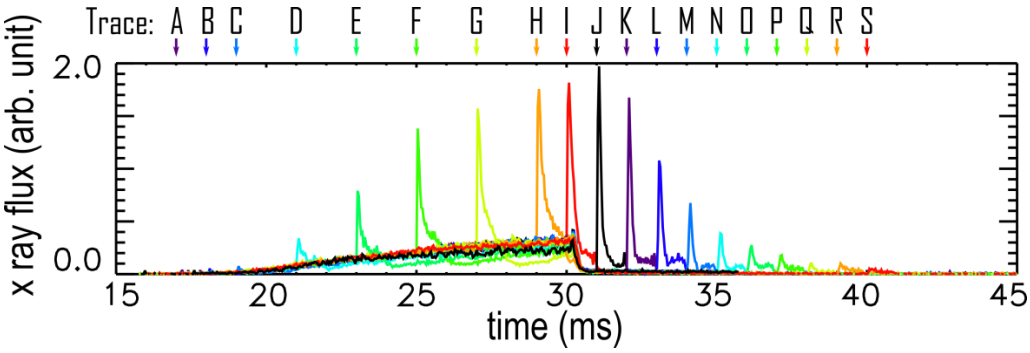

Fig 4.5: Overlay of 19 traces of x-ray flux measured with an un-collimated detector (designated A-S), each with a 100-cycle SAW launched at different time delays (marked by an arrow on the top).

4.2.2 Modulated electron loss

The temporal history of the x-ray burst, created by the Alfvén wave de-trapped fast electrons, shows a modulation at the SAW frequency. The x-ray signal, averaged over a large ensemble (1200 shots), is shown in Fig 4.6 with

comparison of B_x of the Alfvén wave measured at the center of the magnetic mirror.

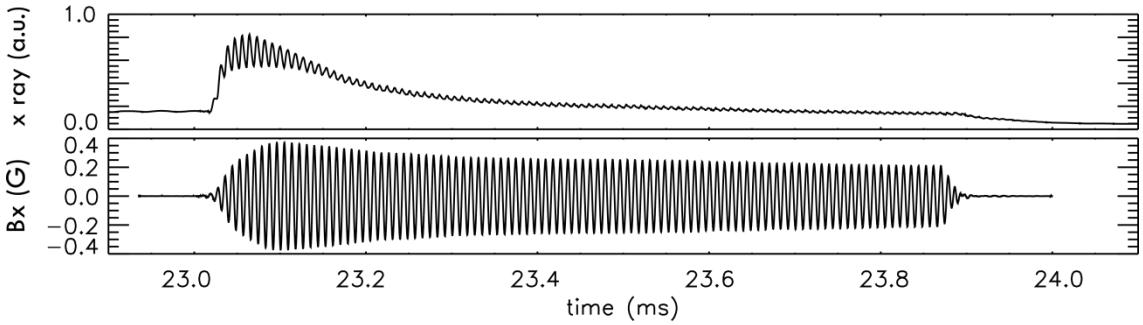

Fig 4.6: 1200 shot averaged signal of the x-ray burst during SAW propagation. B_x of the SAW measured at the center of the magnetic mirror in absence of the ECRH is shown on the bottom trace.

4.2.3 Alfvén ghost

The loss of the fast electrons is observed to continue even after the termination of the Alfvén wave. The hot electron loss is still modulated, at the same frequency that the Alfvén wave when it was on. Shown in Fig 4.7 is the measured magnetic field of the wave (z = 191.7 cm). After the driver is shut off, magnetic fluctuations are observed for an additional 4-5 wave cycles, which appear to become incoherent (frequency is decreased and phase is shifted) as shown magnified in Fig 4.7. About eight SAW periods after the wave driver is turned off, the amplitude of magnetic fluctuation drops to a negligible level (below 0.1 mG). Even so the hot electrons continue to be lost form the magnetic mirror periodically at the SAW frequency. The x-ray oscillations are observed to last more than 50 cycles coherently after the wave is terminated. It is likely that the Alfvén wave has left an imprint on the trapped hot electron distribution

function that is not damped and de-traps the hot electrons, if you like, in its afterlife.

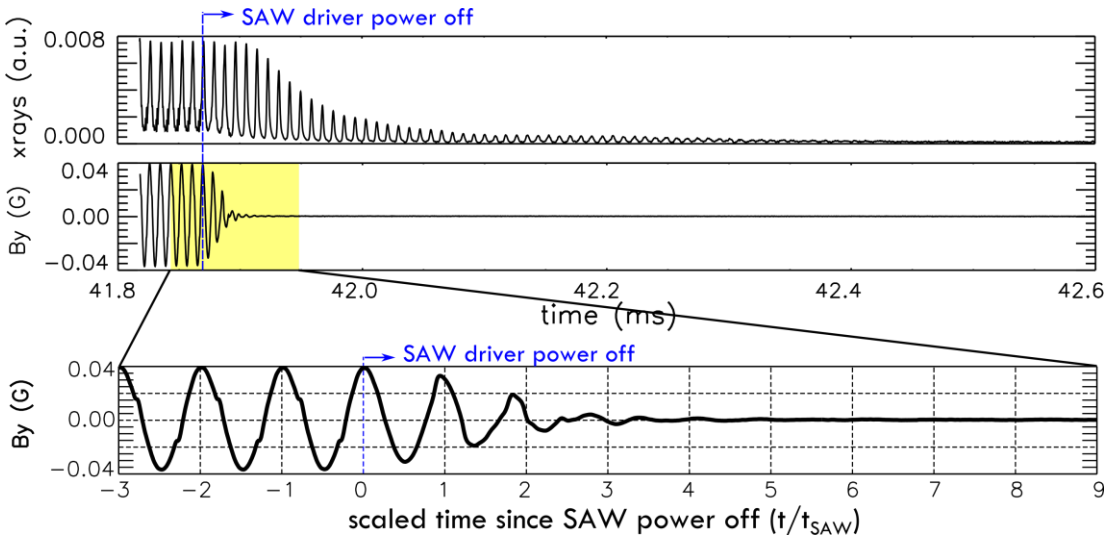

Fig 4.7: X-ray flux (un-collimated) and B_y of the Alfvén wave on the machine axis outside the mirror, measured just after the Alfvén wave driver power off.

4.2.4 Spatial distribution of the lost electrons

Because the x-rays are traces of energetic electrons striking a metallic surface, the x-ray emissivity profile can reveal the spatial distribution of the released hot electrons. Hard x-ray computed tomography (CT), which is a non-invasive diagnostics to measure spatial profile of x-ray emissivity, is performed with a tomography system described in Sec 2.4. The tomograms are rendered using a reconstruction algorithm called DDR described in Appendix A.

Fig 4.8 shows x-ray tomograms at the center of the mirror. The size and position of the waveguide is shown as semi-transparent red rectangles. In this experimental setting the waveguide is the closest object to the trapped hot electron ring, therefore the lost hot electrons are most likely to hit the

waveguide. As a result, an intense x-ray emissivity is observed in the region where the waveguide locates.

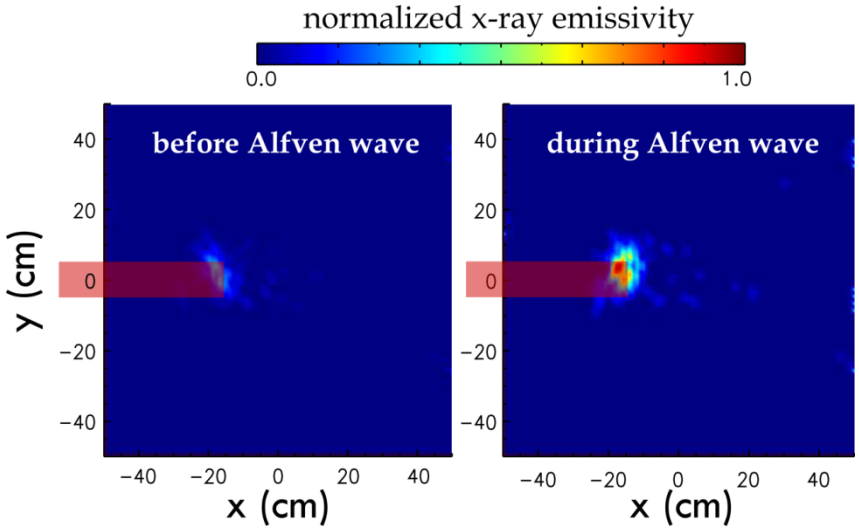

Fig 4.8: X-ray axial tomograms at z = 0. The semi-transparent red rectangles indicating the size and position of the waveguide are superimposed in the plots. The waveguide position is shown as a red rectangle.

X-rays are generated on the LaPD mesh anode located at z = 10.75 m. These x-rays are generated when hot electrons escape the mirror along the machine axis, travel along the magnetic field line and strike the anode. The x-ray counting rate measured on the anode is estimated to be 2% of that measured near the center of the magnetic mirror. The reconstructed emissivity profile on the anode is shown in Fig 4.9. The line cut of the emissivity profile before the Alfvén wave appears to be double peaked at x = ±7 cm. The magnetic field line at this location can be traced back to x = ±9.2 cm in the center of the magnetic mirror. The peak on right-hand side of Fig 4.9 is located at x = -6 cm

which corresponds to x = -7.9 cm in the magnetic mirror and x = -5.9 cm at the RMF antenna.

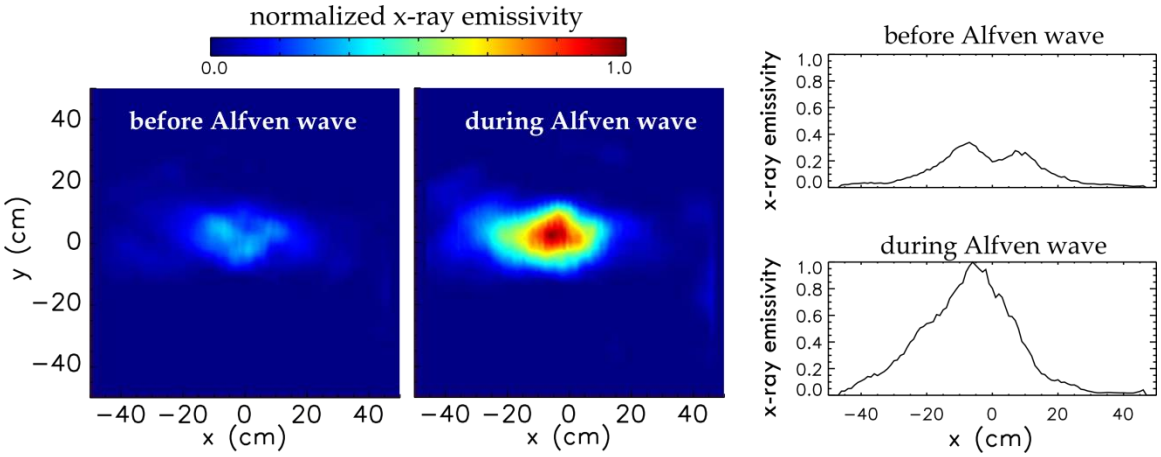

Fig 4.9: (left, colored) X-ray axial tomograms on the plane where the anode was situated (z = 10.75 m). (right) horizontal line cuts at y = 0 of the two tomograms.

At both axial locations (center of mirror and mesh anode), the x-ray flux increases significantly when the shear Alfvén wave is launched. The possibility that the x-rays from the anode may come from a reflection of x-rays at the center of the mirror is ruled out by the highly localized emissivity profile shown in Fig 4.9.

Another interesting observation is that the electron loss in both the axial and radial direction is modulated at $f_{Alfvén}$ with the same phase. As an example, Fig 4.10 compares the time series of the x-rays, generated from the center of the mirror and from a mesh inserted outside the mirror at z = 351.5 cm, which are measured in the same experiment.

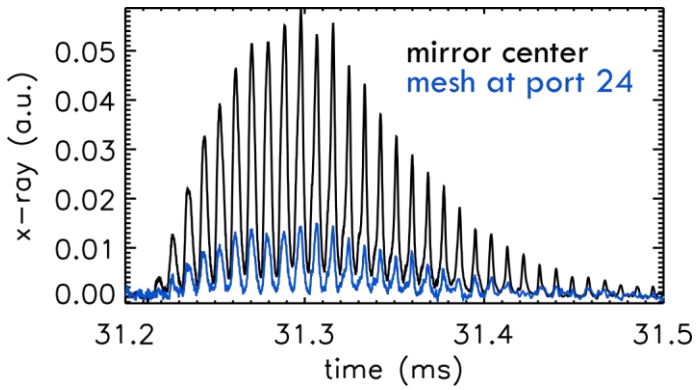

Fig 4.10: Temporal history of x-ray flux. The detector is collimated in such way that only x-rays from near either z = 0 plane (black trace) or z = 351.5 cm plane (blue trace) are recorded. A close up examination of the two traces shows that the oscillations have the same frequency and phase.

4.2.5 Deforming the hot electron ring

The temporal oscillation of the x-rays and its continuation after the termination of the Alfvén wave raises the possibility that the injection of the Alfvén wave generates a collective mode of the ring. In this scenario the collisionless hot electrons interact with each other, likely through a non-local electric field, and oscillate collectively at one frequency. Such a large scale electric field may be directly related to a spatial distortion of the ring, which may come from the non-uniform Alfvén wave field pattern. To study this geometrical asymmetry, a tantalum paddle is inserted to the ring from the side opposite to the waveguide at different distances (Fig 4.11a).

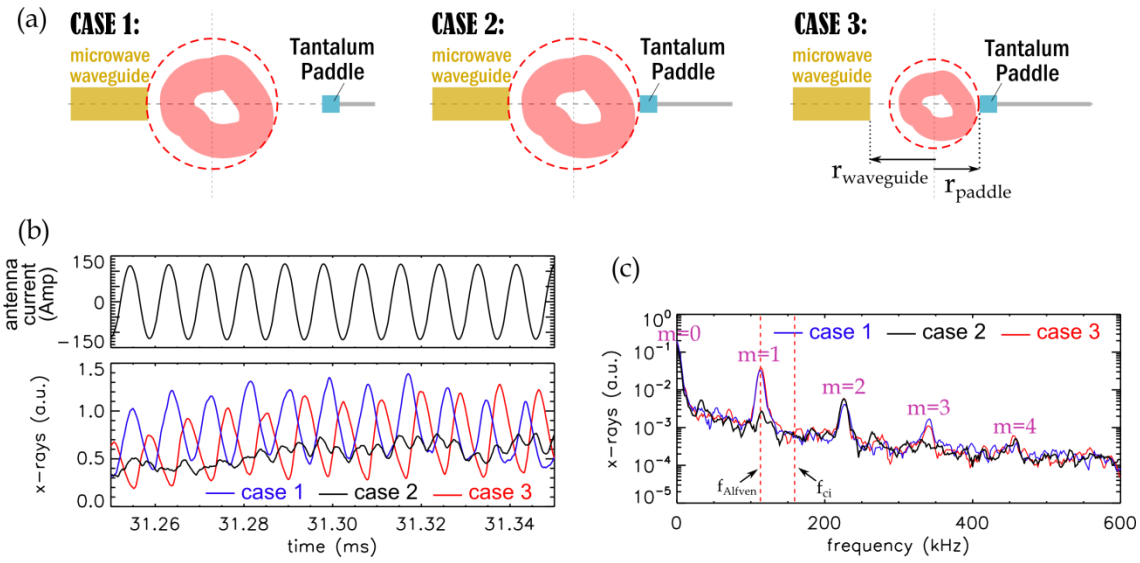

Fig 4.11: (a) Cartoon of experiment setup, for three cases with different positions of a tantalum paddle inserted from the opposite side of the waveguide. (b) X-rays as function of time measured in the three cases. Antenna current is shown on top for comparison. (c) frequency spectrum of the x-ray signal. The dominant oscillation at f = $f_{Alfvén}$ is suppressed by compensating geometrical asymmetry of the experiment.

With the asymmetric setups such as case 1 and 3, as the deformation pattern rotates with the Alfvén wave, electrons are scraped off by the either waveguide or the tantalum paddle in each Alfvén wave period, thus the x-ray signal (Fig 4.11 b, c) have a dominant oscillation at f = $f_{Alfvén}$ (m=1 mode). In these two cases, the phases of the x-ray oscillations are almost reversed. Higher harmonics (m=1 ~ 4) also appears in these two cases. In case 2 the ring is shaved by both the waveguide and the paddle. As the ring is forced to be more symmetric, in the x-ray signal, the dominant m=1 oscillation is suppressed along with m=3 mode, while the m=2,4 oscillation remains. One can imagine

that if we make the system completely cylindrical symmetric, then all modes other than the m = 0 will be suppressed, and the de-trapping of the hot electrons will happen at a nearly uniform rate.

4.2.6 Dependence of de-trapping on the Alfvén wave polarization

It has been observed that the polarization of the shear Alfvén wave plays an important role in this experiment. The Alfvén wave is launched with different polarizations, characterized by the amplitudes of the two circularly polarized components ($|\tilde{B}_{RH}|, |\tilde{B}_{LH}|$) . As an example, hodograms of three different polarities are shown in Fig 4.12. The hot electron ring is created by ECRH from t = 0 to t = 30 ms, and the waves are launched at t = 31 ms for 20 cycles. Fig 4.12 shows the measured x-ray flux generated by Alfvén wave de-trapped hot electrons. The nearly vertical contours indicate the de-trapping is caused by the RH component, while the LH component does not affect the de-trapping.

The x-ray oscillation at the Alfvén wave frequency, such as one shown in Fig4.6, can be approximated by a sine function, thus we can define the phase of the x-ray oscillation its phase. In order to study the relationship between the phase of the x-ray oscillation and that of $\tilde{B}_{RH}$ and $\tilde{B}_{LH}$, we launch shear Alfvén waves composed of RH and LH of the same amplitude but at different phases. Such waves are all linearly polarized but with different polarization angles (3 examples are shown in Fig 4.13). The phase of the x-ray oscillation as a function of the phases of RH and LH is shown in Fig 4.13. Again, the contour is vertical in a LH vs RH plot, which indicates the phase of the x-ray oscillation is locked

to the phase of the RH component, and appears not related to the LH component.

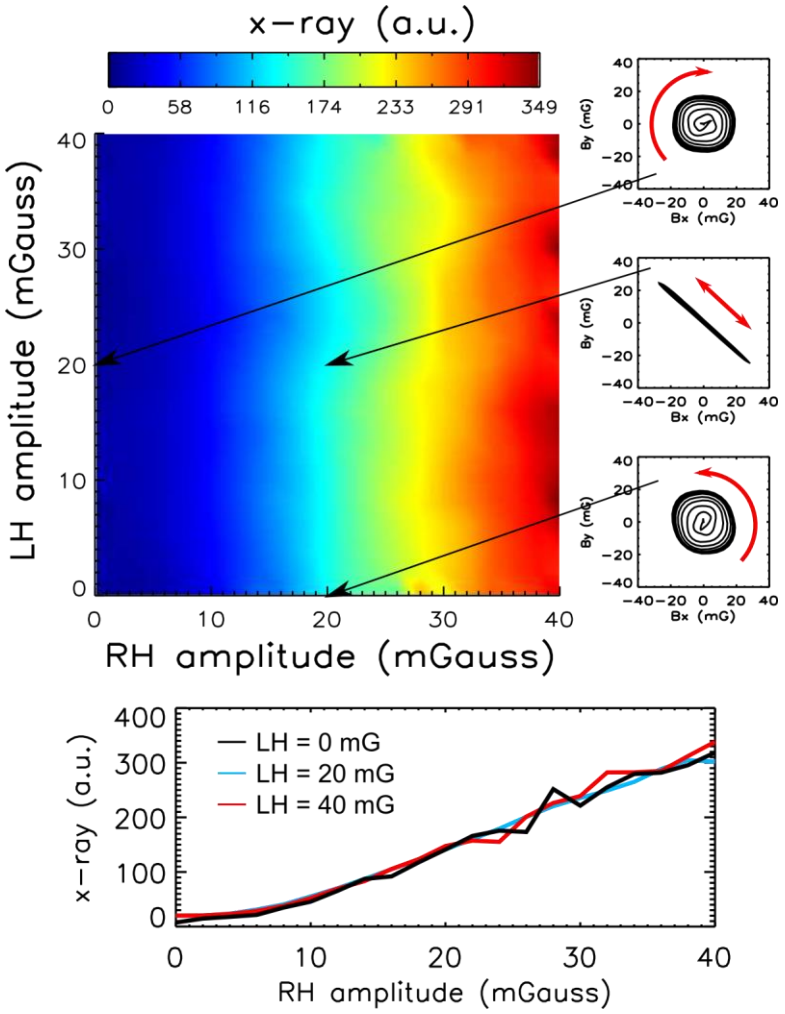

Fig 4.12: (upper-left) The x-ray flux measured when Alfvén waves of different polarizations are launched. (upper-right) Hodograms of Alfvén wave magnetic field with three different polarities. The hodograms begin at the center when the wave is first turned on at t = 31 ms, and end at t = 31.1 ms ($\Delta t = 11\tau_{Alfven}$). The wave magnetic field is measured by a 3-axis B-dot probe on the machine axis at

z = 191.7 cm, by which the polarity of the wave is determined. (bottom) horizontal line-cuts of the upper panel at 3 different LH amplitudes.

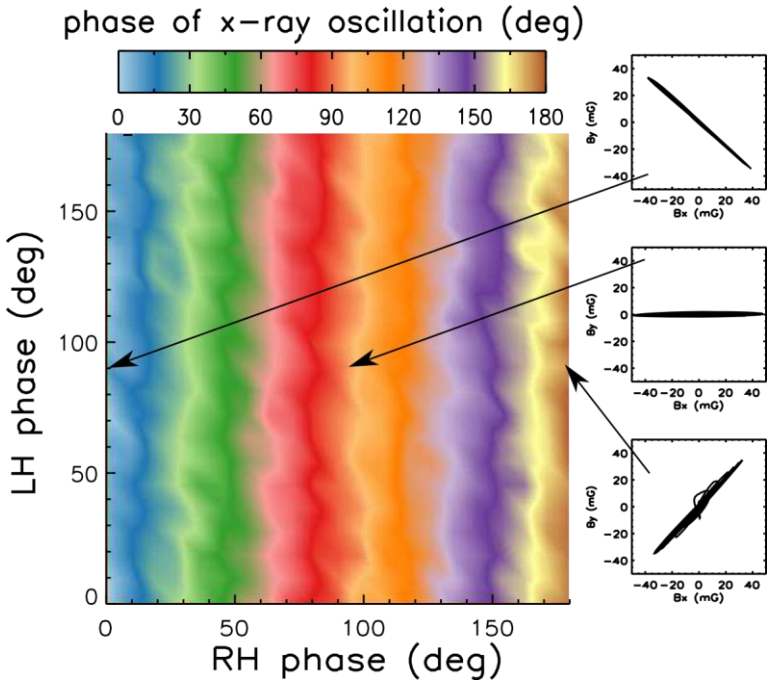

Fig 4.13: (left) Phase of x-ray modulation at $f_{Alfvén}$ as a function of phases of LH and RH component of the Alfvén wave. For ease of comparison, the relative phases are shown with the smallest phases set to 0 deg. (right) Hodograms of Alfvén wave magnetic field with three different phases, measured by a B-dot probe on machine axis at z = 191.7 cm.

4.2.7 X-ray spectrum

The spectrum of the hard x-rays is obtained by pulse-height-analysis from the scintillator detector response, and is calibrated with the 661.7 keV x-ray emission of Cesium-137. Fig 4.14 shows the spectrum of x-rays generated at

the center of the magnetic mirror. Without the presence of Alfvén waves, the hot electrons are slowly lost due to collisions and magnetic field errors. The spectrum overall shows an exponential decay with an e-folding energy of ΔE = 37.4 keV. The deviation from the exponential decay below 100 keV is caused by the low x-ray transmission coefficient of the stainless steel wall of the vacuum vessel. The x-ray counting rate, over the whole energy spectrum, is significantly increased when the Alfvén wave is launched. The x-ray spectrum when the Alfvén is launched still appears to be exponentially decaying with an e-folding energy ΔE = 67.5 keV.

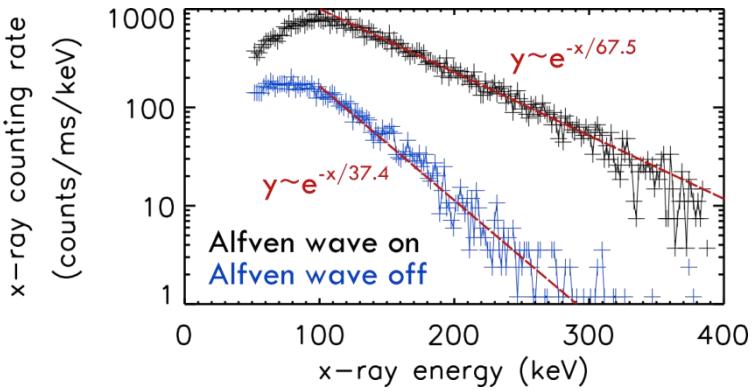

Fig 4.14: X-ray spectrum measured near the center of the magnetic mirror.

The spectrum of the x-rays generated by the axially lost electrons (striking a wire mesh located at z = 351.5 cm) is plotted in Fig 4.15. Similar exponential decay is shown above 100 keV, with ΔE = 41.8 keV (no Alfvén wave) and ΔE = 42.8 keV (with Alfvén wave) respectively. The counting rate is doubled by the Alfvén wave almost uniformly over the whole energy spectrum, which underlines the non-resonant nature of the loss process.

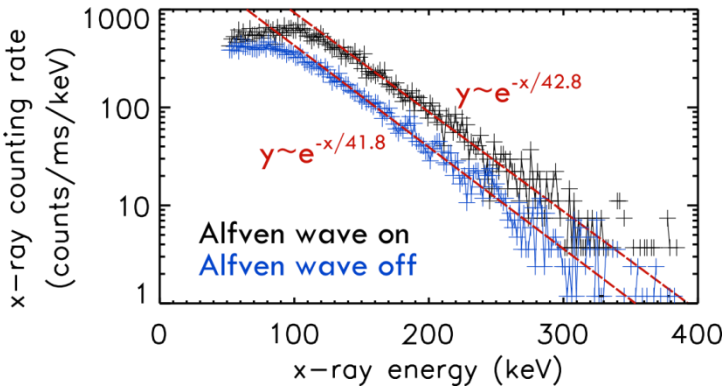

Fig 4.15: X-ray spectrum measured at one end of the magnetic mirror.

4.2.8 Whistler waves and electron de-trapping

The de-trapping process is found to be accompanied by electro-static fluctuations in the frequency range of $1\sim5 f_{lh}$ (the lower hybrid frequency $f_{lh}=(f_{ci}\,f_{ce})^{1/2}$ is about 30 MHz in this case), which are also modulated at the Alfvén wave frequency (Fig 4.16). The electric fluctuation is measured by an electric dipole probe located outside the mirror at z = 1.91 m. They are most likely caused by the high harmonics in the rf current driven in the RMF antenna.

To exclude the possible role of these high frequency fluctuations in the electron de-trapping process, whistler waves at these frequencies are launched with a loop antenna in absence of the Alfvén wave. The electric field amplitudes of the launched whistler waves are at least 10 times higher than that of the high frequency fluctuations accompanied by the electron de-trapping. No significant electron de-trapping is observed when the whistler waves are launched (Fig 4.17).

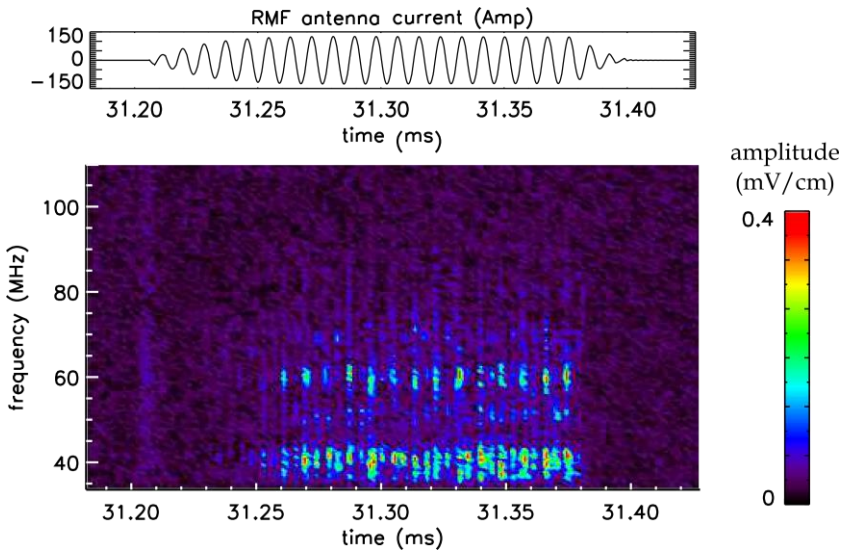

Fig 4.16: (Top) current in the RMF antenna. The launched Alfvén wave has 20 cycles at 115 kHz. (Bottom) High frequency electro-static fluctuations that accompany the electron de-trapping process.

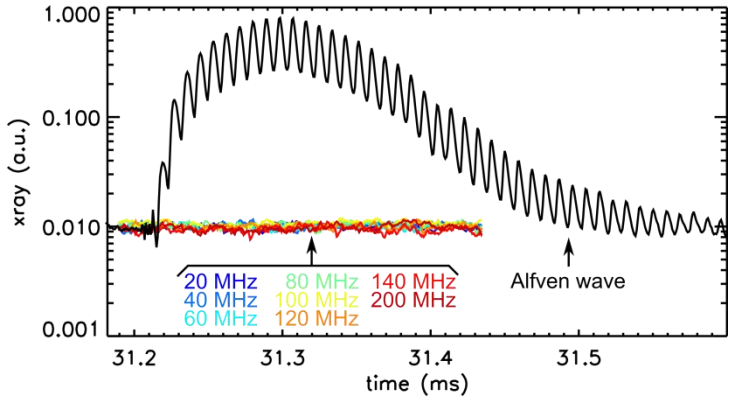

Fig 4.17: X-ray signal measured when Alfvén wave (115 kHz) or whistler waves (20 ~ 200 MHz) are launched. In both cases a hot electron ring is generated by ECRH on from t = [0,30] ms. The Alfvén wave is on from t = [31.2, 31.37] ms. The whistler waves are turned on from t = [31.2, 31.3] ms.

CHAPTER 5

Test particle simulation of single particle evolution

A numerical study is performed to evaluate the effect of the application of an Alfvén wave on the mirror trapped electron population. The highly energetic electrons are nearly collisionless with the background plasma, therefore can be modeled as single particles. The test particle simulation only considers single particle motion, i.e. the electrons are tracked one at a time, and any field caused by them is neglected. The simulation setup is very similar to that in the experiment. From this numerical study, we conclude that changes in the motion of single electrons in the Alfvén wave field are not adequate to explain the experimental observation of electron loss. Therefore collective interactions between the fast electrons must play a role in the electron loss effect.

5.1 Simulation method and setup

The simulation is performed in a domain of $85cm \times 85cm \times 800cm$ volume (longer in the axial direction). The background magnetic mirror field is the same configuration as that in experiment II (Fig 5.3). In consideration of simulation speed and accuracy, the mirror field is calculated from the current setting of the electro-magnets in experiment II on a 101 x 101 x 941 uniform grid in the simulation domain, and values of the background field between grid points are acquired by 3-D interpolation. The variation in B_0 between two adjacent grid points is less than 0.5%.

The Alfvén wave field is calculated by using a Green function solution of the inhomogeneous electromagnetic wave equation with the current source from the RMF antenna. The solution is described in detail in Appendix B. The plasma was modeled using (i) cold plasma approximation; (ii) a kinetic description with a low electron temperature and (iii) a kinetic description of a low temperature plasma with a small population of hot electrons. In the parameter space explored here, except for small quantitative changes, the calculated wave patterns using different plasma models showed no significant difference. Different components of the calculated wave field are shown in Fig 5.1. Similar to the background magnetic field acquisition scheme, the wave field is calculated on a 0.85 cm spacing grid and is interpolated between grid points. A comparison between the calculated $\vec{B}_{Alfven}$ with that measured by a B-dot probe in the experiment is given in Fig 5.2.

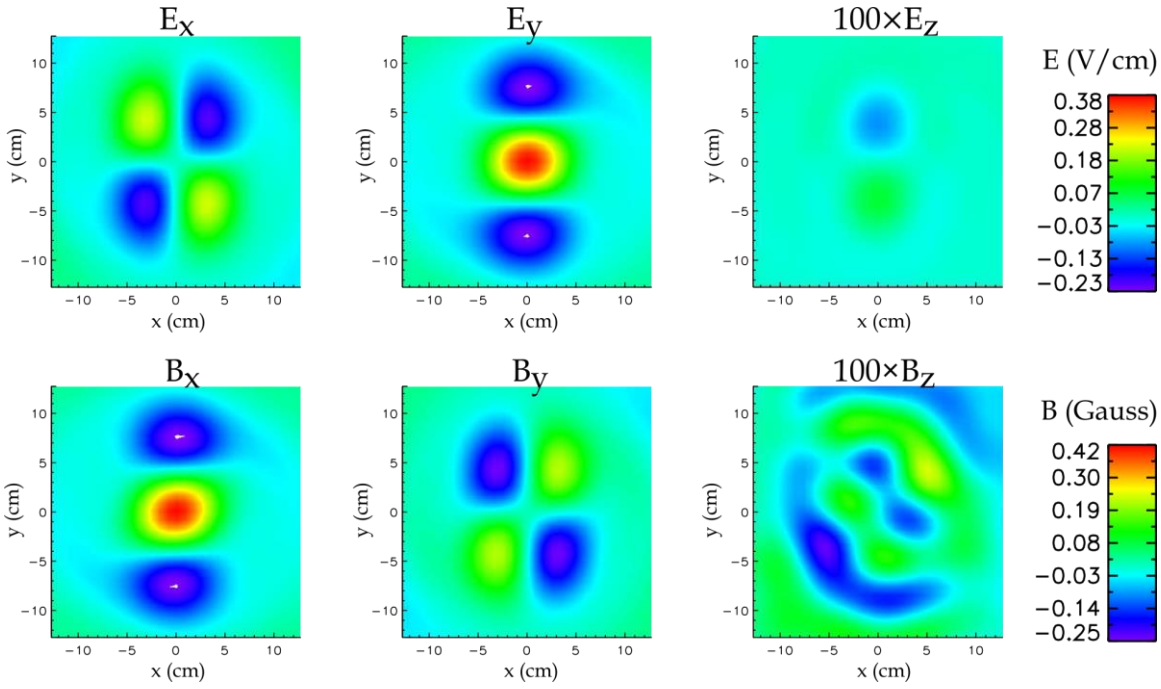

Fig 5.1: Calculated radiation pattern of the RMF antenna on a transverse (x-y) plane Δz = 10.7 m from the antenna. The Alfvén wave E and B field are mostly perpendicular to the background magnetic field direction.

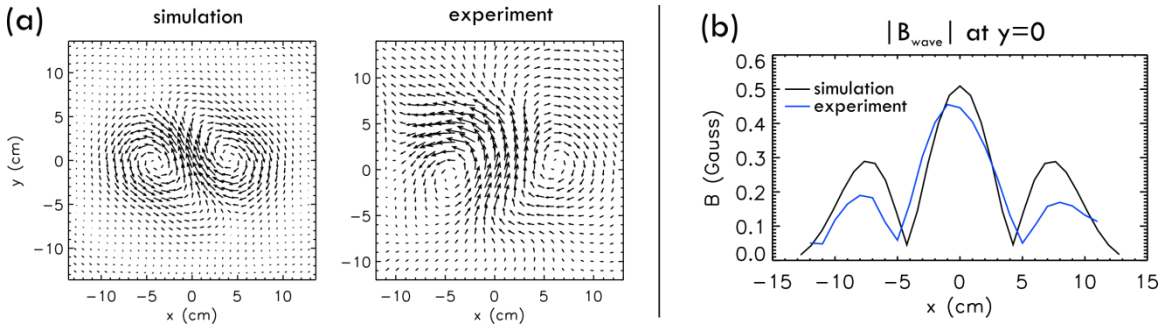

Fig 5.2: Comparison of simulated antenna radiation pattern with experimental measurement.

The Alfvén wave calculation is based on a uniform background magnetic field whereas in the experiment the wave propagates through the magnetic mirror. The measurements by B-dot probes show a very similar wave pattern inside the mirror as that in the straight field section, with a small difference in perpendicular spread of the wave pattern due to the diverging magnetic field lines. The wave frequency is below the local ion cyclotron frequency as it propagates through the mirror (from 0.4 f_{ci} to 0.7 f_{ci}). No reflection of the wave is observed. The shear Alfvén wave propagation along a parallel magnetic field gradient has been studied in detail by [Vincena 2001]. In that study, a WKB type solution of the wave equation, where the parallel wave number is considered as a function of parallel position, is calculated and compared with an experimental measurement. The study found that the wavelength decreases in accord with the WKB solution as it propagated from a region of f/f_{ci}=0.5

along a decreasing background field to f/f_{ci}=1.1. Under the condition in our experiment, the Alfvén wavelength is estimated to decrease to about half of its value outside the mirror when it reaches the field minimum. Because the size of the mirror is small compared to the wavelength (Fig 5.3), this effect is neglected in the simulation.

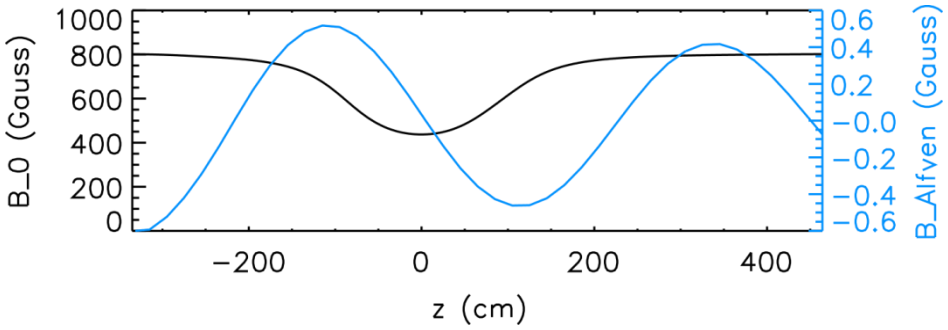

Fig 5.3: Axial profile of the magnetic mirror and the simulated Alfvén wave field (only B_x component is shown) in the calculation domain. The RMF antenna is at z = - 435 cm and the wave propagates to the right. The decreasing amplitude of the wave is due to collisional damping in the modeled plasma.

A total of 94,622 electrons are injected in the middle plane of the magnetic mirror ($z=0$). The electrons are initially uniformly distributed in the parameter space of (i) x-y coordinates of guiding centers in a 20 cm square centered on the magnetic axis; (ii) energy in the range of 100 – 500 keV; (iii) pitch angle in the range of 45^o - 90^o. The trajectories of the electrons are tracked one at a time over a period of 10 Alfvén wave cycles. The wave amplitude is ramped up from zero during the first wave cycle, then it is kept at a constant amplitude till ramped down to zero during the 10^{th} cycle. An absorption boundary condition is imposed in the simulation, that when an electron hits the

boundary of the calculation box it is considered as lost from the mirror trap. The waveguide in the experimental setup is simulated by an additional absorbing volume at its corresponding location. Due to the drift motion in azimuthal direction, radially lost electrons are collected in this volume. The modeled Alfvén wave is not affected by the ring electrons.

The motion of the test particles is traced by numerically integrating their relativistic equations of motion using the Boris mover scheme [Boris 1970]. This part of the simulation code is adapted from the particle pusher in the UCLA parallel Particle-in-Cell (UPIC) Framework [Decyk 2007], which provides high stability and accuracy. The relativistic Boris mover scheme used in this simulation is included in Appendix D. Time is discretized with a time step Δt chosen much smaller than the period of electron cyclotron motion τ_{ce} ($\Delta t / \tau_{ce} \leq 3\%$ in this study). For each test particle, 6×10^6 time steps are calculated.

5.2 Results

The electron motion in the static magnetic mirror in absence of the shear Alfvén wave is tracked. The electrons gyrate in the background magnetic field, bounce in the axial direction between the mirror points and drift in the azimuthal direction due to the gradient and curvature of the magnetic field. The total kinetic energy is well conserved (Fig 5.4). The three adiabatic invariants (μ, J and Φ, see Eq 1.1-3) associated with the three periodical motions of the trapped electrons are calculated for each test particle, and shown to be conserved as well (Fig 5.4). 41,521 out of a total 94,622 electrons are trapped by the mirror, the rest are either lost from the mirror due to small pitch angles or

their orbits are intercepted by the waveguide. The trapped electrons orbits are compared with that in the presence of the Alfvén wave.

The shear Alfvén wave is scaled to a peak amplitude of 0.5 Gauss (about 0.1% of the background field) to match the experimental measurement. This low amplitude wave produced very little effect on the trajectories of the test particles. Only about 0.2% of the originally trapped electrons are lost as a result of the presence of the wave. Shown in Fig 5.5 is the evolution of 10 randomly chosen lost electrons, from which one can hardly tell any apparent trend. The lost electrons have orbits very close by the waveguide. Their orbits, perturbed by the Alfvén wave, are intercepted by the waveguide. No electron is observed to be de-trapped axially. Both left handed and right handed circularly polarized waves are tested. Both waves cause similar electron loss.

We increase the amplitude of the model shear Alfvén wave up to 50 Gauss, which not a realistic amplitude and is only for the purpose of studying the electron loss mechanism. The number of the lost electrons increases when the wave strengthens for both RH and LH waves (Fig 5.6). The RH wave is about twice effective as the LH wave for electron de-trapping in the radial direction. At the amplitude of 50 Gauss, a small number of electrons are de-trapped axially into the loss cone by both RH and LH waves. The time history of electron loss by the 50 Gauss RH wave is shown in Fig 5.7. An oscillation at the Alfvén wave frequency appears in the radial electron loss rate, but not in the axial one.

The evolution of 20 randomly chosen electrons that are lost in axial direction is shown in Fig 5.8. For these electrons, the kinetic energy is preserved, while all three adiabatic invariance are violated due to the large perturbation

(about 10%) of the magnetic mirror field. The pitch-angle distribution of all test particles (Fig 5.10) is changed by the wave near the loss cone, which result in the axial loss. As for the radially lost electrons, again we show the evolution of 20 randomly chosen particles (Fig 5.9). For these electrons, only the 3rd adiabatic invariance, the magnetic flux enclosed by the guiding center azimuthal drift orbit), is violated. The wave moves the particles guiding centers radially outwards and causes particle loss when they hit the waveguide region. Fig 5.11 shows the distribution of the guiding center radial position before and after the application of the Alfvén wave.

The radial electron loss rate fluctuates in time in a similar manner as the experimental observation, whereas the axial loss rate does not show such modulated fluctuation (Fig 5.7). It is worth noting that the fluctuation appears in cases with both LH and RH waves. This modulation in the radial loss rate is further explored by removing the wave at the end of the 5th cycles. After the wave is removed, the electron loss rate tapered off smoothly without any fluctuation at $f_{Alfvén}$ (Fig 5.12).

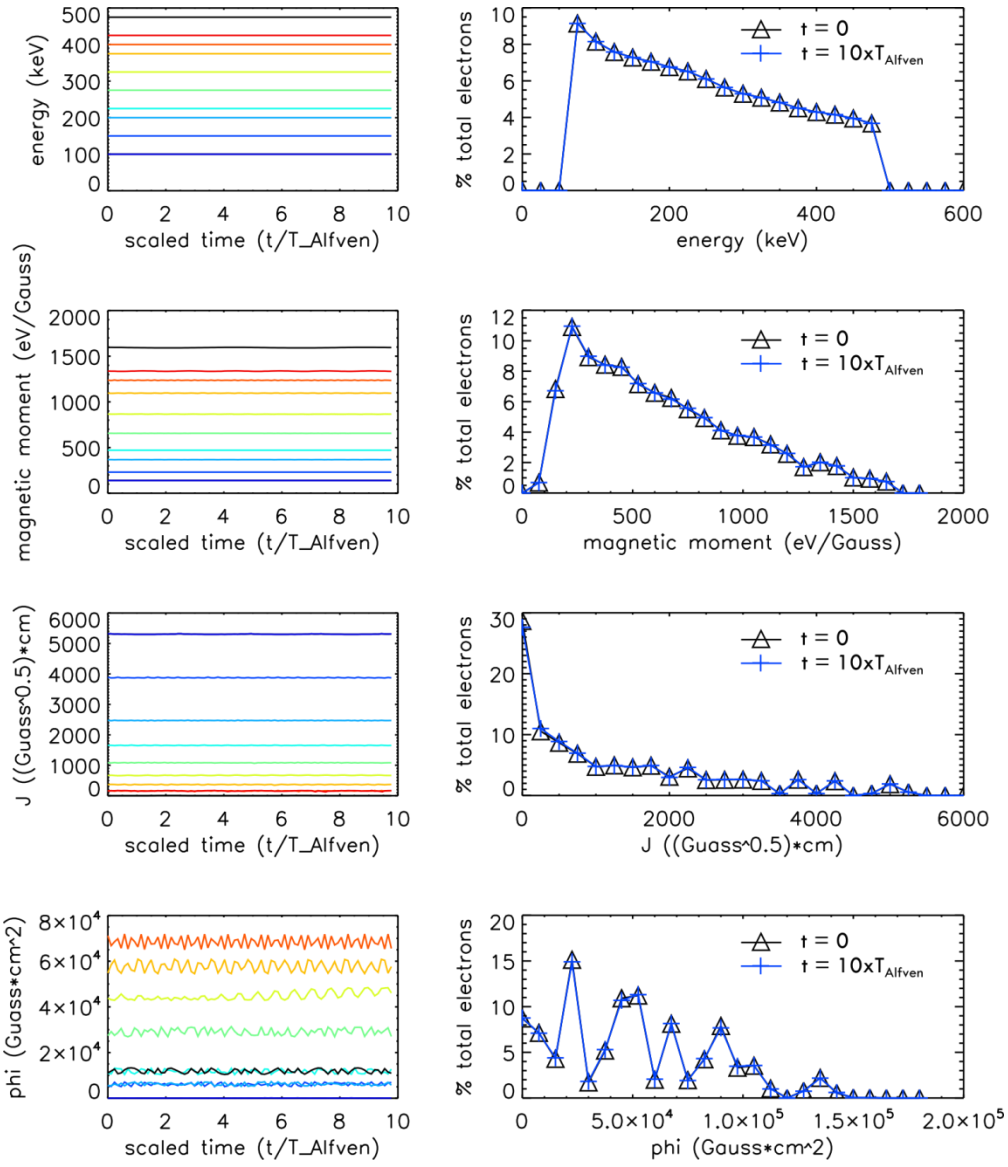

Fig 5.4: (left col.) Kinetic energy and adiabatic invariants evolution of 10 (color coded) randomly chosen test particles trapped in the magnetic mirror, in absence of the Alfvén wave. (right col.) Distribution function of 41,521 trapped electrons, compared at the beginning and end of the simulation time.

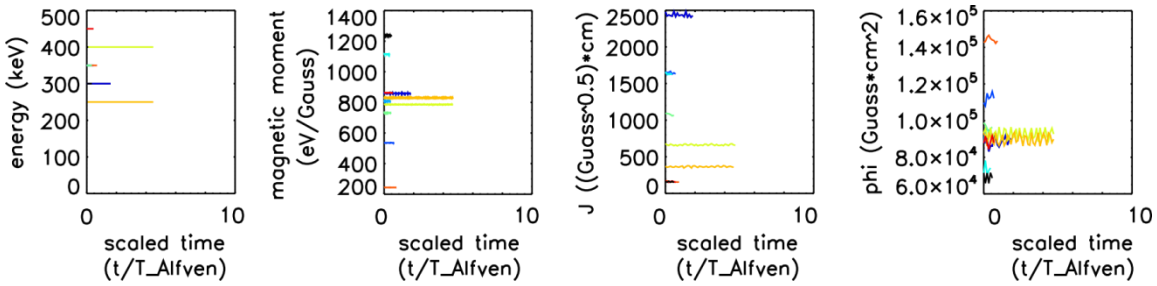

Fig 5.5: Evolution of 10 randomly chosen particles lost by the application of a 0.5 Gauss RH wave.

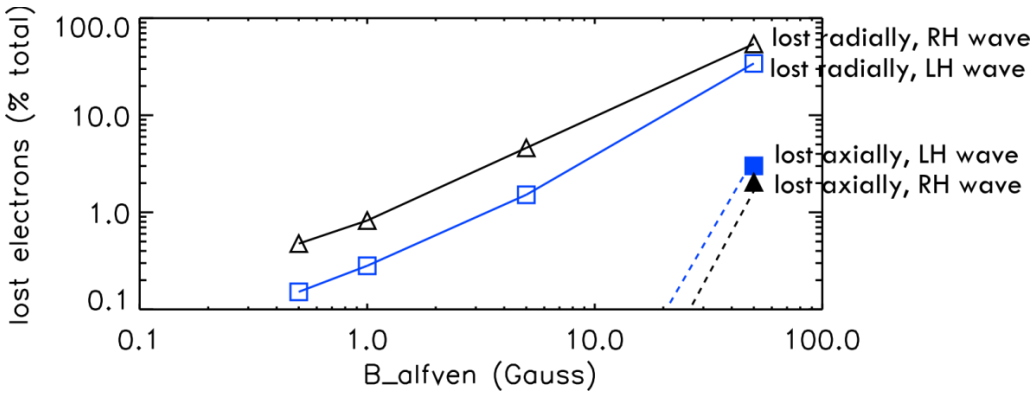

Fig 5.6: Number of lost electrons at 4 different levels of wave amplitude (0.5, 1, 5, 50 Gauss respectively). The apparent threshold value of the wave amplitude for the axial loss (no axial loss is found with waves less than 50 Gauss) is very likely caused by the discretization of the initial electron distribution function.

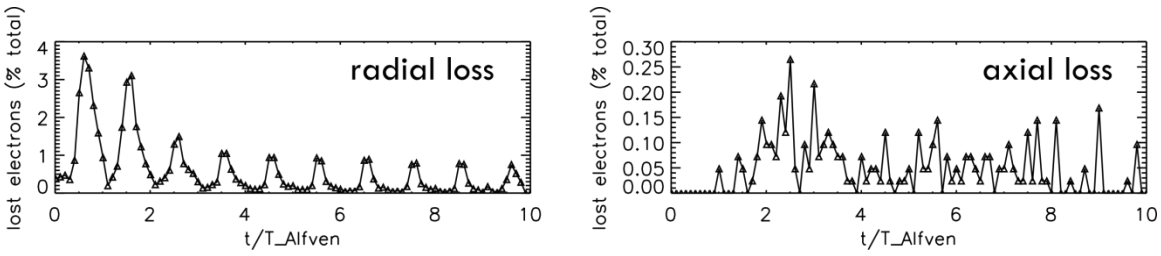

Fig 5.7: Time history of electron loss with application of a 50 Gauss RH wave.

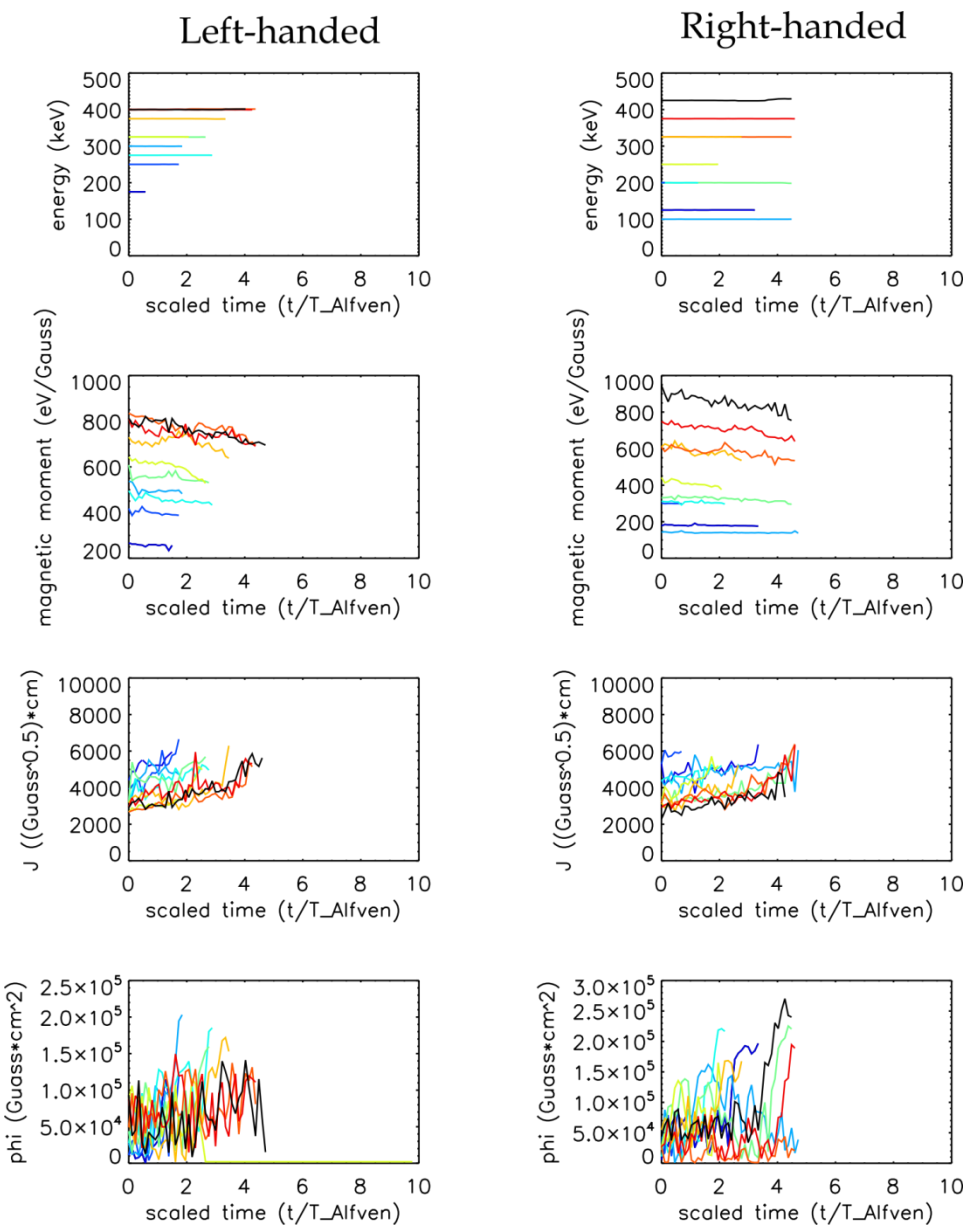

Fig 5.8: Evolution of 10 randomly chosen test particles de-trapped in the axial direction by a 50 Gauss wave, with LH or RH polarity respectively. Test particles kinetic energies are well conserved. The 1st adiabatic invariant (magnetic moment μ) is broken by the wave, which causes the violation of higher order adiabatic invariance (J and Φ). The two cases with different wave polarities behave very similarly.

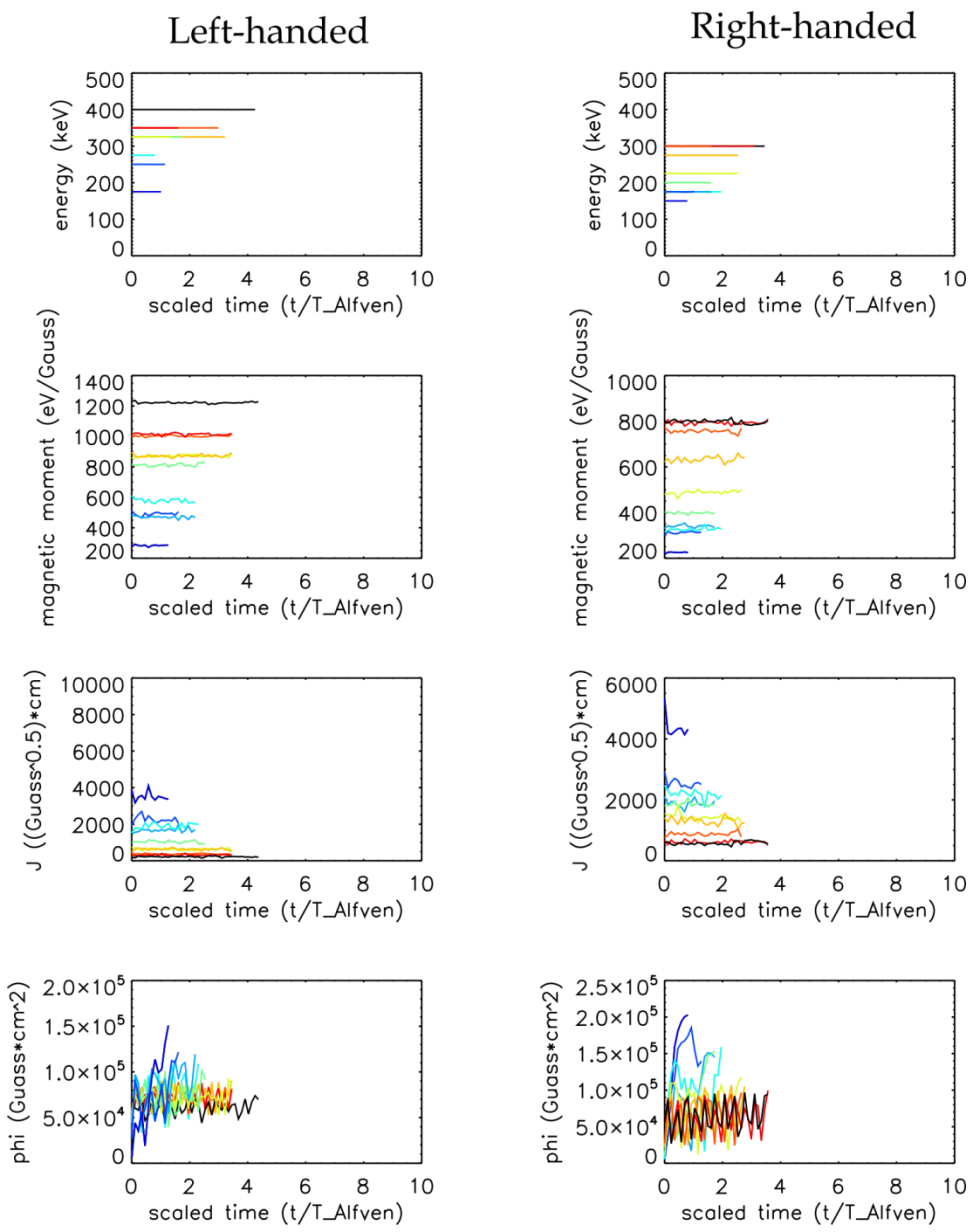

Fig 5.9: kinetic energy and adiabatic invariants evolution of 20 randomly chosen test particles (color coded) that are de-trapped in the radial direction by a 50 Gauss shear Alfven wave.

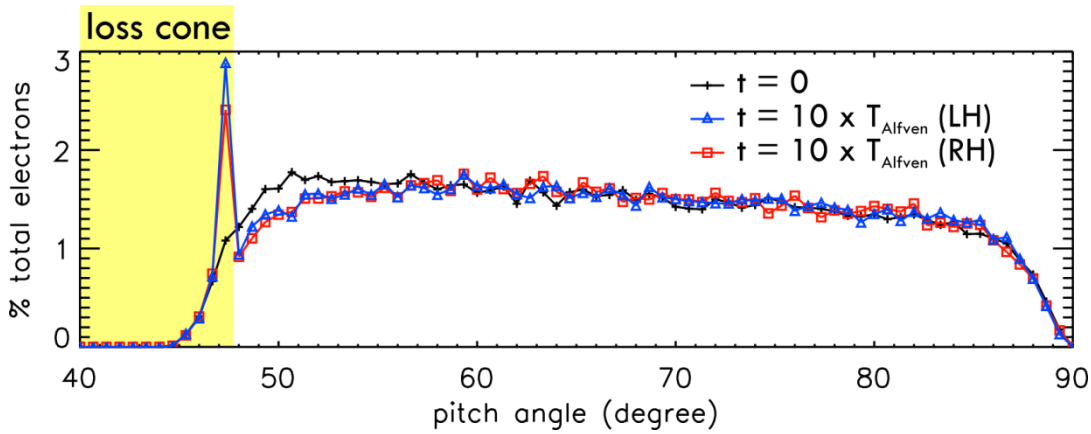

Fig 5.10: Pitch angle distribution function before/after the application of a 50 Gauss Alfvén wave. The loss cone angle of this mirror configuration is also shown. The pitch angle is calculated as the angle between velocity and B_0 when the particle is at the center plane of the mirror trap. Note that in the experiment presented in Chapter 4 there is neither a 50 Gauss Alfvén wave (the real wave amplitude is about 0.5 Gauss), nor electrons with pitch angle close to the loss cone (minimum electron pitch angle is measured to be 56 degree).

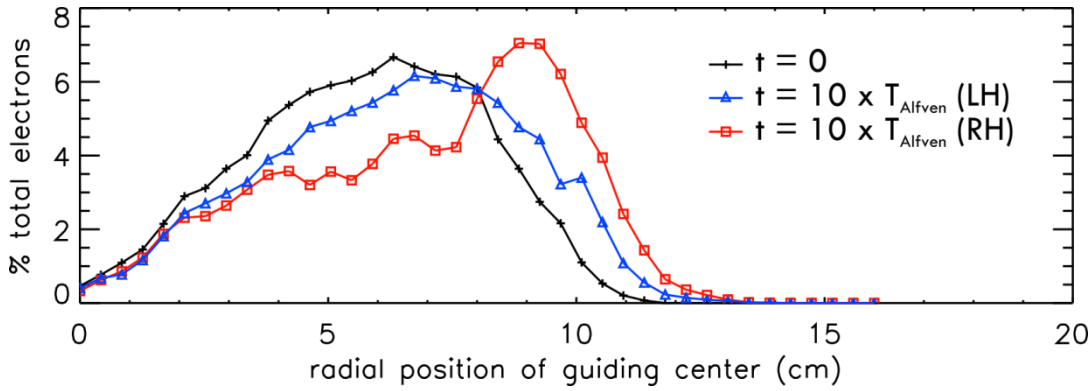

Fig 5.11: Distribution functions of radial position of electrons guiding center before/after the application of a 50 Gauss Alfvén wave.

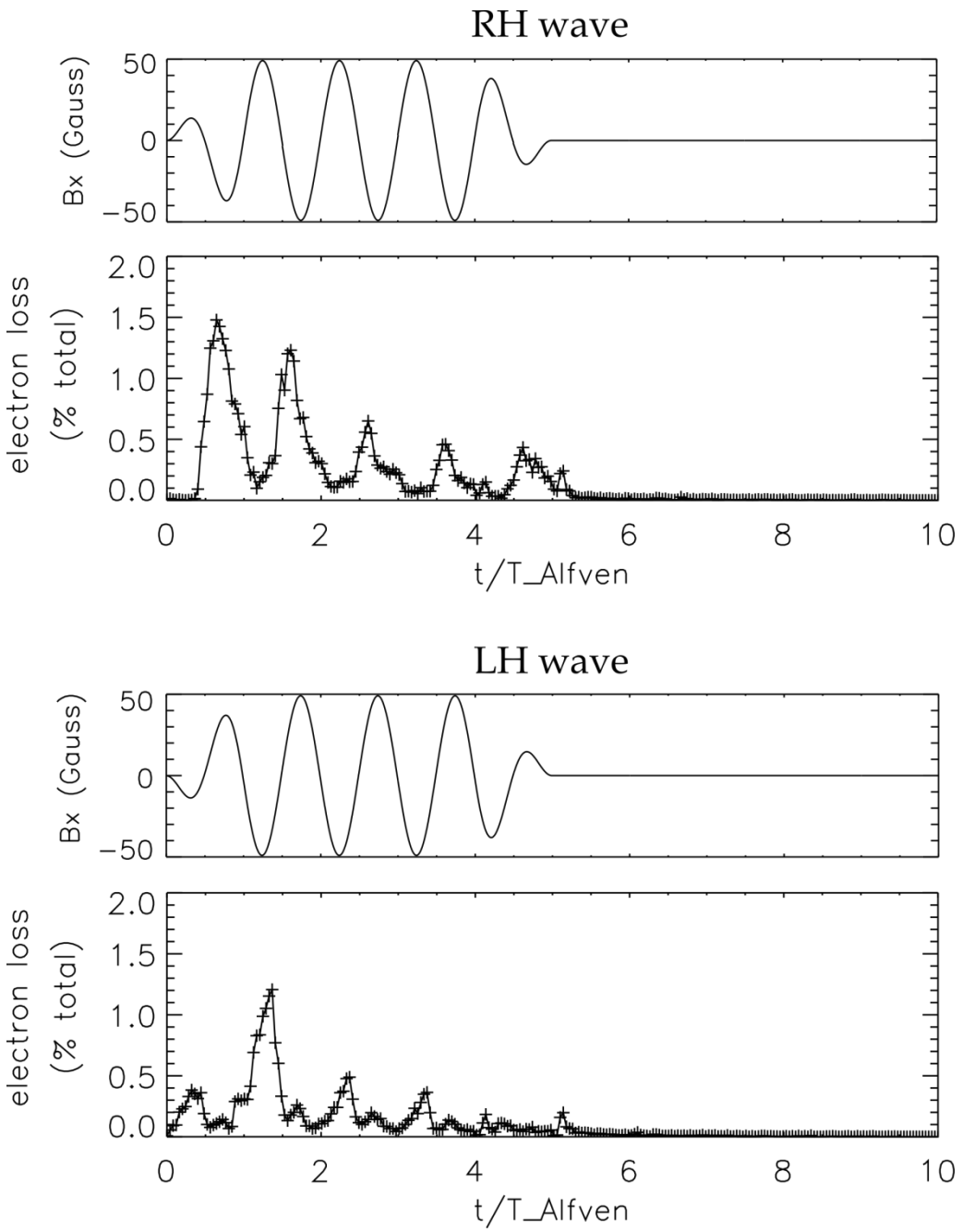

Fig 5.12: time history of the electron loss when a 50 Gauss Alfvén wave is applied for 5 cycles. B_x component of the wave at the center of the mirror is also shown for comparison. Current in the RMF antenna is ramped up from zero during $t = [0,1] \times T_{Alfvén}$, and ramped down to zero during $t = [4,5] \times T_{Alfvén}$.

5.3 Discussion

The simulated test particle trajectory agrees with prediction by theory of single particle motion. It is worth noting that in absence of the Alfvén wave, particle energy and all three adiabatic invariants are conserved precisely even after evolving the particle for 6 million time steps. In this single particle picture, the loss of electrons is caused by perturbation of the magnetic mirror trap, and the efficiency increases with the wave amplitude.

Though some results from the simulation appear in accord with experimental observation, such as the modulated electron loss rate (Fig 5.7 as an example), major discrepancies exist.

To begin with, both LH and RH wave can de-trap electrons in the simulation. For the radial loss, the RH de-traps more electrons compare to the LH with a ratio of roughly 2:1. This polarity preference is likely to be caused by longer interaction time of the RH wave with the right-handed drifting electrons. To scatter the particles into the loss cone, the two polarities are almost equally effective. In a single particle picture, the time scale associated with magnetic moment conservation is the electron cyclotron period. The Alfvén wave field is nearly frozen at this time scale, therefore the two wave polarities should cause the same axial loss. However, clear evidence is found in the experiment that both the radial and axial electron losses are due to the RH wave only. No x-rays are observed when applying an LH wave in the experiment.

In the simulation, no electron is scattered into the loss cone until the wave amplitude is increased to 50 Gauss, which is 100 times stronger than the wave in the experiment. These de-trapped electrons have pitch-angles very close to the loss cone angle (Fig 5.10), which means they are barely trapped by

the mirror field. In the experiment the fast electrons gain energy from the ECRH, which mainly increases the electron perpendicular energy thus the electrons are highly anisotropic. The measured lower boundary of the fast electron pitch angle in the experiment is 56 degrees, which well above the loss cone angle. Therefore, in the experiment these electrons are very unlikely to be de-trapped by the low amplitude wave in the same manner as shown in the simulation. In this case, there should be little surprise that the simulated axial loss rate does not oscillate as that observed in the experiment.

After the termination of the Alfvén wave the electron loss continues for more than 50 Alfvén wave cycles in the experiment, in both radial and axial direction, with a clear modulation at the frequency of the Alfvén wave (Fig 4.7). In comparison, a small portion of the electrons are lost after the removal of the Alfvén wave field, due to the breaking of 3rd adiabatic invariant. However no oscillation at the Alfvén wave frequency in time history of electron loss is found.

In conclusion, what we have learned from this test particle simulation is that although it is possible to de-trap electrons by a large amplitude Alfvén wave only considering single particle motion, it is not adequate to explain the experimental observation. One must go to more complicated interactions between the plasma, the Alfvén wave and the fast electrons to seek an explanation.

CHAPTER 6

Discussion and Conclusions

This dissertation has investigated the loss of fast electrons from a magnetic mirror trap when irradiated by a shear Alfvén wave ($f<f_{ci}$). The experiment is performed in the quiescent LaPD after-glow plasma. The magnetic field is programmed to include a magnetic mirror section. A trapped fast electron population is generated in the mirror section by X-mode high power microwave pulses. Different power level, pulse duration and heating scheme leads to different electron energies. Two distinct electron energy ranges are studied separately in this work.

The hot electron generation by microwaves is found to be more efficient at the second harmonic electron cyclotron resonance (ECR) frequency ($f_{microwaves} = 2 f_{ce}$) compared to at the fundamental ECR frequency ($f_{microwaves} = f_{ce}$) or the upper-hybrid resonance frequency ($f_{microwaves} = f_{uh}$). In this work, the generation of mirror trapped electrons with energies around 100 eV is accomplished by a 3 ms microwave pulse with a peak power of 5 kW injected to the middle of the mirror at f_{UH}. To generate electrons at 100 keV level, the 2nd harmonic ECR configuration is adapted with microwave pulsing for 30 ms at peak power of 10 kW.

For the lower energy range of the trapped electrons, production by microwaves is observed via different diagnostics such as Langmuir probes, soda-straw probes and visible light photography. A shear Alfvén wave is

launched by a RMF antenna, at an amplitude corresponding to of about 0.1% perturbation to the background magnetic field. Every diagnostic indicates that the trapped electrons are significantly mitigated by the shear Alfvén wave.

At this energy level (~100 eV), the period of electron bounce motion between the mirror points is close to the wave period, thus it is possible to break the second adiabatic invariant J (Eq 1.2). However this mechanism requires a large parallel wave electric field, which the shear Alfvén wave does not have. Thus the de-trapping cannot be explained by single particle motion, and more detailed measurements need to be made before a mechanism can be concluded. The fact that de-trapping is observed for both LH and RH waves in this experiment suggests the mechanism behind this experiment may be different from the experiment with more energetic electrons.

For the higher range of electron energy (~100 keV), hard x-rays are generated by the fast electrons when they strike the machine wall or other metal objects in the chamber, which are used as primary diagnostics to study the fast electron confinement in the presence of a shear Alfvén wave. The x-ray diagnostics have several advantages over that used in the earlier experiment: better time and energy spectrum resolution, no electrostatic noise pickup which degrades signal to noise, and most importantly it directly corresponds to electrons that are de-trapped from the mirror.

Hard x-ray tomography, constructed from more than 1000 chord projections at each axial location, shows electrons are lost in both the radial and axial direction. Of special interest are the axially lost electrons, as such electron losses have direct implication of radiation belt remediation, which is the primary motivation of this study. The electrons are well confined by the mirror

field in absence of the Alfvén wave, with a measured lower limit of pitch-angle distribution well above the loss cone (9° gap, i.e. for a 100 keV electron $\Delta E_{\parallel} \geq 15keV$ is required to reach the loss cone). Analysis of single electron motion shows that in order to change the electrons pitch angle by such amount, at least a 10% perturbation of the background field is required. This is very unlikely to be the case in the experiment, where the wave field is measured to be 0.1% of B_0.

The temporal history of the electron loss has been examined as well. Irradiated by the Alfvén wave, the loss of electrons is modulated at $f_{Alfvén}$. Numerous radiation belt observations show a strong correlation between the observed VLF waves (which is excited by the anisotropy of trapped energetic electrons) and simultaneous MHD oscillations (at much lower frequency) [Sato 1974]. Various mechanisms for such interaction are proposed, such as drift-resonance acceleration from the ULF poloidal electric field [Southwood 1981] [Zong 2009], electron precipitation caused by lowered mirror points due to magnetic field oscillation [Brito 2012] , or diffusive transport due to stochastic non-linear particle-wave interaction [Ukhorskiy 2006].

The periodical loss of the electrons is found to be caused only by the RH circularly polarized component of the Alfvén wave. When a LH wave is applied, no x-rays are produced; when a LH wave is mixed with a RH wave, the effect on the x-rays is the same as that caused by only the RH wave component. This means that the LH polarized wave passes through the hot electron ring and does not interact with it at all. At the time scale of electron gyro-period, the wave is essentially stationary, thus the different polarizations are not distinguished by means of electron gyration. Another type of electron motion in

the perpendicular direction is the azimuthal drift, which is also in the RH direction. The time scales for this drift motion is comparable to the period of the Alfvén wave (Fig 6.1), therefore it is possible that the different polarization is distinguished by mechanisms associated with the azimuthal rotation of the electron ring.

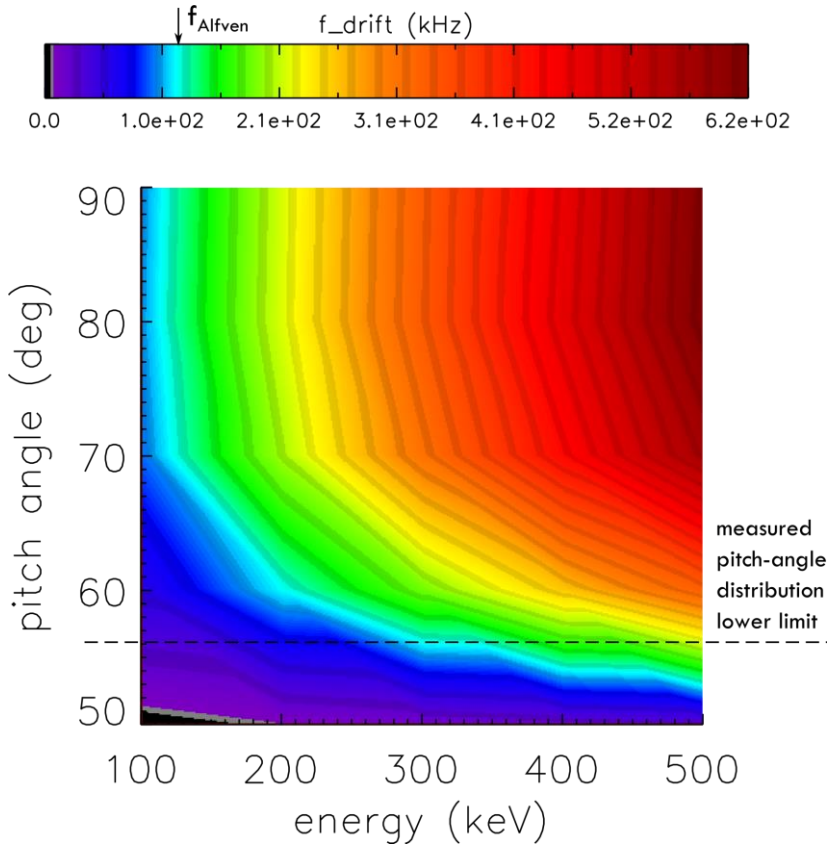

Fig 6.1: Frequency of the electron grad-B and curvature drift, as function of electron energy and pitch-angle. The Alfvén wave frequency, shown in light blue, can be matched by the azimuthal drift frequency of electrons with proper combination of energy and pitch angle. The measured minimum hot electron pitch angle in the experiment is 56 degree, which implies that the drift resonance energy range is 100 ~ 300 keV.

One hypothesis directly resulting from this analysis is that, a single electron can experience a radial $\vec{E}\times\vec{B}$ drift, where $\vec{E}$ in the azimuthal direction comes from the perpendicular electric field of the Alfvén wave and $\vec{B}$ is the background magnetic field (Fig 6.2). If the electron guiding center drift motion is in phase with the rotation of the wave pattern, then the radial drift does not change sign for a long time, therefore the displacement accumulates and the electron can be moved radially outward (or inward, depending on the relative phase between the drift motion and the wave) from the mirror center. The electric field of the Alfvén wave is estimated to be $E_{\perp}=0.5V/cm$. At this amplitude, the time it takes to displace the ring by 1 cm is about one Alfvén wave cycle.

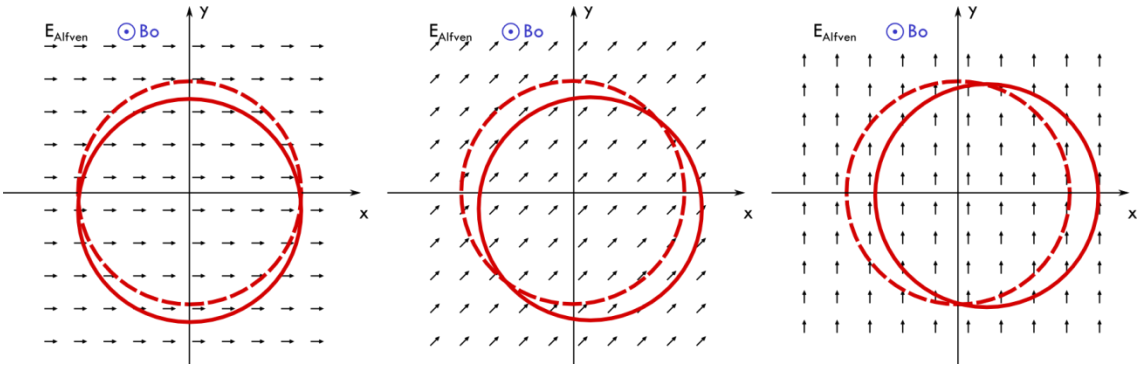

Fig 6.2: Cartoon of ring displacement due to $\vec{E}\times\vec{B}$ drift, at three phases of the wave. The electric field of the Alfvén wave field is simplified as a uniform rotating field. The original positions of the trapped electron guiding centers in absence of the wave is denoted by doted circles, and the displaced positions due to the wave field are the solid circles.

With this hypothesis, as the displacement of the ring rotates in phase with the wave, the x-rays that are produced on the waveguide fluctuate at the wave frequency. This hypothesis also explained the experimental observation that if the asymmetry caused by the waveguide is compensated by inserting a probe on the opposite side of the ring, the x-ray fluctuation is mainly twice the wave frequency (Fig 4.11).

There are also facts that cannot be explained by this hypothesis alone. For example, the axial loss of electrons cannot come from direct single particle motion in the wave field. Another example is the continuous electron loss after the termination of the wave. The rotating of the displacement may still persist, but those electrons that are displaced far enough from the ring center should already have been absorbed by the waveguide, and since no further displacement can be caused in absence of the wave, there should be no more modulated electron loss. The discrepancy between the hypothesized model and the experimental results are confirmed by the test particle simulation presented in Chapter 5.

Though not complete, this hypothesis can be the first step toward explaining these observations. Unlike what is shown in Fig 6.2, the wave pattern in the experiment is not uniform. Instead of a translational displacement in position, the ring may be deformed because different parts of the ring experience drift in different directions. Such three dimensional spatial distortion of the ring may establish a large scale global electric field, which in turn affects the confinement of the ring and could lead to axial loss. Such scenario would be very similar to what is frequently happening in the ring current in the Earth's radiation belt, where the particle drift trajectory is

perturbed by electric field in geomagnetic storms [Nishimura 2007] [Ukhorskiy 2006].

6.1 Future work

The current experimental study is largely based on the hard x-ray diagnostics, which provide information about the electrons that are lost from the mirror. Additional diagnostics of the hot electrons that are trapped inside the mirror would be very informative. Examples of these diagnostics include ECE (Electron Cyclotron Emission) imaging of the hot electron ring, and spatially resolved measurement of the bremsstrahlung x-rays radiated from electron collisions with the helium ions and atoms in the magnetic mirror. Although getting a desirable spatial resolution to measure the ring distortion requires major efforts, these direct measurements of the trapped ring itself would be very helpful to establish a model of the ring distortion. On the other hand, the temporal variation in the measurement of the trapped electron may also provide rich information about the ring modulation.

Presumably there is also an electron population in the energy range of 1 keV ~ 100 keV present in the hot electron ring. However its behavior is largely unknown due to limitations of the current diagnostics. An x-ray detector located inside the vacuum vessel would provide useful information about this lower energy electron population.

An experiment which scans the frequency of the shear Alfvén wave would be interesting. The collective mode of the ring that leads to the loss may have a dispersion relation that the frequency scan experiment may help identify.

This study can be further explored with a detailed theoretical model of the collective behavior of a distorted hot electron ring, which is very likely coupled to the cold background plasma, to eventually understand the mechanism causing the axial loss of the electrons from the magnetic mirror. Such model may even potentially lead to innovative schemes to artificially modify the profile of the ring current drifting in the Earth's magnetic field, to catalyze the change in dynamics of radiation belts and the subsequent remediation.

Although the mechanism proposed in this chapter fit the experimental observations very well, it is wise to keep an eye open for other possibilities. In the model presented here, the Alfvén wave pattern rotation is in phase with the ring rotation caused by grad-B and curvature drift, which requires right-handed rotation at appropriate frequencies. Other collective modes of the ring may have similar requirements of the wave. For example, a diocotron mode or a drift-like mode of the ring, caused by pressure gradient of the ring, may be driven by an Alfvén wave rotating in the same direction as these modes. In this case, further measurements such as the ring density and temperature profiles are needed to calculate the mode frequency, and may provide additional check on the electron loss mechanism.

Appendix A

Dot by Dot Reconstruction (DDR)
- A novel tomography algorithm

Tomography is the technique to produce 2D cross-sectional images (tomogram) of an object without intruding it. A set of line-integrated data is acquired, usually in the form of measurement of the absorption of x-ray beams (such as in the case of medical CT imaging), propagation of seismic waves (in the case of seismic tomography), or collimated x-ray emission (such as in this experiment). To produce a tomogram from the line integrals, some reconstruction algorithm is needed. Over the past few decades numerous reconstruction methods have been introduced and repeatedly performed [Hsieh 2009], largely driven by medical applications, and new methods are likely to emerge with the growth of computational power. Here we describe a Dot by Dot Reconstruction (DDR) method that we developed, and have found to be an improvement over the existing methods for this study.

The rest of this appendix describes the DDR method and is organized into 5 parts. **The 1st part** discusses a concept essential to the DDR method: presenting the integrated measurements in the projection parameter space. In **the 2nd part**, the tomography reconstruction problem is re-introduced from a new perspective that directly leads to the DDR method. In **the 3rd part**, a point-selection criteria is defined, which is calculated by using the integrated measurement, and is used throughout the DDR reconstruction process. Next, the full DDR reconstruction procedure is described. Some discussions of the

procedure are included in the **4th part** of this section. Finally in **the 5th part**, the new method is compared with previously published methods with simulated data, and is shown to be more effective.

I. Presenting measurement in projection parameter space: S(t,θ)

We parameterize each line projection on a transverse plane by (t,θ), where t is the impact parameter of the chord offset from the vacuum chamber center, and θ is the angle from the x-axis (Fig A1). The x-ray emissivity distribution function $f(\vec{r})$ is the x-ray power emitted per unit volume at spatial location $\vec{r}$, with units of W/m^3. An actual detector measures emission from a finite span of angles. Therefore the measurement

$$S(t,\theta)=\frac{1}{4\pi}\int f(\vec{r})\Omega(\vec{r},t,\theta)\,d\vec{r}\,, \tag{A.1}$$

where $\Omega(\vec{r},t,\theta)$ is the solid angle that the detector subtends at the spatial point $\vec{r}$, when the detector is collimated to the (t,θ) direction.

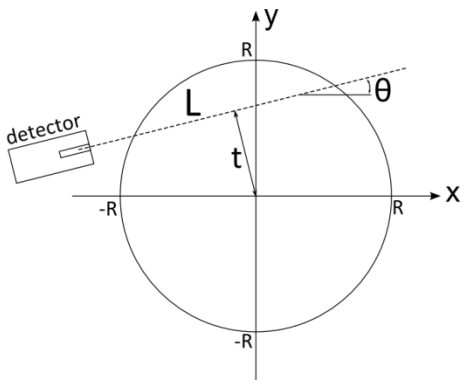

Fig A1: A drawing of the tomography geometry in the transverse x-y plane. The sign of t is defined as the sign of the y-intercept.

If the collimator is narrow enough and the detector is far enough from the volume of interest, the detector can be considered as an ideal collimated detector, for which Ω is uniform along the line of sight $L_{(t,\theta)}$ in the volume of interest. $L_{(t,\theta)}$, as shown in Fig A1, is described by parametric equations

$$\begin{cases} x = l\cos\theta - t\sin\theta \\ y = l\sin\theta + t\cos\theta \end{cases}, \; l \in (-\infty, \infty)$$

Here l is the length along the chord. If we assume the emissivity is uniform in the z-direction, we can write a 2D emissivity as $f(x,y)$, and the measurement $S(t,\theta)$ in units of W/m^2 can be defined as the line integral of $f(x,y)$ along $L_{(t,\theta)}$:

$$\begin{aligned} S(t,\theta) &\equiv \int_{L_{(t,\theta)}} f(x,y)dl \\ &= \int f(l\cos\theta - t\sin\theta, l\sin\theta + t\cos\theta)dl \end{aligned} \tag{A.2}$$

For a single point source at (x_0, y_0) with intensity ε, the emissivity is

$$f(x,y) = \varepsilon\delta(x - x_0)\delta(y - y_0), \tag{A.3}$$

From (A.2) and (A.3), and using $\delta(ax) = \delta(x)/|a|$ for non-zero a, the measurement $S_0(t,\theta)$ arising from this one-point emission profile is

$$\begin{aligned} S_0(t,\theta) &= \int \varepsilon\delta(l\cos\theta - t\sin\theta - x_0)\delta(l\sin\theta + t\cos\theta - y_0)dl \\ &= \int \varepsilon \frac{\delta(l - \frac{t\sin\theta + x_0}{\cos\theta})}{\cos\theta}\delta(l\sin\theta + t\cos\theta - y_0)dl \\ &= \frac{\varepsilon}{\cos\theta}\delta(\frac{t\sin\theta + x_0}{\cos\theta}\cdot\sin\theta + t\cos\theta - y_0) \\ &= \varepsilon\delta(y_0\cos\theta - x_0\sin\theta - t) \end{aligned} \tag{A.4}$$

where $\theta \in (-\frac{\pi}{2}, \frac{\pi}{2})$. In the case of $\theta = \frac{\pi}{2}$, (A.4) still holds since

$$S_0(t,\frac{\pi}{2}) = \int \varepsilon\delta(-t-x_0)\delta(l-y_0)dl = \varepsilon\delta(-t-x_0) = \varepsilon\delta(y_0\cos\theta - x_0\sin\theta - t).$$

Therefore, the measurement of a point source at (x_0, y_0) is represented by a curve $\Gamma_{(x_0,y_0)}$ in the (t,θ) projection parameter space. The curve, labeled by the point (x_0, y_0), can be expressed by writing t as a function of θ:

$$t_{(x_0,y_0)}(\theta) = y_0\cos\theta - x_0\sin\theta, \quad \text{where } \theta \in (-\frac{\pi}{2}, \frac{\pi}{2}]. \qquad \text{(A.5)}$$

Only when the detector's line of sight (t,θ) satisfies (A.5) can it detect emission from the point source at (x_0, y_0). For example, for a point source shown in Fig A2(a) located at $(x_0, y_0) = (1,1)$, the detector will see the source on any line of sight that has a projection parameter that lies on the dark curve in Fig A2(b), such as $(t,\theta) = (1,0)$. Such (t,θ) combinations, which represent all chords going through the point source, form the curve $\Gamma_{(x_0,y_0)}$ which is described by (A.5).

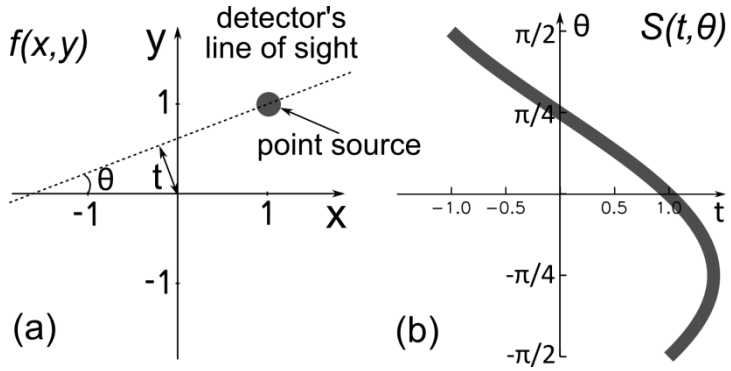

Fig A2: A point source, shown in (a), is measured from different angles θ and different impact parameter to the coordinate origin t. Presented in a (t,θ) coordinate, the measurement of a point source forms a curve, as shown in (b).

Because the above transformation is linear in f, a collection of point sources at locations of $P=\{(x_i,y_i)_{i=1,\ldots,N}\}$ with uniform intensity ε in image space (x,y) have a chord integrated measurement $S_P(t,\theta)$ which is the superposition of the curves $\Gamma_{(x_i,y_i)}$:

$$S_P(t,\theta)=\sum_i \varepsilon\delta(y_i\cos\theta-x_i\sin\theta-t). \qquad \text{(A.6)}$$

II. The problem of tomography reconstruction from a new perspective

The tomography reconstruction problem in its most common form is simply to calculate an emission profile $f(x,y)$ corresponding to a given measurement $S(t,\theta)$. It is the inverse process of the previously discussed process of getting measurements by integrating an emission profile.

The emissivity $f(x,y)$ is a continuous function, but we assume it can be approximated by a set of emitting points with a small and uniform intensity ε. These emitting points can overlap to account for different intensities at different locations. As above, we designate the locations of these emitting points by P. In this perspective, the tomography reconstruction problem can be stated as: given the chord integrated measurement $S_P(t,\theta)$ of a set of point sources with uniform intensity ε, find the locations of all the points in this set P.

As previously discussed, the measurement of many point sources presented in (t,θ) space is the superposition of curves in the form of (A.6). In a reconstruction problem, we only have the left-hand side of (A.6) and wish to determine the right-hand side. Since each of these curves is labeled with the location of the point source, if we identify all the curves, then the locations of the point sources are found and the tomography problem is solved. The

question now is how to identify these curves. In the following part, a point-selection criteria is defined, which compares the measurement with a single curve in the form of (A.5) generated by an arbitrary point (x, y). With this criteria, the superimposed curves can be identified one at a time to reconstruct the emissivity profile.

III. The point-selection criteria and the procedure of DDR

For a chord integrated measurement $S_P(t,\theta)$, the point-selection criteria for an arbitrary point of interest (x, y) is defined as the average value of $S_P(t,\theta)$ over all possible angles of chords passing through the point (x, y):

$$I_{S_P}(x,y) = \frac{1}{\pi}\int_{-\pi/2}^{\pi/2} S_P\left(t_{(x,y)}(\theta),\theta\right)d\theta, \tag{A.7}$$

where $t_{(x,y)}(\theta)$ is defined in (A.5). This criteria has a more intuitive meaning, which can be found by substituting (A.5) and (A.6) into (A.7):

$$\begin{aligned} I_{S_P}(x,y) &= \frac{1}{\pi}\int_{-\pi/2}^{\pi/2}\sum_i \varepsilon\delta(y_i\cos\theta - x_i\sin\theta - y\cos\theta + x\sin\theta)d\theta \\ &= \frac{1}{\pi}\sum_i \frac{1}{\sqrt{(x-x_i)^2+(y-y_i)^2}} \end{aligned}$$

Note that every point in P represents the location of a point source of x-ray emission ε. If one equates this to a point charge, then the integral $I_{S_P}(x,y)$ is the electric potential from these charges at the point (x, y), with a constant factor of $\frac{1}{\pi}$. Therefore, one apparent way to reconstruct the emissivity f is to calculate $I_{S_P}(x,y)$ for all (x, y), which is equivalent to the electric potential field everywhere; then the reconstructed emissivity profile $f_{rec}(x,y)$, which is

equivalent to charge distribution, can be calculated by taking the Laplacian of the equivalent potential field

$$f_{rec}(x,y) = -\frac{1}{4}\nabla^2 I_{S_p}(x,y) \tag{A.8}$$

This method requires measurement S on the full (t,θ) projection space in order to exactly calculate $I_S(x,y)$. In the experiment, due to limitations described in chapter 2 of this dissertation, the projection space can only be partially sampled (see Fig 2.13). So we define the generalized point-selection criteria $\tilde{I}_S(x,y)$ as the integral only in the area where S is measured, e.g. $\theta_1 < \theta < \theta_2 : \tilde{I}_{S_p}(x,y) = \frac{1}{\theta_2 - \theta_1}\int_{\theta_1}^{\theta_2} S_P\left(t_{(x,y)}(\theta),\theta\right)d\theta$. In this case, there is not enough information for a unique reconstruction, and the following assertion is made: For two points (x_A,y_A) and (x_B,y_B), if $\tilde{I}_{S_p}(x_A,y_A) > \tilde{I}_{S_p}(x_B,y_B)$, then it is more likely that the point (x_A,y_A) belongs to P than the point (x_B,y_B) does.

Consider a set of locations $Q = \{(x_i,y_i)_{i=1,2,\ldots,M}\}$, where it is possible to have a non-zero emissivity. Essentially this is an infinite set with all points in the image space, but as an approximation, we can choose a finite number of locations uniformly distributed in the area of interest, so that any point in P can be approximated by a point in Q within a given finite spatial resolution (Because of this, the points in Q can be considered as candidate points). The DDR procedure determines which of the points in Q are the best suited to reconstruct P. Because the points in P can overlap, we allow any candidate point in Q to be chosen multiple times. As a reminder, P is the set of locations of the unit intensity point sources, whose elements can appear more than once

(strictly speaking, P is a multiset), and is the unknown set to be reconstructed. Q is the set of all possible emitting locations, in which no two elements are same.

To begin with, assume P is not empty, there is at least one candidate point in Q that is also in P. To find this point, $\tilde{I}_S$ is calculated for every point in Q, and the point q_{i1} that has the maximum $\tilde{I}_S$ is chosen. Only one candidate point can be chosen, because (a) the next best choice may represent the same point in P, and (b) the next point to be chosen may be a repeat of the same candidate point. To exclude these possibilities, we redefine the set to be reconstructed as $P^{(1)} = P - \{q_{i1}\}$, thus the measurement data needs to be updated to exclude the portion of the measurement resulting from q_{i1}, i.e. $S^{(1)} = S - S_{q_{i1}}$. Assuming $S^{(1)} > 0$ (meaning $P^{(1)}$ is not empty), using this updated measurement we calculate $\tilde{I}_{S^{(1)}}$ for every point in Q, then a second point q_{i2} (q_{i2} can be same as q_{i1} if necessary) can be chosen from Q by searching for the maximum $\tilde{I}_{S^{(1)}}$, and the measurement can be updated again: $S^{(2)} = S^{(1)} - S_{q_{i2}}$. This process can be repeated to find a set of points $\{q_{i1}, q_{i2}, ...\}$ which represent the reconstructed emissivity. The stopping condition at the i^{th} iteration is the newly updated measurement $S^{(i)} = 0$, which means $P^{(i)}$ is empty and all points in P are found. In practice this condition can be implemented as a test that the average value of $S^{(i)}$ is sufficiently small.

IV. Some discussion about DDR

In summary, we try to decompose the measured $S(t,\theta)$ into curves of the form (A.6). In the reconstruction process, the curve which represents the maximum contribution to S is treated as the most "likely" one at a given stage in the reconstruction, and the corresponding point in image space is chosen to be included in the reconstruction. When the reconstruction process is complete, we have found a set of curves in (t,θ) space corresponding to a known set of emitting points in the image space. Since the sum of these curves approximates S over the area where S is measured, the set of corresponding points is a solution to the tomography problem.

For an actual measurement with non-ideal $\Omega(\vec{r},t,\theta)$ in (A.1), the measurement $S_0(t,\theta)$ of a point source of intensity ε at (x_0,y_0) presented in the (t,θ) space is not a line of uniform intensity as in (A.4), but a curve with finite width and varying intensity. This actual $S_0(t,\theta)$ can be calculated using (A.1) once $\Omega(\vec{r},t,\theta)$ is known, which can be calculated from the collimator geometry and the detector location. In this case, the calculation of $I_{S_p}(x,y)$ can be generalized to

$$I_{S_p}(x,y)=\frac{1}{\varepsilon\pi}\int_{-\pi/2}^{\pi/2}\int_{-\infty}^{\infty}S_P(t,\theta)S_0(t,\theta)dtd\theta \qquad \text{(A.9)}$$

In the limit of an idealized case, by substituting $S_0(t,\theta)$ in the form of (A.4), (A.9) gives the same result as the original definition in (A.7).

As mentioned above, this method makes an explicit approximation, that the continuous 2D function to be reconstructed is approximated by a set of points. In other words, the emissivity function is approximated by a set of

emitting dots, and the small intensity of each of these dots ε is the "unit emissivity". The amplitude of f at a position is approximated by the number of points in the vicinity of this position. ε, which sets the amplitude resolution, should be sufficiently small for the desired smoothness of the reconstructed emission profile, but reducing its value requires increased computation time. Fig A3 shows a demonstration of this method with an arbitrary test function, which is reconstructed with ~10^4 points. The maximum value of the test function $\max(f)=1$, and the amplitude of each dot $\varepsilon=0.05$. $S(t,\theta)$ of the reconstructed image (Fig A3 (e) bottom) agrees with the original measurement (Fig A3 (a) bottom) within 0.5% error.

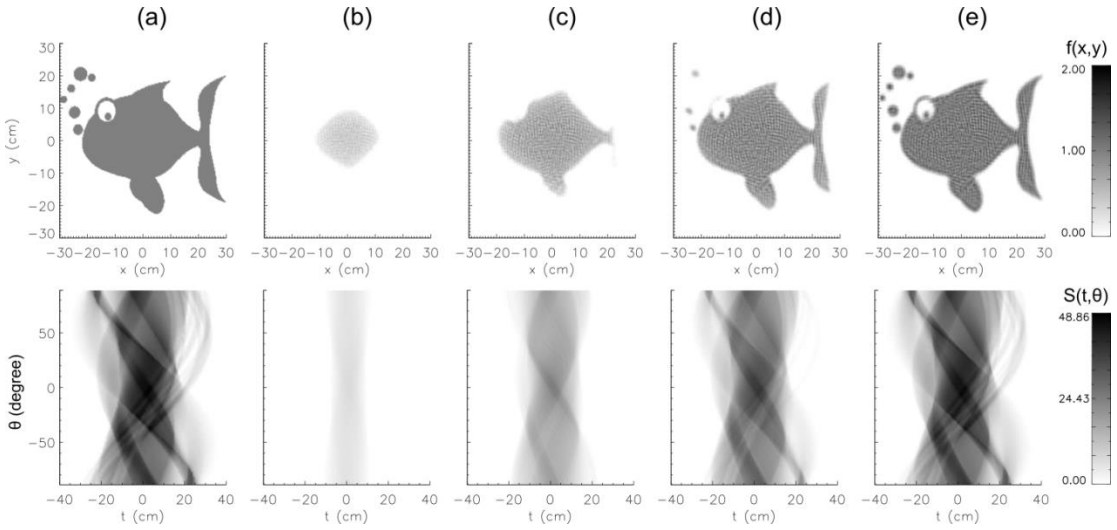

Fig A3: (a) An arbitrary test 2D emissivity. Using DDR method, 2.8×10^4 points are found one by one, to reconstruct the emissivity. The course of the reconstruction is shown in (b) – (e), which contains the first 0.2×10^4, 1×10^4, 2×10^4, and 2.8×10^4 points. The images on the top row are emissivity profiles, and their corresponding line of sight integrated measurements are shown on the bottom.

This method has several features that make it attractive for reconstructions in this experiment. First, the method works with limited measurement. Second, non-negativity of the emissivity is ensured by the reconstruction procedure, since only positive numbers are added to it. Third, to calculate the line integral the integration area should be well sampled. This requirement can be satisfied in this experiment, as in Fig.2.13 (b) the shaded area can be sampled continuously. Finally, this method empirically produces less undesired artifacts compared to some other methods with the geometry used in this experiment. Comparisons of reconstruction results by different methods will be shown in the next section.

The computation time is generally longer for DDR compared to most of the other methods tested by the authors. If S is sampled on N_s points (each point is a line of sight integral measurement), the candidate set Q contains N_q points (usually distributed uniformly in the image area), and the image contains $N_p \propto 1/\varepsilon$ point sources, then all three values need to approach infinity as the reconstruction approaches the real emissivity function, and the computation time is proportional to $N_s \times N_q \times N_p$. For the example given in Fig.A3, $N_S \sim 10^4$, $N_q \sim 10^4$, $N_p \sim 10^4$, and it took ~100 hours to perform the reconstruction using a C++ program on a 2.93GHz Intel® Xeon® X5570 processor.

V. Results from simulated data and experiment data

The experiment has a limited set of measurements in the (t,θ) projection space. In a practical sense, it is helpful to test the reconstruction algorithms with the projection geometry used in the experiment. A Gaussian $f(x,y)=\exp\left(-\frac{(x+20)^2+y^2}{200}\right)$ was chosen as the test function (plotted in Fig A4 a), and was numerically "measured" with the same geometry as used in the experiment (see Fig A4 b).

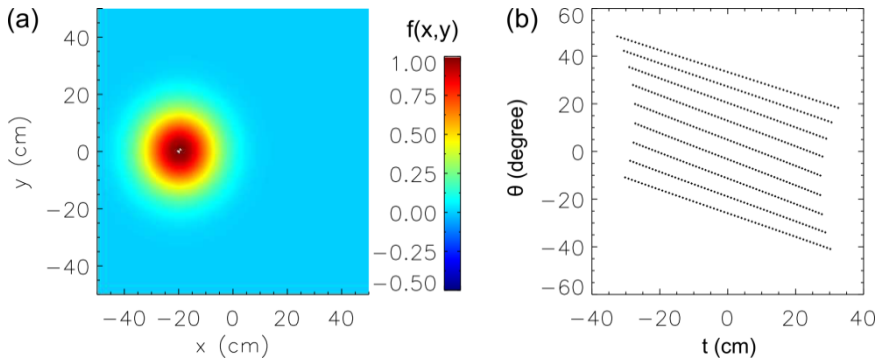

Fig A4: (a) An artificial test function f(x,y), which is a 2D Gaussian centered at (-20,0). (b) The distribution of 549 points in the projection space, where the simulated measurement is made for the test.

Five different published procedures [Hsieh 2009] [Camacho 1986] [Edwards 1986] [Nagayama 1987] [Janicki 1989] [Anton 1996] [Censor 1983] [Herman 2009] were tested with the simulated measurement for comparison with the proposed technique. In each case the reconstructed emissivity function f_{rec} has undesired artifacts, as shown in Fig A5. For example, some f_{rec} have

negative values. Another significant artifact is displacement of the peak position. Also in some f_{rec} artificial peaks are generated separate from the actual peak. These artifacts arise from the limitations of the measurement technique, and within the context of any one reconstruction it is impossible to separate them from the "real" emissivity. The DDR method has the least artifacts with this measurement geometry.

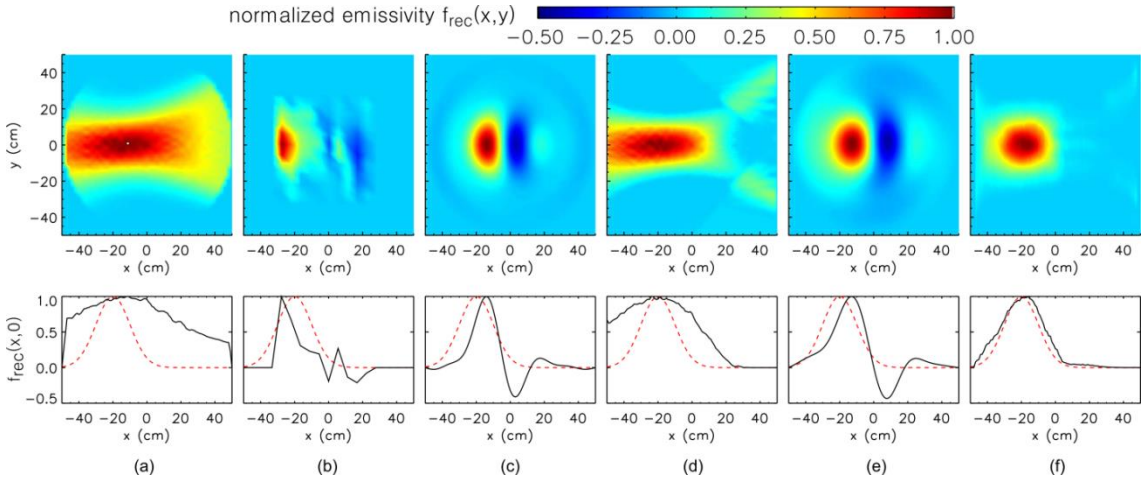

Fig A5: The emissivity f_{rec} reconstructed by 6 different procedures are shown on top: (a) back-projection; (b) least-squares fit with pixel basis; (c) least-squares fit with Fourier-Bessel basis; (d) ART with pixel basis; (e) ART with Fourier-Bessel basis; (f) DDR. Line cuts of f_{rec} at y=0 are shown on the bottom plot with solid lines, and line cut of the test emissivity is plotted with dashed lines.

Appendix B

Green function calculation of RMF antenna radiation pattern

A Green function solution of the RMF antenna radiation pattern is used in this work, to provide a model Alfvén wave field in a volume in which the orbit of single particles are calculated (Chapter 5). The solution generally follows a similar calculation presented by [Bamber 1995], who calculated the whistler wave pattern radiated by a loop antenna in a uniform cold plasma. We calculate the shear Alfvén wave field using the same method, with a finite temperature description of the plasma.

We start with the wave equation

$$\nabla \times (\nabla \times \vec{E}) - \frac{\omega^2}{c^2} \vec{E} = \frac{4\pi}{c^2} i\omega \vec{J} \tag{B.1}$$

, in which we have assumed monochromatic time variation $\sim \exp(-i\omega t)$ of all time dependent quantities. J is the total current in the system, in this case the sum of the current carried in the antenna J_A and the plasma current response to electric field fluctuations:

$$\vec{J} = \vec{\vec{\mu}} \cdot \vec{E} + \vec{J}_A, \tag{B.2}$$

where $\vec{\vec{\mu}}$ is the plasma mobility tensor. Using (B.1) and (B.2) the wave equation becomes

$$\nabla \times (\nabla \times \vec{E}) - k_0^2 \vec{\vec{\varepsilon}} \cdot \vec{E} = 4\pi \frac{ik_0^2}{\omega} \vec{J}_A, \tag{B.3}$$

where $k_0^2 \equiv \frac{\omega^2}{c^2}$, and $\vec{\vec{\varepsilon}} = \vec{\vec{I}} + \frac{4\pi i}{\omega}\vec{\vec{\mu}}$ is the plasma dielectric tensor.

The inhomogeneous wave equation (B.3) is solved by using a Green function method. If there exists a Green function $\vec{\vec{G}}(\vec{x}-\vec{x}')$, which is the response of a point source that satisfies:

$$\nabla\times(\nabla\times\vec{\vec{G}}) - k_0^2\vec{\vec{\varepsilon}}\cdot\vec{\vec{G}} = 4\pi\delta(\vec{x}-\vec{x}')\vec{\vec{I}}\,, \tag{B.4}$$

then a formal solution to (B.3) is obtained by convolving the Green function with the current distribution in the antenna

$$\vec{E}(\vec{x}) = \int dx'^3 \vec{\vec{G}}(\vec{x}-\vec{x}')\cdot\frac{ik_0^2}{\omega}\vec{J}_A(\vec{x}') \tag{B.5}$$

Equation (B.4) can be easily solved in Fourier space. Denote the Fourier transform of $\vec{\vec{G}}(\vec{x})$ as $\vec{\vec{G}}_k(\vec{k})$, then (B.4) in Fourier space is

$$-\vec{k}\times\vec{k}\times\vec{\vec{G}}_k(\vec{k}) - k_0^2\vec{\vec{\varepsilon}}\cdot\vec{\vec{G}}_k(\vec{k}) = 4\pi\vec{\vec{I}}\,, \tag{B.4f}$$

which directly yields

$$\vec{\vec{G}}_k(\vec{k}) = 4\pi(-\vec{k}\vec{k} + k^2\vec{\vec{I}} - k_0^2\vec{\vec{\varepsilon}})^{-1} \tag{B.6}$$

Therefore, we have found a solution of the wave equation.

Bamber took a different path, as he found it is easier to calculate $\vec{E}$ in k-space. In the Fourier k-space, equation (B.5) becomes

$$\vec{E}_k(\vec{k}) = \vec{\vec{G}}_k(\vec{k})\cdot\frac{ik_0^2}{\omega}\vec{J}_{Ak}(\vec{k})\,, \tag{B.5f}$$

where E_k and J_{Ak} are the Fourier transforms of E and J_A:

$$\vec{E}_k(\vec{k}) = \int dx^3\vec{E}(\vec{x})e^{i\vec{k}\cdot\vec{x}} \tag{B.7}$$

$$\vec{J}_{Ak}(\vec{k}) = \int dx^3\vec{J}_A(\vec{x})e^{i\vec{k}\cdot\vec{x}} \tag{B.8}$$

The wave generated by the RMF antenna is the superposition of the waves generated by each of the two coils. Because each coil has cylindrical symmetry, which greatly simplifies the calculation of (B.8), we calculate the wave pattern from the two coils separately and then superimpose them.

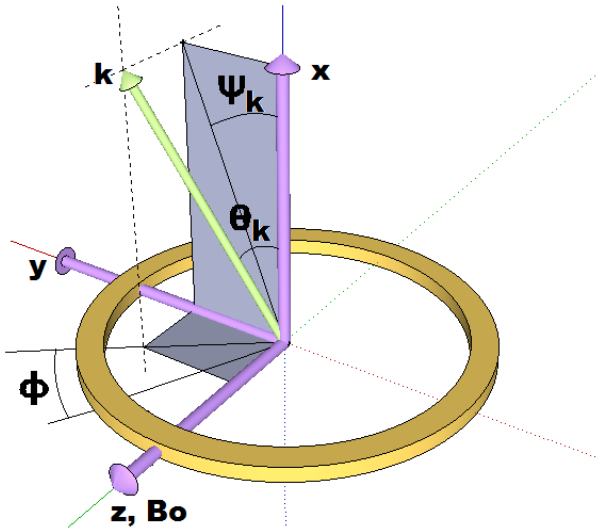

Fig B1: Coordinate system for one coil of the RMF antenna. The Cartesian coordinates that are used in the experiment and the test particle simulation are retained for clarity.

In the coordinate system shown in Fig B1, the antenna current is:

$$\vec{J}_A = I\delta(x)\delta(r - r_A)\hat{\phi}\,, \tag{B.9}$$

where r_A is the radius of the coil, and I is the total current amplitude. The antenna current k-spectra (eq B.8) is simplified as

$$\begin{aligned}\vec{J}_{Ak}(\vec{k}) &= \int dx^3 \vec{J}_A(\vec{x}) e^{i\vec{k}\cdot\vec{x}} \\ &= \int dx^3 I\delta(x)\delta(r-r_A)\hat{\phi}e^{i\vec{k}\cdot\vec{x}} \\ &= Ir_A\hat{\phi}\int_0^{2\pi} d\phi \cos(kr_A\sin\theta_k\cdot\cos\phi) + i\sin(kr_A\sin\theta_k\cdot\cos\phi) \\ &= Ir_A\hat{\phi}\int_0^{2\pi} d\phi \cos(kr_A\sin\theta_k\cdot\cos\phi) \end{aligned} \tag{B.10}$$

The plasma dielectric tensor with anisotropic electron temperature is provided by [Swanson 2011]:

$$\vec{\vec{\varepsilon}} = \begin{pmatrix} K_1 + \sin^2\psi_k K_0 & K_2 - \cos\psi_k \sin\psi_k K_0 & \cos\psi_k K_4 + \sin\psi_k K_5 \\ -K_2 - \cos\psi_k \sin\psi_k K_0 & K_1 + \cos^2\psi_k K_0 & \sin\psi_k K_4 - \cos\psi_k K_5 \\ \cos\psi_k K_4 - \sin\psi_k K_5 & \sin\psi_k K_4 + \cos\psi_k K_5 & K_3 \end{pmatrix} \tag{B.11}$$

where

$$K_0 = 2\sum_j \frac{\omega_{pj}^2 e^{-\lambda_j}}{\omega k_z v_{lj}} \sum_{n=-\infty}^{\infty} \lambda_j (I_n - I'_n)\left[Z(\varsigma_{nj}) + \frac{k_z v_{lj}}{\omega}\left(1 - \frac{T_{\perp j}}{T_{\parallel j}}\right)\frac{Z'(\varsigma_{nj})}{2}\right] \tag{B.12}$$

$$K_1 = 1 + \sum_j \frac{\omega_{pj}^2 e^{-\lambda_j}}{\omega k_z v_{lj}} \sum_{n=-\infty}^{\infty} \frac{n^2 I_n}{\lambda_j}\left[Z(\varsigma_{nj}) + \frac{k_z v_{lj}}{\omega}\left(1 - \frac{T_{\perp j}}{T_{\parallel j}}\right)\frac{Z'(\varsigma_{nj})}{2}\right] \tag{B.13}$$

$$K_2 = i\sum_j \frac{\varepsilon_j \omega_{pj}^2 e^{-\lambda_j}}{\omega k_z v_{lj}} \sum_{n=-\infty}^{\infty} n(I_n - I'_n)\left[Z(\varsigma_{nj}) + \frac{k_z v_{lj}}{\omega}\left(1 - \frac{T_{\perp j}}{T_{\parallel j}}\right)\frac{Z'(\varsigma_{nj})}{2}\right] \tag{B.14}$$

$$K_3 = 1 - \sum_j \frac{\omega_{pj}^2 e^{-\lambda_j}}{\omega k_z v_{lj}} \sum_{n=-\infty}^{\infty} I_n\left(\frac{\omega + n\omega_{cj}}{k_z v_{lj}}\right)\left[1 + \frac{n\omega_{cj}}{\omega}\left(1 - \frac{T_{\perp j}}{T_{\parallel j}}\right)\right] Z'(\varsigma_{nj}) \tag{B.15}$$

$$K_4 = \sum_j \frac{k_\perp \omega_{pj}^2 e^{-\lambda_j}}{k_z \omega \omega_{cj}} \sum_{n=-\infty}^{\infty} \frac{n I_n}{\lambda_j}\left[\frac{T_{\perp j}}{T_{\parallel j}} - \frac{n\omega_{cj}}{\omega}\left(1 - \frac{T_{\perp j}}{T_{\parallel j}}\right)\right]\frac{Z'(\varsigma_{nj})}{2} \tag{B.16}$$

$$K_5 = i\sum_j \frac{\varepsilon_j k_\perp \omega_{pj}^2 e^{-\lambda_j}}{k_z \omega \omega_{cj}} \sum_{n=-\infty}^{\infty} (I_n - I'_n)\left[\frac{T_{\perp j}}{T_{\parallel j}} - \frac{n\omega_{cj}}{\omega}\left(1 - \frac{T_{\perp j}}{T_{\parallel j}}\right)\right]\frac{Z'(\varsigma_{nj})}{2} \tag{B.17}$$

and

$\lambda_j \equiv \frac{1}{2}k_\perp^2 v_{tj}^2 / \omega_{cj}^2$, $\varsigma_{nj} \equiv \frac{\omega + n\omega_{cj}}{k_z v_{lj}}$; $I_n = I_n(\lambda)$ and $I'_n = I_n(\lambda)$ are the Bessel function of the first kind and its derivative; Z and Z' are the plasma dispersion function and its derivative. Subscript j refers to particle species, $\varepsilon = q/|q|$. $T_\parallel$ and $T_\perp$ are parallel and perpendicular temperature; v_l and v_t are the longitudinal and transverse thermal speed; k_z and $k_\parallel$ are the parallel and perpendicular wave number.

Appendix C

Evolution of the hot electron ring in absence of Alfvén waves

In this appendix we consider the decay of the hot electron ring in absence of Alfvén waves and ECRH, which has been observed in the experiment (Fig C1). The hot electrons can collide with ions or neutral atoms, causing transport in the parallel or cross-field direction which may lead to particle and energy loss. The ring also loses energy by radiation. Because these processes happen on much longer time scales compared to that of the electron de-trapping caused by an Alfvén wave, the mechanisms can be considered separately.

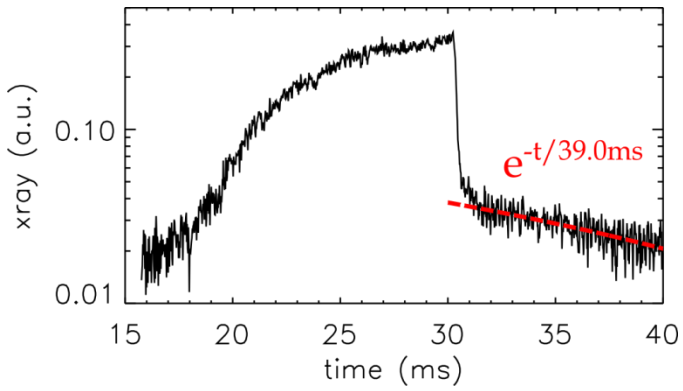

Fig C1: Time series of x-rays measured without the presence of Alfvén wave. The ECRH is on from t=0 to 30 ms. It talks about 0.5 ms for the microwaves to completely shut off, which caused the rapid drop of x-ray flux immediately after t=30 ms. After ECRH is completely turned off (t > 31 ms), the x-ray signal shows an exponential decay. This measurement is the same one in Fig 4.5 trace S, but is shown in log scale here.

Assume the plasma is fully ionized. The cumulative large angle electron-ion collision cross-section can be calculated by [Krall 1973]:

$$\sigma_M = 8\pi\left(\frac{Ze^2}{m_e v_0^2}\right)^2 \ln\Lambda \tag{C.1}$$

where $\ln\Lambda = \ln(r_{\max}/r_{\min})$ is the Coulomb logarithm, $r_{\max}$ and $r_{\min}$ are the maximum and minimum impact parameters. In this case, $r_{\max}$ is taken to be the Debye length $\lambda_D = (kT/4\pi ne^2)^{1/2}$, and $r_{\min}$ is the $90°$ deflection impact parameter $b_0 = \frac{Ze^2}{m_e v_0^2}$.

However the experiment is conducted late in the afterglow when the ionization rate is low. The hot electrons collide mostly with neutral atoms instead of ions. At high incident energies, the neutral atom cannot be treated as a solid particle with constant cross-section, and one must consider the charge distribution inside the atom. A quantum-mechanical approximation of electron-atom collision differential cross-section at small angle is given by [Jackson 1999]:

$$\frac{d\sigma}{d\Omega} = \left(\frac{2Ze^2}{pv}\right)^2 \frac{1}{(\theta^2 + \theta_{\min}^2)^2}, \tag{C.2}$$

where $\theta_{\min} = \hbar/pa$ is the minimum deflection angle, p is the incident momentum and a is the Bohr radius. Note that if we set $\theta_{\min} = 0$ then (C.2) becomes the classical Rutherford small-angle expression, from which (C.1) is derived. This means the electron screened atomic field deviates from the coulomb field of an ion mostly at large radius. We can proceed using eq (C.1) by only changing $r_{\max}$ to the impact parameter that corresponds to $\theta_{\min}$ [Landau 1958]:

$$r_{\max} = \frac{2Ze^2}{pv\theta_{\min}} = \frac{2Ze^2 a}{v\hbar}. \tag{C.3}$$

For a 200 keV electron, $\theta_{\min} = 9.4\times10^{-3}$ and $r_{\max} = 2.5\times10^{-10} cm$. The calculated collision frequency is $0.75\times10^{2} Hz$.

Due to these collisions, the hot electrons in the ring diffuse in both the radial and axial directions in a random-walk fashion. The evolution in the perpendicular direction can be approximated by the diffusion equation:

$$\frac{\partial}{\partial t} n = D_{\perp} \nabla_{\perp}^2 n, \tag{C.4}$$

where the single species cross-field diffusion coefficient is [Krall 1973]:

$$D_{\perp} = \frac{kT_{\perp} / m\nu}{\omega_{ce}^2 / \nu^2}. \tag{C.5}$$

The solution to Eq (C.4) has exponential decay time dependence. The decay time constant is set by spatial boundary conditions. In this experiment the radial boundary is set to the position of the edge of the waveguide r_0, where the particle density vanishes. The decay time is

$$\tau_{\perp} = \frac{r_0^2}{D_{\perp}\xi_{01}^2}, \tag{C.6}$$

where $\xi_{01} = 2.4$ is the first root of the zero order Bessel function. Setting experimental values $r_0 = 15cm$, $T_e = 200keV$, $\omega_{ce} = 2\pi\times1.23GHz$ and $\nu = 1\times10^{2} Hz$, the estimated perpendicular confinement time is 53.7 ms.

The collisional loss in the axial direction can be most directly described as a diffusion process in the electron pitch angle space [Roberts 1969]. Pitch-angle is the angle between electron velocity and the local magnetic field. Let α

be the electron's pitch angle at the mid plane. The diffusion equation which describes the evolution of the distribution function $f(\alpha,t)$ is [Kennel 1966]

$$\frac{\partial}{\partial t} f = \frac{1}{\sin\alpha}\frac{\partial}{\partial \alpha}\left(D_p \sin\alpha \frac{\partial f}{\partial \alpha}\right), \tag{C.7}$$

where the pitch-angle diffusion coefficient $D_p = \left\langle (\Delta\alpha)^2 \right\rangle / \Delta t$ is the average change in particle's pitch angle in unit time. Since (C.1) is calculated assuming $\left\langle (\Delta\theta_c)^2 \right\rangle = 1$ (θ_c is the deflection angle), the pitch-angle diffusion coefficient is simply $D_p = \frac{1}{2}\nu_c$, where ν_c is the collision frequency calculated above, and the factor $\frac{1}{2}$ comes from the perpendicular projection of the collision angle, i.e. $\left\langle (\Delta\alpha)^2 \right\rangle = \frac{1}{2}\left\langle (\Delta\theta_c)^2 \right\rangle$. The solution to (C.7) also follows exponential decay. An estimation of the decay time is given by [Kennel 1969] as $\tau_p(\alpha) = \alpha^2 / D_p$. Using this estimation, the time it takes for an electron, with energy of 200 keV and a pitch angle of $\frac{\pi}{2}$, to diffuse into the loss cone is about 49.3 ms.

The hot electron ring also loses energy by radiation. There are two main mechanisms: bremsstrahlung radiation and synchrotron radiation. The former is caused by electron acceleration during coulomb collisions; the latter is caused by the electron acceleration in the gyro motions. Both mechanisms can be described rather accurately by classical electrodynamics [Jackson 1999]. Here we are interested in the total radiation power (integrated over radiation frequency and angular distribution), to give an estimation of radiation caused energy decay time of the hot electrons.

Bremsstrahlung radiation is produced when the hot electrons experience collisions. If we ignore the screening effect of the electrons associated with the nucleus, the interaction can be approximated by a coulomb potential. When an electron collides with an ion of charge Ze at an impact parameter b, the total radiated energy during this collision is given by:

$$\Delta W = \frac{\pi Z^4 e^6}{3m^2 c^3 v_0} \frac{1}{b^3}. \tag{C.8}$$

Assume ions are uniformly distributed with a density n, we integrate over the impact parameter to obtain the radiation power:

$$P = \int_{b_{\min}}^{\infty} \frac{\pi Z^4 e^6}{3m^2 c^3 v_0} \frac{1}{b^3} 2\pi b v_0 n \cdot db = \frac{\pi^2 n Z^3 e^4 v_0^2}{3mc^3}, \tag{C.9}$$

where $b_{\min} = 2Ze^2 / mv_0^2$ is the closest distance of approach. For one 200 keV electron, the bremsstrahlung radiation power is about $2.1\times10^{-16} watt$ or $1.3\times10^{3} eV/s$, thus the energy decay time is on the order of 10^2 s. Assuming there are 10^{13} such electrons in the experiment, which is the upper-bound of total numbers of the hot electrons estimated by diamagnetic current measurement, then the total bremsstrahlung radiation power is on the order of $10^{-3} watt$. Electron screening could be included for a more accurate calculation, but as above does not significantly affect this number.

Synchrotron radiation, caused by the instantaneous acceleration of the hot electron gyro motion, can be estimated by the Larmor's formula with an electron in circular motion:

$$P = \frac{2}{3} \frac{e^2 c}{r_{ce}^2} \beta^4 \gamma^4, \tag{C.10}$$

where $\beta = v/c$ and $\gamma = \left(1-\beta^2\right)^{-1/2}$. For a 200 keV electron in a background magnetic field of 438 Gauss, the estimated radiation power is $6.5\times10^{-17}\,watt$ or $4.1\times10^{2}\,eV/s$. Thus the energy decay time is on the order of $5\times10^{2}\,s$, which is also much longer than the time scale of this experiment. The total power radiated does not exceed $10^{-3}\,watt$.

In conclusion, the radial and axial particle losses due to collisional diffusion are the main mechanisms for the decay of the hot electron ring, which happen at comparable rates in this experiment. If the losses by the two mechanisms drain the same source, then the decay time of the ring is mostly determined by the fastest process. Fig C2 is x-ray measurement with a collimated x-ray detector, showing x-rays generated by hot electrons scattered in the radial or axial (to loss cone) direction, both decay at roughly the same rate. The radiation energy loss is negligible in this experiment.

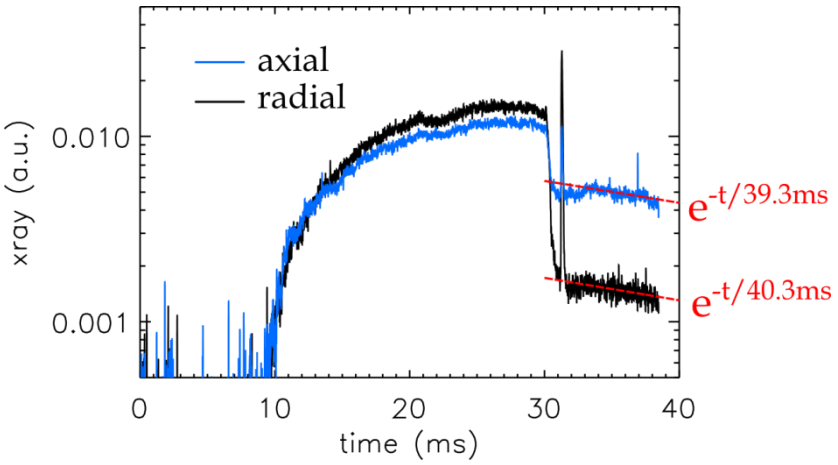

Fig C2. After ECRH is turned off, the x-ray signal shows an exponential decay in the axial and radial loss, both with a decay time about 40 ms. The ECRH is on from t=[0,30] ms. Around t=31 ms, the spike in the x-ray signal is caused by a shear Alfvén wave launched during the time t=[31.2,31.4] ms.

Appendix D

Boris Mover Scheme

This appendix briefly describes the Boris Mover scheme used in this work to integrate the discrete equations of motion for a charged particle in a given electromagnetic field.

The relativistic equations of motion for a particle of mass m and charge q in an electric and magnetic field E and B are

$$\frac{d(\gamma\vec{v})}{dt} = \frac{q}{m}\left(\vec{E} + \frac{\vec{v}}{c} \times \vec{B}\right), \tag{D.1}$$

$$\frac{d\vec{x}}{dt} = \vec{v}, \tag{D.2}$$

where $\gamma = 1/\sqrt{1 - v^2/c^2}$. In a finite difference form with a time step size of Δt, these equations are discretized as

$$\frac{\vec{u}(t+\frac{\Delta t}{2}) - \vec{u}(t-\frac{\Delta t}{2})}{\Delta t} = \frac{q}{m}\left(\vec{E} + \frac{\vec{u}(t+\frac{\Delta t}{2}) + \vec{u}(t-\frac{\Delta t}{2})}{2c} \times \frac{\vec{B}}{\gamma}\right), \tag{D.3}$$

$$\frac{\vec{x}(t+\Delta t) - \vec{x}(t)}{\Delta t} = \frac{\vec{u}(t+\frac{\Delta t}{2})}{\gamma}. \tag{D.4}$$

Here we have used $\vec{u} = \gamma\vec{v}$ to replace $\vec{v}$ in (D.1) so that the relativity merely counts for a renormalization of the magnetic field in (D.3). The solution to the implicit equation (D.3) is given by [Boris 1970]:

$$\vec{u}_1 = \vec{u}(t - \frac{\Delta t}{2}) + \frac{q\Delta t}{2m}\vec{E}\,, \tag{D.5}$$

$$\vec{u}_2 = \vec{u}_1 + f_1\vec{u}_1 \times \vec{B}/\gamma\,, \tag{D.6}$$

$$\vec{u}_3 = \vec{u}_1 + f_2\vec{u}_2 \times \vec{B}/\gamma\,, \tag{D.7}$$

$$\vec{u}(t + \frac{\Delta t}{2}) = \vec{u}_3 + \frac{q\Delta t}{2m}\vec{E}\,, \tag{D.8}$$

where $f_1 = \dfrac{\tan\dfrac{q\Delta t}{2mc\gamma}B}{B/\gamma}$ and $f_2 = 2f_1/(1+f_1^2B^2/\gamma^2)$. After some algebra [Decyk 2007], equation (D.6) and (D.7) can be simplified (in the sense of reduced number of numerical operations) to:

$$\vec{u}_3 = \left\{\vec{u}_1\left[1-\left(\frac{\Omega\Delta t}{2}\right)^2\right] + \vec{u}_1 \times \vec{\Omega}\Delta t + \frac{(\Delta t)^2}{2}\left[\vec{u}_1 \cdot \vec{\Omega}\right]\vec{\Omega}\right\} / \left[1+\left(\frac{\Omega\Delta t}{2}\right)^2\right], \tag{D.9}$$

with $\vec{\Omega} = \dfrac{q\vec{B}}{\gamma mc}$. The position of the particle $\vec{x}$ can be updated in a straightforward manner using (D.4).

BIBLIOGRAPHY

Alfvén, H. (1942), Existence of electromagnetic-hydrodynamic waves, Nature, 150(3805), 405–406.

BAPSF website, http://plasma.physics.ucla.edu/

Anton, M., H. Weisen, M. J. Dutch, W. von der Linden, F. Buhlmann, R. Chavan, B. Marletaz, P. Marmillod, and P. Paris (1996), X-ray tomography on the TCV tokamak, Plasma Physics and Controlled Fusion, 38(11), 1849–1878

Bamber, J. F. (1995), Whistler wave interaction with density striations, University of California, Los Angeles.

Beall, D. S., C. O. Bostrom, and D. J. Williams (1967), Structure and decay of the STARFISH radiation belt, October 1963 to December 1965, Journal of Geophysical Research, 72(13), 3403–3424.

Boris, J. P. (1970), Relativistic plasma simulation-optimization of a hybrid code, in Proc. Fourth Conf. Num. Sim. Plasmas, Naval Res. Lab, Wash. DC, pp. 3–67.

Bortnik, J., R. M. Thorne, T. P. O'Brien, J. C. Green, R. J. Strangeway, Y. Y. Shprits, and D. N. Baker (2006), Observation of two distinct, rapid loss mechanisms during the 20 November 2003 radiation belt dropout event, J. Geophys. Res., 111(A12), A12216

Brautigam, D. H., and J. M. Albert (2000), Radial diffusion analysis of outer radiation belt electrons during the October 9, 1990, magnetic storm, Journal of Geophysical Research: Space Physics (1978–2012), 105(A1), 291–309.

Brito, T., L. Woodger, M. Hudson, and R. Millan (2012), Energetic radiation belt electron precipitation showing ULF modulation, Geophys. Res. Lett., 39(22), L22104

Camacho, J. F., and R. S. Granetz (1986), Soft x-ray tomography diagnostic for the Alcator C tokamak, Review of Scientific Instruments, 57(3), 417 –425

Censor, Y. (1983), Finite series-expansion reconstruction methods, Proceedings of the IEEE, 71(3), 409 – 419

Cooper, C. (2012), Transport in a field aligned magnetized plasma/neutral gas boundary: the end of the plasma, University of California, Los Angeles.

Decyk, V. K. (2007), UPIC: A framework for massively parallel particle-in-cell codes, Computer Physics Communications, 177(1), 95–97.

Degeling, A. W., R. Rankin, K. Murphy, and J. Rae (2013), Magnetospheric Convection and Magnetopause Shadowing Effects in ULF wave Driven Energetic Electron Transport, J. Geophys. Res.

Dupont, D. G. (2004), Nuclear Explosions in Orbit, Scientific American, 290(6), 100–107

Edwards, A. W. et al. (1986), Rapid Collapse of a Plasma Sawtooth Oscillation in the JET Tokamak, Phys. Rev. Lett., 57(2), 210–213

Everson, E. T., P. Pribyl, C. G. Constantin, A. Zylstra, D. Schaeffer, N. L. Kugland, and C. Niemann (2009), Design, construction, and calibration of a three-axis, high-frequency magnetic probe (B-dot probe) as a diagnostic for exploding plasmas, Review of Scientific Instruments, 80, 113505.

Gekelman, W., H. Pfister, Z. Lucky, J. Bamber, D. Leneman, and J. Maggs (1991), Design, construction, and properties of the large plasma research device-The LAPD at UCLA, Review of scientific instruments, 62(12), 2875–2883.

Gekelman, W., D. Leneman, J. Maggs, and S. Vincena (1994), Experimental observation of Alfvén wave cones, Physics of Plasmas, 1, 3775.

Gekelman, W., S. Vincena, D. Leneman, and J. Maggs (1997), Laboratory experiments on shear Alfvén waves and their relationship to space plasmas, Journal of geophysical research, 102, 7225–7236.

Gigliotti, A., W. Gekelman, P. Pribyl, S. Vincena, A. Karavaev, X. Shao, A. S. Sharma, and D. Papadopoulos (2009), Generation of polarized shear Alfvén waves by a rotating magnetic field source, Physics of Plasmas, 16(9), 092106

Herman, G. T. (2009), Fundamentals of computerized tomography: image reconstruction from projections, Springer.

Horne, R. B., S. A. Glauert, and R. M. Thorne (2003), Resonant diffusion of radiation belt electrons by whistler-mode chorus, Geophys. Res. Lett., 30(9), 1493

Hsieh, J. (2009), Computed Tomography: Principles, Design, Artifacts, and Recent Advances, SPIE.

Hutchinson, I. H. (2005), Principles of Plasma Diagnostics, Cambridge University Press.

Ikegami, H., H. Ikezi, M. Hosokawa, S. Tanaka, and K. Takayama (1967), Shell structure of a hot-electron plasma, Physical Review Letters, 19(14), 778–781.

Inan, U. S., T. F. Bell, J. Bortnik, and J. M. Albert (2003), Controlled precipitation of radiation belt electrons, J. Geophys. Res., 108(A5), 1186

Jackson, J. D. (1999), Classical electrodynamics, Wiley, New York.

Janicki, C., R. Décoste, and C. Simm (1989), High resolution soft-x-ray tomography of sawtooth oscillations on the Tokamak de Varennes, Phys. Rev. Lett., 62(26), 3038–3041

Karavaev, A. V., N. A. Gumerov, K. Papadopoulos, X. Shao, A. S. Sharma, W. Gekelman, A. Gigliotti, P. Pribyl, and S. Vincena (2010), Generation of whistler waves by a rotating magnetic field source, Physics of Plasmas, 17, 012102.

Karavaev, A. V., N. A. Gumerov, K. Papadopoulos, X. Shao, A. S. Sharma, W. Gekelman, Y. Wang, B. Van Compernolle, P. Pribyl, and S. Vincena (2011), Generation of shear Alfvén waves by a rotating magnetic field source: Three-dimensional simulations, Phys. Plasmas, 18(3), 032113–032113–13

Kennel, C. F. (1969), Consequences of a magnetospheric plasma, Reviews of Geophysics, 7(1, 2), 379–419.

Kennel, C. F., and H. E. Petschek (1966), Limit on stably trapped particle fluxes, Journal of Geophysical Research, 71(1), 1–28.

Kivelson, M. G., and C. T. Russell (1995), Introduction to space physics, Cambridge university press.

Krall, N. A., and A. W. Trivelpiece (1973), Principles of plasma physics, McGraw-Hill.

Landau, L. D. (1958), The kinetic equation in the case of coulomb interaction, DTIC Document.

Lawrance, E. (2010), Colliding Magnetic Flux Ropes and Quasi-Separatrix Layers in a Laboratory Plasma, University of California, Los Angeles.

Loto'aniu, T. M., H. J. Singer, C. L. Waters, V. Angelopoulos, I. R. Mann, S. R. Elkington, and J. W. Bonnell (2010), Relativistic electron loss due to ultralow frequency waves and enhanced outward radial diffusion, J. Geophys. Res., 115(A12), A12245

Maggs, J. E., and G. J. Morales (2003), Laboratory realization of an Alfvén wave maser, Physical review letters, 91(3), 035004–035004.

Millan, R. M., and R. M. Thorne (2007), Review of radiation belt relativistic electron losses, J. Atmos. Sol.-Terr. Phys., 69(3), 362–377.

Morales, G. J., and J. E. Maggs (1997), Structure of kinetic Alfven waves with small transverse scale length, Physics of Plasmas, 4, 4118.

Morales, G. J., R. S. Loritsch, and J. E. Maggs (1994), Structure of Alfvén waves at the skin - depth scale, Phys. Plasmas, 1(12), 3765 – 3774

Nagayama, Y. (1987), Tomography of m=1 mode structure in tokamak plasma using least #x2010;square #x2010;fitting method and Fourier #x2013;Bessel expansions, Journal of Applied Physics, 62(7), 2702 –2706

Nishimura, Y., A. Shinbori, T. Ono, M. Iizima, and A. Kumamoto (2007), Evolution of ring current and radiation belt particles under the influence of storm-time electric fields, Journal of Geophysical Research: Space Physics (1978–2012), 112(A6).

O'Brien, T. P., K. R. Lorentzen, I. R. Mann, N. P. Meredith, J. B. Blake, J. F. Fennell, M. D. Looper, D. K. Milling, and R. R. Anderson (2003), Energization of relativistic electrons in the presence of ULF power and MeV microbursts: Evidence for dual ULF and VLF acceleration, J. Geophys. Res., 108(A8), 1329

Ohtani, S., Y. Miyoshi, H. J. Singer, and J. M. Weygand (2009), On the loss of relativistic electrons at geosynchronous altitude: Its dependence on magnetic configurations and external conditions, J. Geophys. Res., 114(A1), A01202

Oskooi, A. F., D. Roundy, M. Ibanescu, P. Bermel, J. D. Joannopoulos, and S. G. Johnson (2010), Meep: A flexible free-software package for electromagnetic simulations by the FDTD method, Computer Physics Communications, 181(3), 687–702

Roberts, C. S. (1969), Pitch-angle diffusion of electrons in the magnetosphere, Reviews of Geophysics, 7(1-2), 305–337.

Sato, N., K. Hayashi, S. Kokubun, T. Oguti, and H. Fukunishi (1974), Relationships between quasi-periodic VLF emission and geomagnetic pulsation, Journal of Atmospheric and Terrestrial Physics, 36(9), 1515–1526

Sauvaud, J.-A., R. Maggiolo, C. Jacquey, M. Parrot, J.-J. Berthelier, R. J. Gamble, and C. J. Rodger (2008), Radiation belt electron precipitation due to VLF transmitters: Satellite observations, Geophys. Res. Lett., 35(9), L09101

Shprits, Y. Y., R. M. Thorne, R. Friedel, G. D. Reeves, J. Fennell, D. N. Baker, and S. G. Kanekal (2006), Outward radial diffusion driven by losses at magnetopause, J. Geophys. Res., 111(A11), A11214

SIA (2012), 2012 SIA State of the Satellite Industry Report,

Southwood, D. J., and M. G. Kivelson (1981), Charged particle behavior in low-frequency geomagnetic pulsations 1. Transverse waves, Journal of Geophysical Research: Space Physics (1978–2012), 86(A7), 5643–5655.

Swanson, D. G. (2011), Plasma Kinetic Theory, Chapman and Hall/CRC

Thorne, R. M., and C. F. Kennel (1971), Relativistic electron precipitation during magnetic storm main phase, J. Geophys. Res., 76(19), 4446–4453

Turner, D. L., Y. Shprits, M. Hartinger, and V. Angelopoulos (2012), Explaining sudden losses of outer radiation belt electrons during geomagnetic storms, Nat Phys, 8(3), 208–212

Ukhorskiy, A. Y., B. J. Anderson, K. Takahashi, and N. A. Tsyganenko (2006), Impact of ULF oscillations in solar wind dynamic pressure on the outer radiation belt electrons, Geophysical research letters, 33(6).

Vincena, S., W. Gekelman, and J. Maggs (2001), Shear Alfvén waves in a magnetic beach and the roles of electron and ion damping, Phys. Plasmas, 8(9), 3884–3896

West, H. I., R. M. Buck, and J. R. Walton (1972), Shadowing of Electron Azimuthal-Drift Motions near the Noon Magnetopause, Nature, 240(97), 6–7

Zong, Q.-G., X.-Z. Zhou, Y. F. Wang, X. Li, P. Song, D. N. Baker, T. A. Fritz, P. W. Daly, M. Dunlop, and A. Pedersen (2009), Energetic electron response to ULF waves induced by interplanetary shocks in the outer radiation belt, Journal of Geophysical Research: Space Physics (1978–2012), 114(A10).